ABSTRACT

FLUID DYNAMICS OF INTERACTING PARTICLES: BOUNCING DROPLETS AND COLLOID-POLYMER MIXTURES

by
Lauren Barnes

Interacting particles are a common theme across various physical systems, particularly on the atomic and sub-atomic scales. While these particles cannot be seen with the human eye, insight into such systems can be gained by observing macroscopic systems whose physical behavior is similar. This dissertation consists of three different chapters, each presenting a different problem related to interacting particles, as follows:

Chapter 1 explores chaotic trajectories of a droplet bouncing on the surface of a vertically vibrating fluid bath, with a simple harmonic force acting on the droplet. The bouncing droplet system has attracted recent interest because it exhibits behaviors similar to those previously observed only in the microscopic quantum realm. In this investigation, an approximation is presented for an existing model that describes a walking droplet's trajectories in the xy-plane. Simulations of the approximate model show that it captures behaviors of the full model, but is less computationally expensive to simulate.

Chapter 2 presents the results of a theoretical investigation of one-dimensional chains of bouncing droplets, with particular attention to the case in which the drop at one end of the chain is oscillated periodically. Numerical simulation results are also presented, and are found to compare favorably with predictions based on linear theory. Both demonstrate the existence of resonant forcing frequencies, as well as the presence of an oscillatory instability in the chain as the forcing acceleration is increased. For sufficiently high forcing frequencies, dynamic stabilization of the chain into a new bouncing state is observed. The results of this investigation highlight the

role of temporally nonlocal interactions in the dynamics of this unique system, and have been published in the journal *Comptes Rendus Mécanique*.

Chapter 3 investigates the phase behavior of colloid-polymer suspensions in a microgravity environment. Phase transitions in such suspensions give valuable insight into atomic-scale phase transitions. While colloidal suspensions exhibit fluid-solid coexistence, the addition of polymer leads to three-phase coexistence. A numerical exploration of the effects of fluid viscosity and other system parameters on the phase behavior of colloid-polymer suspensions is presented. The first few sections of Chapter 3 describe the process of downloading and processing experimental images from a NASA database and extracting information from them in order to quantitatively characterize the separation of the mixture into distinct phases as time progresses. The remainder of this chapter is dedicated to the development and implementation of a phase-field model that couples a Cahn-Hilliard equation for the colloid concentration with the incompressible Stokes equations to include the effects of hydrodynamic interactions between the particles and the surrounding fluid in the low-Reynolds number limit. The model also incorporates the dependence of viscosity on the local colloid concentration, which significantly influences the hydrodynamic behavior. Simulation results for varied system parameters are presented and discussed.

FLUID DYNAMICS OF INTERACTING PARTICLES: BOUNCING DROPLETS AND COLLOID-POLYMER MIXTURES

by
Lauren Barnes

A Dissertation
Submitted to the Faculty of
New Jersey Institute of Technology and
Rutgers, The State University of New Jersey – Newark
in Partial Fulfillment of the Requirements for the Degree of
Doctor of Philosophy in Mathematical Sciences

Department of Mathematical Sciences
Department of Mathematics and Computer Science, Rutgers-Newark

August 2023

APPROVAL PAGE

FLUID DYNAMICS OF INTERACTING PARTICLES: BOUNCING DROPLETS AND COLLOID-POLYMER MIXTURES

Lauren Barnes

Dr. Anand U. Oza, Dissertation Advisor — Date
Assistant Professor of Mathematical Sciences, NJIT

Dr. Lou Kondic, Committee Member — Date
Distinguished Professor of Mathematical Sciences, NJIT

Dr. Linda J. Cummings, Committee Member — Date
Professor of Mathematical Sciences, NJIT

Dr. Boris Khusid, Committee Member — Date
Professor of Chemical and Materials Engineering, NJIT

Dr. Daniel M. Harris, Committee Member — Date
Assistant Professor of Engineering, Brown University

BIOGRAPHICAL SKETCH

Author: Lauren Barnes

Degree: Doctor of Philosophy

Date: August 2023

Undergraduate and Graduate Education:

- Doctor of Philosophy in Mathematical Sciences,
  New Jersey Institute of Technology, Newark, NJ, 2023
- Bachelor of Science in Mathematics,
  William Paterson University, Wayne, NJ, 2016

Major: Applied Mathematics

Presentations and Publications:

L. Barnes, G. Pucci and A.U. Oza, "Resonant interactions in bouncing droplet chains," *Comptes Rendus Mecanique*, vol. 348, pp 573-589, 2020.

L. Barnes, "The role of concentration-dependent viscosity on the dynamics of colloid-polymer mixtures," *Oral Presentation*, American Society for Gravitational and Space Research annual meeting, Houston, TX, 2022.

L. Barnes, "Modeling phase separation of colloid-polymer mixtures in microgravity," *Oral Presentation*, Northeast Complex Fluids and Soft Matter Workshop, Stevens University, NJ, 2022.

L. Barnes, "Modeling of colloid-polymer mixtures in microgravity," *Oral Presentation (virtual)*, American Physical Society Division of Fluid Dynamics annual meeting, 2021.

L. Barnes, "Continuum modeling of colloid-polymer mixtures in microgravity," *Poster Presentation*, American Society for Gravitational and Space Research annual meeting, Baltimore, MD, 2021.

L. Barnes, "Modeling of colloid-polymer mixtures in microgravity," *Oral Presentation (virtual)*, NJIT Dana Knox Student Research Showcase, 2021.

L. Barnes, "Resonance, instability and dynamical stabilization in bouncing droplet chains," *Oral Presentation (virtual)*, American Physical Society Division of Fluid Dynamics annual meeting, 2020.

L. Barnes, "Modeling of colloid-polymer mixtures in microgravity," *Oral Presentation (virtual)*, American Society for Gravitational and Space Research annual meeting, 2020.

Worthy are You, our Lord and God, to receive glory and honor and power, for You created all things, and by Your will they existed and were created.

Revelation 4:11

ACKNOWLEDGMENTS

I would like to thank my advisor, Anand Oza, for going above and beyond the expectations and duties of an advisor. Your support and encouragement over these years mean more to me than you know, and your extensive knowledge and intuition as a researcher make me realize that I am very privileged to be working with you.

I would also like to thank Lou Kondic, Linda Cummings, Boris Khusid, and Daniel Harris for being very knowledgeable and supportive dissertation committee members and for their valuable input and mentorship along the way.

I would like to gratefully acknowledge the financial support I received from the Department of Mathematical Sciences at NJIT as a teaching and research assistant. I also gratefully acknowledge the financial support our team received from NASA.

Many thanks to Ryan Allaire, an excellent mentor and friend, for helping me to survive my first year. I want to thank all of my fellow NJIT students, including Rituparna Basak, Ruqi Pei, Axel Turnquist, Brandon Behring, Linda Firriolo, Yasser Almoteri, Erli Wind-Anderson, Tadanaga Takahashi, David Mazowiecki, Soheil Saghafi, Connor Robertson, Esther Wang, Elizabeth Daudelin, Diego Rios, Valeria Barra, Yiming Yu, and many others for their camaraderie throughout these years. I also want to thank Eliana Antoniou, Melkamu Zeleke, Jyoti Champanerkar, Paul Von Dohlen, Christina Mouser, David Nacin, and Zhiqiang Chen, all of whom taught me to love math and inspired me to pursue a Ph.D.

Finally, I would like to say a special thank-you to my mother and father, Dorothy and Timothy Barnes, for homeschooling me from kindergarten through high school and teaching me all the most important things in life. I also specially thank my sister and best friend, Rebecca Barnes, whose positive outlook and sense of humor have kept me lighthearted during these years of hard work, and my best friend, Rachel Taylor, for always being there to give a listening ear and an encouraging word. Many thanks

go to all of my family members and friends, including Julie Mee, Jennette Firriolo, Andrew Firriolo, Carina Castagna, Hannah Rodums, Jason Krantz, Lisa Gessler, Mark and Wilma Cordes, and many others who have been there for me through thick and thin.

TABLE OF CONTENTS

Chapter **Page**

1 INTRODUCTION 1

1.1 The Pilot-Wave Dynamics of Walking Droplets 1

1.2 Phase-Transitions in Colloid-Polymer Mixtures 2

2 CHAOTIC TRAJECTORIES OF A WALKING DROPLET 7

2.1 Introduction and Background 7

2.2 The Stroboscopic Model 8

2.3 A Finite Mode Approximation 13

2.3.1 Circular orbit solutions 16

2.4 Time-Dependent Simulations 17

2.5 Comparison of Results 20

2.6 Discussion and Future Work 23

3 RESONANT INTERACTIONS IN DROPLET CHAINS 26

3.1 Introduction and Background 26

3.2 Equilibrium Solutions and Linear Stability 29

3.3 Forced Droplet Chains 34

3.3.1 Linear theory 35

3.3.2 Nonlinear oscillations of forced droplet chains 38

3.3.3 High-frequency limit $f \to \infty$ 44

3.4 Discussion and Future Work 47

4 PHASE SEPARATION IN COLLOID-POLYMER MIXTURES 51

4.1 Introduction and Background 51

4.1.1 Experimental details and overview 53

4.2 Image Processing and Analysis 57

4.2.1 Image processing 58

4.2.2 Image analysis: quantifying phase domain growth 65

TABLE OF CONTENTS
(Continued)

Chapter **Page**

4.3 Model for Phase Separation in Colloid-Polymer Mixtures 76

4.3.1 Cahn-Hilliard equation 76

4.3.2 Coupled system: Cahn-Hilliard equation with hydrodynamic interactions 85

4.3.3 Numerical implementation 89

4.4 Simulation Results 96

4.4.1 Qualitative behavior in simulation outputs 96

4.4.2 Quantifying phase domain growth in simulation outputs 100

4.4.3 Validations and checks 111

4.4.4 Preliminary results for BCAT-3 and BCAT-4 112

4.5 Discussion and Future Work 117

APPENDIX A INCOMPRESSIBLE STOKES EQUATIONS: STREAM FUNCTION FORMULATION 120

REFERENCES 124

LIST OF TABLES

Table **Page**

4.1 System Parameters for BCAT-3 Samples 55

4.2 System Parameters for BCAT-4 Samples 55

4.3 System Parameters for BCAT-5 Samples 56

4.4 Parameters for Rolling-Ball Radius in Image Processing Algorithm . . . 64

LIST OF FIGURES

Figure		Page
1.1	Overview of the walking droplet problem.	3
1.2	Overview of the colloid-polymer problem.	4
1.3	Colloid-polymer suspension phase diagram.	5
2.1	A walking droplet in a central spring force.	9
2.2	Strobe image of a walker.	10
2.3	Orbital radius vs. spring constant: constant radius.	18
2.4	Orbital angular frequency vs. spring constant: constant radius.	19
2.5	Stable, circular orbit: $\gamma = 0.94$.	20
2.6	Unstable orbits and a chaotic trajectory.	21
2.7	Orbital frequencies from full-model simulations.	24
2.8	Orbital frequencies from reduced-model simulations.	25
3.1	Free and confined rings of bouncing droplets.	27
3.2	A chain of bouncing droplets.	28
3.3	Equilibrium solutions at intersection points of zero-contours.	31
3.4	Symmetric bouncing states.	34
3.5	Stability analysis of droplet chains.	35
3.6	Linear theory prediction of oscillation amplitudes for n_{11}-bouncing state.	36
3.7	Linear theory prediction of oscillation amplitudes for other bouncing states.	37
3.8	Numerically-simulated trajectories of a forced droplet chain.	39
3.9	Oscillation amplitude vs. forcing frequency: $A_1 = \lambda_F/8$ (numerical)	40
3.10	Oscillation amplitudes for numerical simulations with $A_1 = \lambda_F/4$.	42
3.11	Oscillation amplitudes for numerical simulations of other bouncing states.	43
3.12	Complex aperiodic oscillations.	44
3.13	High forcing frequency simulation results for n_{11}-bouncing state.	45
3.14	High forcing frequency simulation results for n_{11}-bouncing state.	47

LIST OF FIGURES
(Continued)

Figure **Page**

4.1 Phase separation images from microgravity experiment. 54

4.2 Raw images of BCAT sample. 58

4.3 Image enhancement procedure. 61

4.4 Enhanced images of BCAT-3 Sample 1. 65

4.5 Enhanced images of BCAT-3 Sample 2. 65

4.6 Enhanced images of BCAT-3 Sample 4. 66

4.7 Enhanced images of BCAT-3 Sample 6. 66

4.8 Enhanced images of BCAT-4 Sample 2. 67

4.9 Enhanced images of BCAT-4 Sample 3. 68

4.10 Enhanced images of BCAT-5 Sample 4. 69

4.11 Enhanced images of BCAT-5 Sample 5. 69

4.12 Enhanced images of BCAT-5 Sample 6. 70

4.13 Enhanced images of BCAT-5 Sample 7. 70

4.14 Enhanced images of BCAT-5 Sample 8. 71

4.15 Autocorrelation matrix and 1D autocorrelation function. 71

4.16 Phase domain growth curves for experimental images: BCAT-3. 72

4.17 Phase domain growth curves for experimental images: BCAT-4. 73

4.18 Phase domain growth curves for experimental images: BCAT-5. 74

4.19 Validation of autocorrelation results for BCAT-5. 75

4.20 Mobility function $\Gamma(\phi)$. 78

4.21 Helmholtz free energy and colloid chemical potential plots. 80

4.22 Depletion interactions. 81

4.23 Free volume fraction $\alpha(\phi)$. 82

4.24 Linear stability analysis: spinodal decomposition. 84

4.25 Suspension viscosity function $\eta(\phi)$. 86

4.26 Time convergence plot for time-stepping scheme. 91

LIST OF FIGURES
(Continued)

Figure **Page**

4.27 Simulation with hydrodynamic interactions: BCAT-5 Sample 7. 98

4.28 Simulation without hydrodynamic interactions: BCAT-5 Sample 7. . . . 99

4.29 Simulation with hydrodynamic interactions: BCAT-5 Sample 4. 101

4.30 Simulation without hydrodynamic interactions: BCAT-5 Sample 4. . . . 102

4.31 Vortex quadrupole. 103

4.32 Parameter fitting for phase domain growth curves. 104

4.33 Phase domain growth curves for simulation: BCAT-5 Sample 4. 105

4.34 Phase domain growth curves for simulation: BCAT-5 Sample 5. 105

4.35 Phase domain growth curves for simulation: BCAT-5 Sample 6. 106

4.36 Phase domain growth curves for simulation: BCAT-5 Sample 7. 106

4.37 Phase domain growth curves for simulation: BCAT-5 Sample 8. 107

4.38 Phase domain growth curves for experimental images and simulations with $\gamma = 0$ of all BCAT-5 samples. 109

4.39 Phase domain growth curves for experimental images and simulations with $\gamma = 50$ of all BCAT-5 samples. 110

4.40 Comparison of $\gamma = 0$ and $\gamma = 50$ simulation curves in dimensionless variables. 111

4.41 Validation of spatial resolution and domain size. 112

4.42 Preliminary $\gamma = 0$ simulation results for BCAT-3 samples. 113

4.43 Preliminary $\gamma = 50$ simulation results for BCAT-3 samples. 114

4.44 Preliminary $\gamma = 0$ simulation results for BCAT-4 samples. 115

4.45 Preliminary $\gamma = 50$ simulation results for BCAT-4 samples. 116

CHAPTER 1

INTRODUCTION

Quantum phenomena and other mysterious behaviors that take place on an atomic or sub-atomic scale remain a puzzlement largely because their mechanisms cannot be observed by the human eye, even with the most powerful of microscopes. However, some of the tiny but intricate systems that exhibit these behaviors have macroscopic analogues that behave in a strikingly similar manner. By observing these larger-scale analogous systems, we can visualize and observe phenomena that can be probed in experiments, which are often more easily implemented on a macroscopic scale. In this dissertation, we study two such macroscopic analogues that imitate microscopic systems: bouncing droplets and colloid-polymer suspensions, both of which involve interacting particles in a hydrodynamic setting. The bouncing droplet problem is briefly introduced in Section 1.1 of this chapter, and our work on this problem is detailed in Chapters 2 and 3. A brief introduction to the colloid-polymer suspension system is given in Section 1.2, with our work presented in Chapter 4.

1.1 The Pilot-Wave Dynamics of Walking Droplets

Experiments by Yves Couder, Emmanuel Fort, and coworkers have shown that a millimetric droplet is able to bounce in place [118, 30] (Figure 1.1(a)) or even walk [31, 93] (Figure 1.1(b)) on the surface of a vertically vibrated fluid bath without coalescing with the fluid, if the forcing acceleration of the bath is sufficiently large. When such a droplet bounces, it produces standing (Faraday) waves (Figure 1.1(c)) on the bath's surface, which can in turn influence the droplet's trajectory [49, 40]. This system offers an intriguing visualization of wave-particle coupling on a macroscopic scale [93], and has demonstrated phenomena that have otherwise been observed only in the microscopic quantum realm. Some examples of these phenomena

include tunneling [38], quantized Larmor levels [49, 55], double quantization in a harmonic potential [88, 87, 86], Zeeman-like splitting [39], multimodal statistics in circular corrals [57, 32], statistical projection effects in elliptical corrals [105], Friedel oscillations [106], and the Hong-Ou-Mandel effect [116]. Analogues of single- and double-slit diffraction [28] remain the subject of ongoing investigation [8, 16, 34, 95, 100]. The relation between this hydrodynamic system and quantum pilot-wave theories has been reviewed elsewhere [29, 22, 21].

A key feature of the walker system is its *path memory*, as the walker's trajectory is influenced by the waves it generates during its prior impacts [49, 40]. These waves are sustained by the vibrational forcing of the bath. While single droplets are influenced by their own history, collections of bouncers and walkers may interact through the collective wave field they generate. Lattices of bouncers have been shown to arrange themselves into eight of the eleven possible Archimedean tilings of the plane [37], and both stationary and spontaneously spinning droplet lattices have been reported [94, 76, 41] (Figure 1.2).

The first part of this dissertation is concerned with theoretical models of the pilot-wave dynamics of walking droplets. In Chapter 2, we derive, analyze and simulate a reduced model for the dynamics of a single droplet under the influence of a central harmonic potential. Such a system has been realized in experiments, and constitutes a hydrodynamic analog of the canonical simple harmonic oscillator problem in quantum mechanics. In Chapter 3, we consider the dynamics of a linear chain of bouncing droplets, a hydrodynamic analog of a one-dimensional crystal.

1.2 Phase-Transitions in Colloid-Polymer Mixtures

Colloids have been studied extensively because of the many similarities they share with behaviors of atoms in a microscopic setting. Examples of microscopic situations that are mimicked by colloids are the "barometric distribution" of gas molecules in

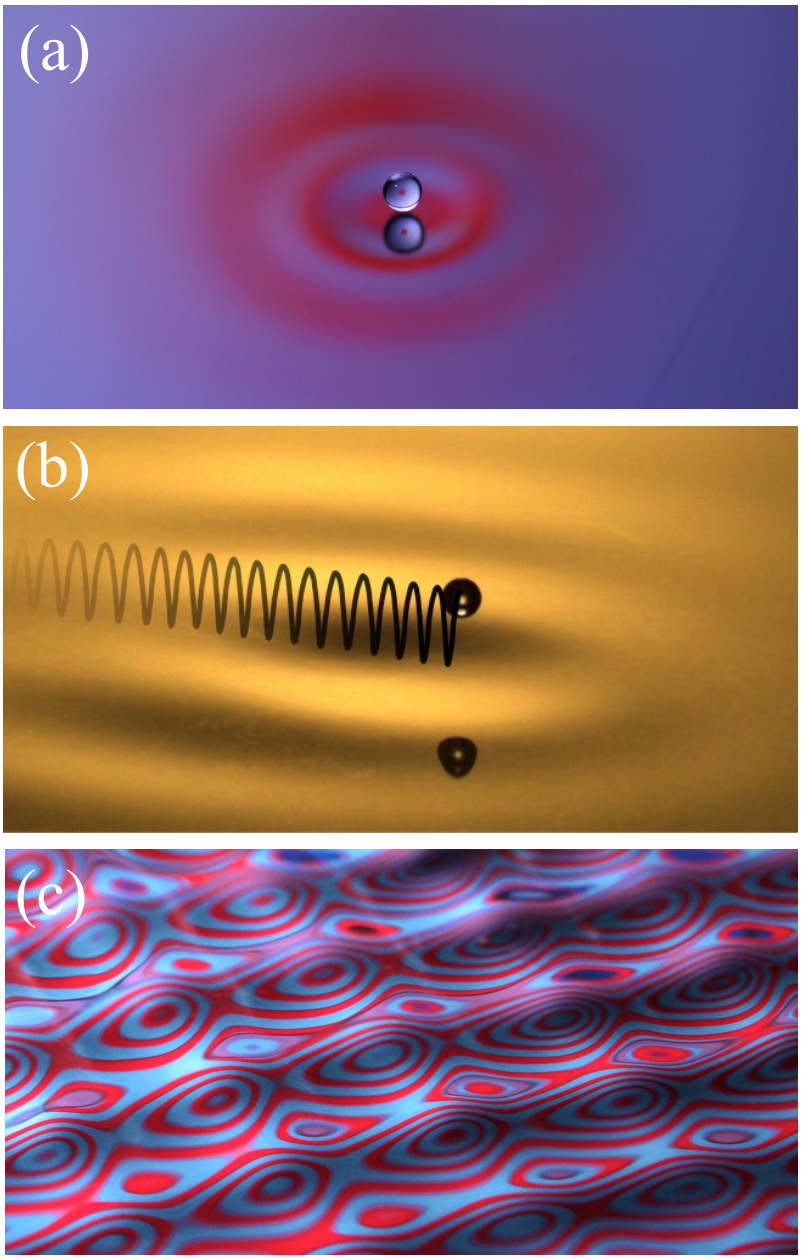

Figure 1.1 (a) A silicone oil drop bounces on the surface of a vertically vibrating fluid bath above a critical value of the forcing acceleration. Picture taken from [18]. (b) A drop may walk along the fluid interface while bouncing. Its trajectory is indicated by the black line. Picture taken from [21]. (c) If the bath is shaken with a sufficiently large acceleration, Faraday waves emerge on the free surface [46]. Picture taken from [58].

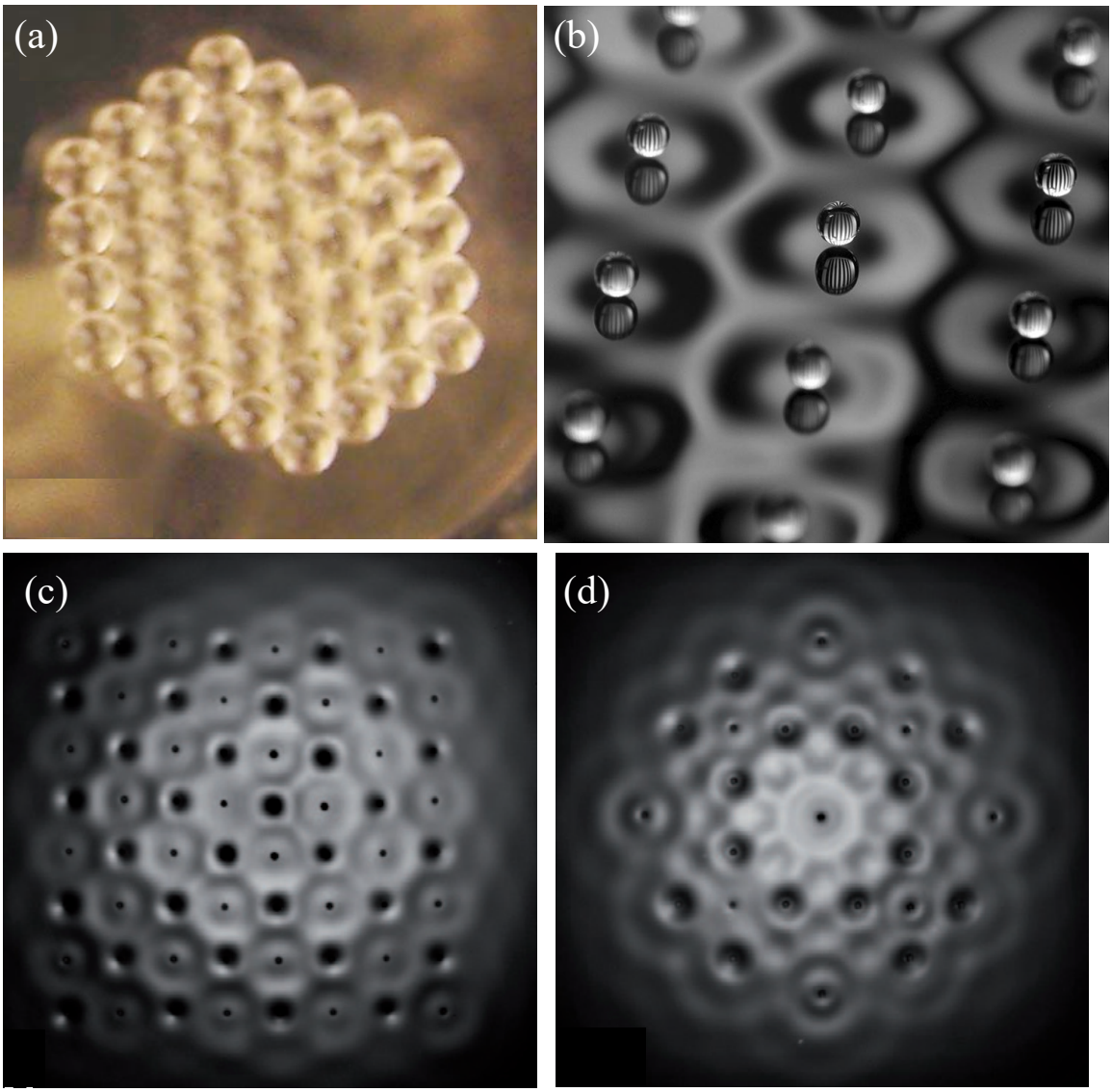

Figure 1.2 (a) Densely packed lattice of bouncing droplets, taken from Lieber *et al.* [76]. (b) Loosely packed lattice of bouncing droplets, taken from Harris *et al.* [56]. (c) In Eddi *et al.* [37], it was shown that two-square sub-lattices bouncing out of phase together comprise a square lattice. (d) A more exotic Archimedean tiling was achieved in [37].

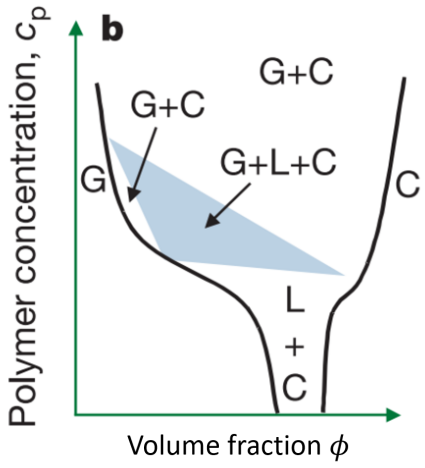

Figure 1.3 Phase diagram [9] for a colloid-polymer suspension in which the polymers are large relative to the colloids. ϕ denotes the colloid volume fraction, the ratio of colloidal particles to total volume in the mixture. Large values of ϕ correspond to a crystal phase (denoted by C in the diagram), while lower values correspond to a liquid phase (L) and the lowest ϕ-values correspond to a gas phase (G). The shaded region represents the three-phase region, *i.e.,* values of ϕ and c_p for which all three phases (crystal, liquid, and gas) may coexist simultaneously.

a constant-temperature atmosphere in gravity, and vapor-liquid interfaces [89]. The fact that the colloidal particles are macroscopic makes colloids much easier to observe than atomic systems, and yet their behavior is such that Wilson Poon described them as "big atoms" [89].

Experiments with colloids have applications in fields such as materials science, engineering, and pharmaceuticals, and the phase transition behavior of a colloidal suspension provides valuable insight into atomic-scale phase transitions. Understanding phase transitions on an atomic scale is extremely useful in making and working with materials that are used to manufacture electronics and other products that we use in our everyday lives.

The addition of non-adsorbing polymers to a colloidal suspension induces attractive forces between colloidal spheres originating from the presence of depletion zones around the spheres. This mechanism will be explained further in Chapter 4.

For a system in which the polymers are large in comparison to the colloidal particles (ratio of polymer size to colloid particle size > 0.3), a three-phase (gas, liquid, and crystal) coexistence occurs [9, 12] (Figure 1.3), corresponding to relatively low (gas), intermediate (liquid), and large (crystal) colloid concentrations, respectively. Note the contrast to a colloidal suspension without added polymer, in which only two phases (gas and crystal) may be present. Since the phase transition process in experiments performed on earth tends to be impeded by the effects of gravity, experiments are performed in space by NASA, onboard the ISS—an environment in which the colloids may form complex crystal structures.

Our research objectives in Chapter 4 are twofold. First, we develop and implement an image-processing algorithm to enhance photographic images of phase separation in colloid-polymer systems obtained by NASA on the International Space Station. We use the enhanced images to quantify the rate of phase separation as the experiment progresses. Second, we develop a phase-field model for the phase separation dynamics, taking particular care to incorporate hydrodynamic effects, and simulate the model numerically. The theoretical predictions are then compared with the experimental observations.

CHAPTER 2

CHAOTIC TRAJECTORIES OF A WALKING DROPLET

2.1 Introduction and Background

In this chapter, we construct and analyze an approximation to the so-called "stroboscopic model" for walking droplets, which was first proposed by Oza *et al.* [82] and is described in Section 2.2. The stroboscopic model has successfully been used to model the dynamics of a walking droplet in a rotating frame [81, 84] and central spring force [69], and the orbiting [83] and promenading [26, 10] bound states of pairs of walkers. Unfortunately, because the model is an integro-differential equation, solving it is computationally expensive. The goal of this chapter is to derive an analytical approximation to the stroboscopic model, and ascertain the degree to which it faithfully captures the walker dynamics.

After deriving the approximation in Section 2.3, we will simulate in Section 2.4 the resulting equations for a walker in a central force, $\mathbf{F} = -k\mathbf{x}$, a canonical problem in quantum mechanics. Such a force was realized in the experiments of Perrard *et al.* [88], who encapsulated a drop of ferrofluid within a larger droplet of silicone oil and subjected the droplet to a magnetic field. They found that, under the influence of the central harmonic force, the droplet executed one of four periodic trajectories, depicted in Figure 2.1(a). These orbits were found to be doubly quantized in their mean radius $\overline{R}$ and angular momentum $\overline{L}_z$, a result reminiscent of the doubly quantized solutions to the quantum harmonic oscillator problem. Moreover, Perrard *et al.* [88] found that, as the forcing acceleration of the bath was progressively increased, the droplet's motion became chaotic (Figure 2.1(b,c)); however, the chaotic trajectories were composed of excursions between the periodic trajectories depicted in Figure 2.1(a). This behavior is depicted qualitatively in Figure 2.1(b,c), and quantitatively in

Figure 2.1(d), the last of which shows that the chaotic walker's angular momentum switches between values consistent with those of the periodic trajectories. A prior study [110] investigated the manner in which the walker's trajectories become chaotic as the forcing acceleration is progressively increased; we study the transition to chaos in Section 2.4, and compare our results to [110] in Section 2.5.

2.2 The Stroboscopic Model

Consider a droplet of mass m and radius R, bouncing on the surface of a bath of the same fluid in the presence of a gravitational acceleration g. The bath is subjected to a vertical acceleration $\gamma \sin(2\pi f_0 t)$, and has surface tension σ, density ρ, kinematic viscosity ν, and depth H. Provided $\gamma < \gamma_F$, with γ_F being the Faraday instability threshold [46], the surface of the bath would remain flat if not for the presence of the drop perturbing the surface when it bounces. We assume the droplet to be in a so-called $(2,1)$ bouncing mode, where the (i,j) notation indicates that the drop's vertical motion has period equal to i driving periods, and within this period the drop contacts the bath j times [53]. The drop's bouncing period $T_F = 2/f_0$ is thus equal to the bath's least stable Faraday mode [15, 67, 66], whose wavelength $\lambda_F = 2\pi/k_F$ may be approximated by the water-wave dispersion relation

$$(\pi f_0)^2 = \left(g k_F + \frac{\sigma}{\rho} k_F^3 \right) \tanh(k_F H) \tag{2.1}$$

for this system [78].

Following the theoretical developments of Moláček & Bush [78] and letting $\mathbf{x} = \mathbf{x}(t)$ denote the droplet's position in the xy-plane at time t, we assume that the drop moves in response to two forces: a wave force $-mg\nabla h(\mathbf{x},t)$ proportional to the local slope of the wave field $h(\mathbf{x},t)$, and a drag $-D\dot{\mathbf{x}}$ induced during impact and flight. Averaging the horizontal forces over the bouncing period yields an integro-differential

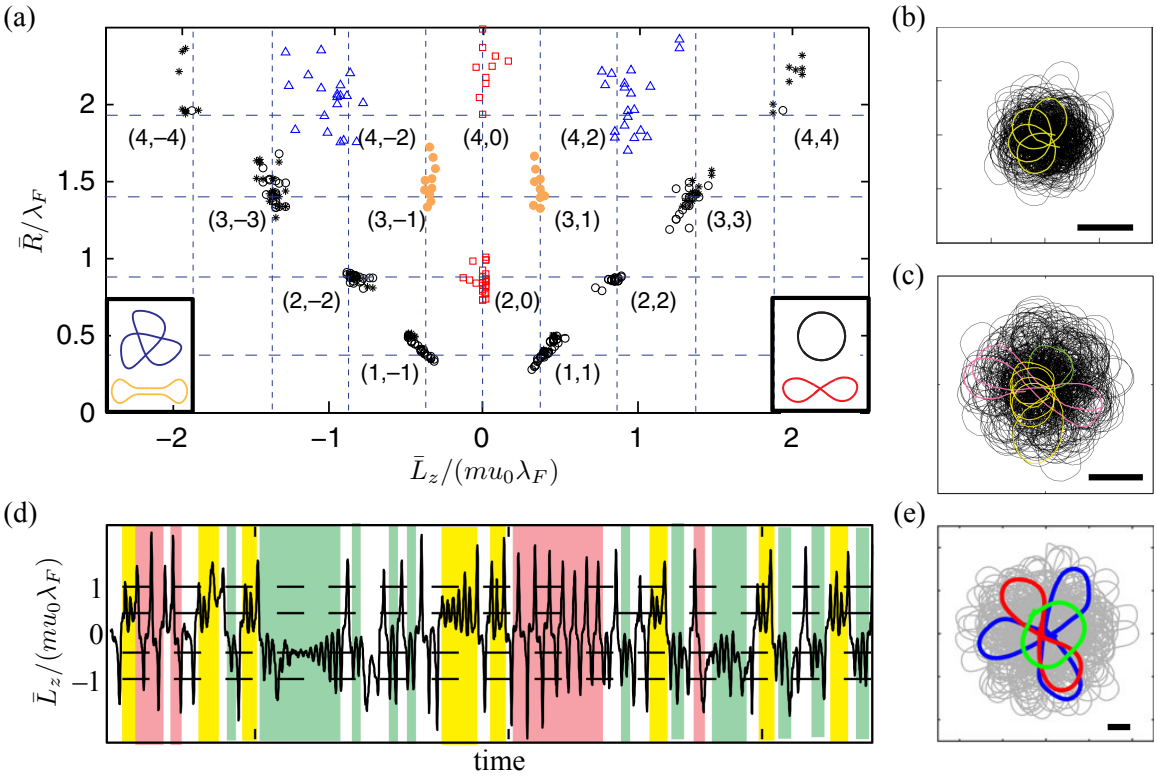

Figure 2.1 A summary of the phenomena observed in experiments on a walking droplet in a central spring force $\mathbf{F} = -k\mathbf{x}$. (a) The mean radius $\overline{R}$ and angular momentum $\overline{L}_z$ of periodic orbits captured over a range of forcing accelerations γ/γ_F and spring constants k, as obtained in experiments [88]. Four different types of orbits were observed: circular orbits (black), lemniscates (red), trefoils (blue) and dumbbells (orange), as shown in the legend. Two different chaotic trajectories are shown in panels (b) and (c) for two different values of the spring constant k. The time-evolution of the angular momentum of the trajectory in panel (c) is shown in panel (d). The trajectory is color-coded by sub-trajectories with different quantized values of $\overline{R}$ and $\overline{L}_z$. Specifically, $(\overline{R}/\lambda_F, \overline{L}_z/mu_0\lambda_F) \approx (1,1)$ (yellow) corresponds to a clockwise circular orbit); $(1,-1)$ (green) to a counterclockwise circular orbit; and $(2,0)$ (pink) to a lemniscate. Scale bars denote the Faraday wavelength λ_F in panels (b), (c) and (e). These three sub-trajectories were obtained in numerical simulations in Durey *et al.* [35]. The Faraday wavelength, walker mass and walker free speed are denoted by λ_F, m and u_0, respectively. Figure and caption are drawn from Bush *et al.* [23].

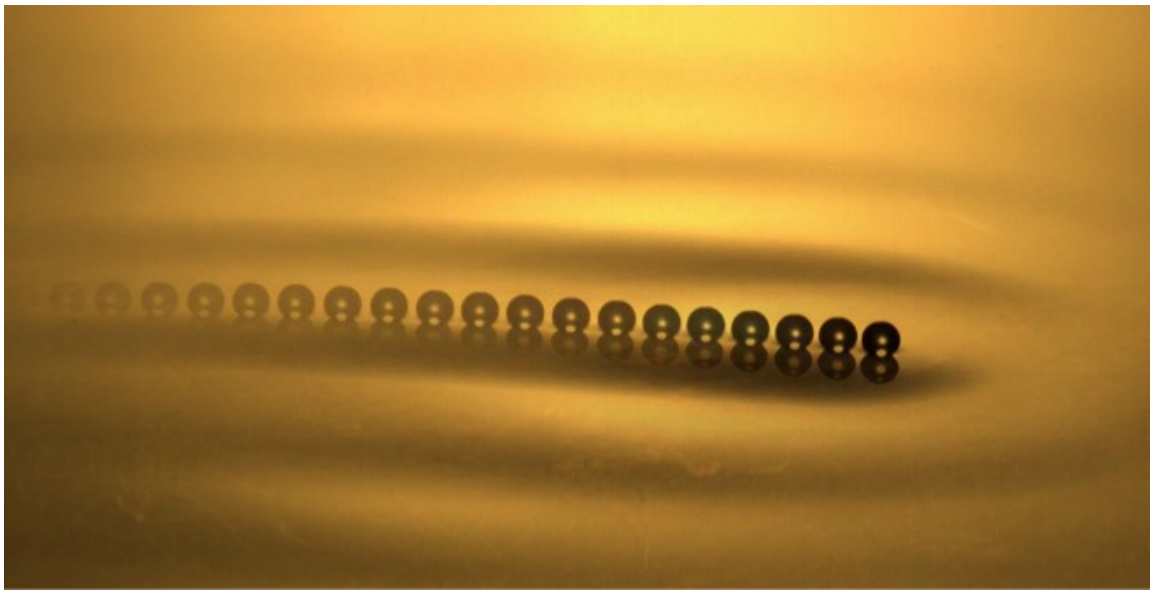

Figure 2.2 A strobe image of a walker surfing on the fluid interface, which offers a visualization of the strobscopic model described in Section 2.2. Picture taken from [21].

trajectory equation for the droplet's horizontal position [82]:

$$m\ddot{\mathbf{x}} + D\dot{\mathbf{x}}_i = -mg\nabla h(\mathbf{x},t), \quad h(\mathbf{x},t) = \frac{A}{T_F}\int_{-\infty}^{t} \mathrm{J}_0[k_F(\mathbf{x}-\mathbf{x}(s))]\mathrm{e}^{-(t-s)/T_M}\,\mathrm{ds}. \quad (2.2)$$

The drop is assumed to generate monochromatic standing waves with spatial profile $\mathrm{J}_0(k_F\mathbf{x})$ and decay time T_M, where J_0 is a Bessel function of the first kind. We assume the wave field to be linear, so that $h(\mathbf{x},t)$ may be expressed as the sum of waves generated prior to time t. The wave field in Equation (2.2) is obtained by approximating the resulting discrete sum as an integral, an approximation that is valid provided the timescale of horizontal motion is much greater than the bouncing period, $\lambda_F/|\dot{\mathbf{x}}_p| \gg T_F$, as is the case in the experiments. The trajectory equation (2.2) is referred to as the *stroboscopic model*, as we have effectively eliminated consideration of the drops' vertical motion by averaging over the vertical dynamics, and model the drops as continuous moving sources of standing waves. Figure 2.2 shows a visualization of the stroboscopic model.

The drag coefficient D, memory time T_M and wave amplitude A are given by the formulas [40, 78]

$$D = Cmg\sqrt{\frac{\rho R}{\sigma}} + 6\pi\mu_a R\left(1 + \frac{\rho_a g R}{12\mu_a f}\right), \quad T_M = \frac{T_d}{1-\gamma/\gamma_F}$$
$$\text{and } A = \frac{\sqrt{8\pi\nu_e T_F}}{3}\frac{(k_F R)^3}{3k_F^2\sigma/(\rho g)+1}\sin\Phi. \tag{2.3}$$

Here, C is a dimensionless drag constant, ρ_a and μ_a are the density and dynamic viscosity of air, respectively, T_d is the viscous decay time of the surface waves in the absence of forcing, ν_e is the bath's effective kinematic viscosity [78, 92] and $\sin\Phi$ is the sine of the droplet's impact phase. The first term in the formula for D results from the drag induced on the drop during its impact, the second from its free flight. Note that the memory time T_M increases as $\gamma \to \gamma_F$ from below, a regime in which the standing waves are more persistent. The terms "memory" and bath forcing acceleration are thus used interchangeably in what follows.

For the sake of simplicity, we neglect the effect of spatial damping, the exponential decay of surface waves in the far field that has been characterized experimentally [40, 33] and theoretically [77, 115, 109]. Indeed, the following analysis cannot be straightforwardly applied if spatial damping is included. We also neglect the dependence of the impact phase $\sin\Phi$ on both the forcing acceleration γ and the instantaneous wave height, effects that have been quantified in recent experiments [27]. Impact phase variations have been shown to influence the stability of the orbital [83] and promenade [10] modes executed by pairs of walking droplets, and of free rings of bouncers [26].

We proceed by non-dimensionalizing the trajectory equation using the Faraday wavelength and memory time, and so let $\mathbf{x} \to k_F\mathbf{x}$ and $t \to t/T_M$ in Equation (2.2). The dimensionless trajectory equation is thus

$$\kappa\ddot{\mathbf{x}}(t) + \dot{\mathbf{x}}(t) = -\beta\nabla\int_{-\infty}^{t} \mathrm{J}_0(|\mathbf{x}-\mathbf{x}(s)|)\mathrm{e}^{-(t-s)}\,\mathrm{ds}\Big|_{\mathbf{x}=\mathbf{x}(\mathrm{t})} \tag{2.4}$$

where $\kappa = m/DT_M$ is the dimensionless mass and $\beta = mgAk_F^2T_M^2/DT_F$ the dimensionless wave force coefficient. For this study, we adopt fluid parameters comparable to those used in typical experiments [93, 78, 55, 112, 26]. Specifically, we assume that the fluid bath of depth $H = 4$ mm consists of silicone oil with viscosity $\nu = 20$ cSt driven at $f_0 = 80$ Hz, with associated Faraday wavelength $\lambda_F = 4.75$ mm and viscous decay time $T_d = 0.018$ s. We also assume the droplets to have radius $R = 0.4$ mm and mass $m = 0.25$ mg, for which the time-averaged drag is $D = 2.0$ mg/s and wave amplitude $A = 3.5$ μm through Equation (2.3). We adopt the value $\sin\Phi = 0.2$, which is roughly consistent with experimental measurements of the impact phase [27] and also provides adequate agreement between the predicted and observed speeds of walking droplets [78, 82]. For these parameter values, we obtain the formulas $\kappa \approx 7(1 - \gamma/\gamma_F)$ and $\beta \approx 0.1/(1 - \gamma/\gamma_F)^2$. For convenience, we will from now on denote the dimensional forcing acceleration γ by γ^* instead, and will refer to the *dimensionless* forcing acceleration as γ instead, *i.e.,* $\gamma = \gamma^*/\gamma_F$. We may think of this as the "memory parameter" since the fluid's memory increases as $\gamma \to 1$, *i.e.,* as $\gamma^* \to \gamma_F$.

The present study is concerned with walkers, so we restrict our attention to the parameter regime $\gamma > 0.78$. According to the regime diagrams presented by Moláček & Bush [78] and Wind-Willassen *et al.* [119], this value corresponds to the walking threshold $\beta = 2$ for a single drop [82], specifically, the critical vibrational acceleration above which the bouncing state destabilizes into a steadily translating walking state.

According to the experiments of Perrard *et al.* [88], an external force analogous to a (radial) linear spring force can be applied to the drop by putting some ferromagnetic fluid into the drop and subjecting the system to a radially non-uniform vertical magnetic field. Thus, the additional forcing term $\mathbf{F} = -k^*\mathbf{x}$ is introduced; we will take $k^* = 3.2\,\mu$N/m and denote the corresponding nondimensional spring force

as $k = k^* T_M / D$, where $T_M = T_F M_e$, and

$$M_e = \frac{T_d}{T_F(1 - \gamma^*/\gamma_F)}. \tag{2.5}$$

With this new external forcing, our trajectory equation becomes:

$$\kappa\ddot{\mathbf{x}}(t) + \dot{\mathbf{x}}(t) = -\beta\nabla \int_{-\infty}^{t} \mathrm{J}_0(|\mathbf{x} - \mathbf{x}(s)|)\mathrm{e}^{-(t-s)}\,\mathrm{ds}\Big|_{\mathbf{x}=\mathbf{x}(\mathrm{t})} - k\mathbf{x}(\mathrm{t}) \tag{2.6}$$

Integro-differential equations like this are difficult and computationally expensive to solve. To offset these computational costs, we will rewrite this equation in such a way that allows us to approximate it by a system of finitely many ordinary differential equations.

2.3 A Finite Mode Approximation

In this section we will describe the steps taken to obtain our approximation to the stroboscopic model, Equation (2.6). To start, since we are working with Bessel functions of the first kind, we will apply *Graf's Theorem* for the zeroth Bessel function of the first kind [6]:

$$J_0(|\mathbf{x} - \mathbf{y}|) = \sum_{n=-\infty}^{\infty} J_n(|\mathbf{x}|)J_n(|\mathbf{y}|) \cdot e^{in(\theta_x - \theta_y)} \tag{2.7}$$

where θ_x denotes the angle that the vector $\mathbf{x}$ forms with the positive x-axis.

Applying Equation (2.7) to Equation (2.6), we get:

$$\kappa\ddot{\mathbf{x}}(t) + \dot{\mathbf{x}}(t) = -\beta\nabla \int_{-\infty}^{t} \sum_{n=-\infty}^{\infty} J_n(|\mathbf{x}|)J_n(|\mathbf{x}(s)|)e^{in(\theta_{\mathbf{x}} - \theta_{\mathbf{x}(s)})}e^{-(t-s)}ds\Big|_{\mathbf{x}=\mathbf{x}(t)} - k\mathbf{x}(t). \tag{2.8}$$

Using Euler's Formula and several other familiar identities from trigonometry, along with the well-known identity $J_{-n}(x) = (-1)^n J_n(x)$ for Bessel functions, we can again

rewrite to get:

$$\kappa\ddot{\mathbf{x}}(t) + \dot{\mathbf{x}}(t) = -2\beta\nabla \int_{-\infty}^{t} \left[\frac{1}{2} J_0(|\mathbf{x}|) J_0(|\mathbf{x}(s)|) + \sum_{n=1}^{\infty} J_n(|\mathbf{x}|) J_n(|\mathbf{x}(s)|) \cdot \right.$$
$$\left. \cdot \ \left[\cos(n\theta_{\mathbf{x}}) \cos(n\theta_{\mathbf{x}(s)}) + \sin(n\theta_{\mathbf{x}}) \sin(n\theta_{\mathbf{x}(s)}) \right] \right] e^{-(t-s)} ds \Big|_{\mathbf{x}=\mathbf{x}(t)} - k\mathbf{x}(t) \tag{2.9}$$

Interchanging the summation and integral signs allows us to write the integral term on the right-hand side of Equation (2.9) as:

$$\begin{aligned} &- \beta\nabla \int_{-\infty}^{t} J_0(|\mathbf{x}|) J_0(|\mathbf{x}(s)|) ds \\ &- 2\beta\nabla \sum_{n=1}^{\infty} \left[\int_{-\infty}^{t} J_n(|\mathbf{x}|) J_n(|\mathbf{x}(s)|) \cos(n\theta_{\mathbf{x}}) \cos(n\theta_{\mathbf{x}(s)}) e^{-(t-s)} ds + \right. \\ &\left. + \int_{-\infty}^{t} J_n(|\mathbf{x}|) J_n(|\mathbf{x}(s)|) \sin(n\theta_{\mathbf{x}}) \sin(n\theta_{\mathbf{x}(s)}) e^{-(t-s)} ds \right] \Big|_{\mathbf{x}=\mathbf{x}(t)}. \end{aligned} \tag{2.10}$$

Taking the terms that are independent of s outside of the integral and evaluating $\mathbf{x}$ at $\mathbf{x}(t)$, we can write the summation term (the second term in Equation (2.10)) as follows:

$$\begin{aligned} -2\beta\nabla \sum_{n=1}^{\infty} \Bigg[& J_n(|\mathbf{x}(t)|) \cos(n\theta_{\mathbf{x}(t)}) \int_{-\infty}^{t} J_n(|\mathbf{x}(s)|) \cos(n\theta_{\mathbf{x}(s)}) e^{-(t-s)} ds + \\ & J_n(|\mathbf{x}(t)|) \sin(n\theta_{\mathbf{x}(t)}) \int_{-\infty}^{t} J_n(|\mathbf{x}(s)|) \sin(n\theta_{\mathbf{x}(s)}) e^{-(t-s)} ds \Bigg]. \end{aligned}$$

For convenience, we will define:

$$\begin{aligned} c_n(t) &:= \int_{-\infty}^{t} J_n(|\mathbf{x}(s)|) \cos(n\theta_{\mathbf{x}(s)}) e^{-(t-s)} ds, \\ d_n(t) &:= \int_{-\infty}^{t} J_n(|\mathbf{x}(s)|) \sin(n\theta_{\mathbf{x}(s)}) e^{-(t-s)} ds \end{aligned}$$

so we may write (2.9) as:

$$\begin{aligned} \kappa\ddot{\mathbf{x}}(t) + \dot{\mathbf{x}}(t) = & - \beta\nabla \left[c_0(t) J_0(|\mathbf{x}(t)|) \right] - 2\beta\nabla \sum_{n=1}^{\infty} \left[c_n(t) J_n(|\mathbf{x}(t)|) \cos(n\theta_{\mathbf{x}(t)}) + \right. \\ & \left. + d_n(t) J_n(|\mathbf{x}(t)|) \sin(n\theta_{\mathbf{x}(t)}) \right] - k\mathbf{x}(t). \end{aligned} \tag{2.11}$$

Applying the Leibniz Rule to compute the derivatives of $c_n(t)$ and $d_n(t)$ yields the first-order ordinary differential equations (ODEs):

$$\begin{aligned}\dot{c}_n(t) =& J_n(|\mathbf{x}(t)|)\cos(n\theta_{\mathbf{x}(t)}) - c_n(t)\\ \dot{d}_n(t) =& J_n(|\mathbf{x}(t)|)\sin(n\theta_{\mathbf{x}(t)}) - d_n(t).\end{aligned} \tag{2.12}$$

Note that Equations (2.11) and (2.12) define a system of (infinitely many) ODEs. We now convert this system to polar coordinates to further simplify:

$$\begin{cases}\kappa(\ddot{r} - r\dot{\theta}^2) + \dot{r} = \beta c_0(t)J_1(r) \\ \qquad\qquad\qquad - \beta\displaystyle\sum_{n=1}^{\infty}\big[\big(c_n(t)\cos n\theta + d_n(t)\sin n\theta\big)\big(J_{n-1}(r) - J_{n+1}(r)\big)\big] - kr \\ \kappa(r\ddot{\theta} + 2\dot{r}\dot{\theta}) + r\dot{\theta} = -2\beta\displaystyle\sum_{n=1}^{\infty}\big[\tfrac{n}{r}J_n(r)\big(-c_n(t)\sin(n\theta) + d_n(t)\cos(n\theta)\big)\big],\end{cases}$$

$$\begin{cases}\dot{c}_n(t) = -c_n(t) + J_n(r)\cos(n\theta), \quad n = 0, 1, 2, 3, ... \\ \\ \dot{d}_n(t) = -d_n(t) + J_n(r)\sin(n\theta), \quad n = 1, 2, 3, ...\end{cases} \tag{2.13}$$

Although we now have a system of infinitely many ODEs in infinitely many unknowns, which is impossible to solve, we note that the Bessel functions J_n with large n are effectively zero except in the far field: specifically, $J_n(x) \sim \frac{1}{\Gamma(n+1)}\big(\frac{x}{2}\big)^n$ as $x \to 0$. This leads us to make an approximation: we truncate the infinite system above and retain a finite number of terms N. Thus, we have:

$$\begin{cases}\kappa(\ddot{r} - r\dot{\theta}^2) + \dot{r} = \beta c_0(t)J_1(r) \\ \qquad\qquad\qquad - \beta\displaystyle\sum_{n=1}^{N}\big[\big(c_n(t)\cos n\theta + d_n(t)\sin n\theta\big)\big(J_{n-1}(r) - J_{n+1}(r)\big)\big] - kr \\ \kappa(r\ddot{\theta} + 2\dot{r}\dot{\theta}) + r\dot{\theta} = -2\beta\displaystyle\sum_{n=1}^{N}\big[\tfrac{n}{r}J_n(r)\big(-c_n(t)\sin(n\theta) + d_n(t)\cos(n\theta)\big)\big],\end{cases}$$

$$\begin{cases}\dot{c}_n(t) = -c_n(t) + J_n(r)\cos(n\theta), \quad n = 0, 1, 2, 3, ...N \\ \\ \dot{d}_n(t) = -d_n(t) + J_n(r)\sin(n\theta), \quad n = 1, 2, 3, ...N\end{cases} \tag{2.14}$$

Note that the system (2.14) is a system of $2N+3$ ODEs in $2N+3$ unknowns. Choosing an appropriate N that will preserve the behaviors of the system described by Equation (2.6) without being too computationally expensive has been somewhat of a trial-and-error process, but we were able to get an idea of how large N should be by solving a simplified, time-independent version of the system (2.14). We will now discuss this simplified system in Subsection 2.3.1.

2.3.1 Circular orbit solutions

Labousse *et al.* [68] substituted a constant-radius, constant-angular frequency ansatz $\mathbf{x} = (r_0 \cos \omega t,\ r_0 \sin \omega t)$ into Equation (2.6). The result is a system of 2 algebraic equations in 2 unknowns:

$$\begin{cases} -\kappa r_0 \omega^2 = \beta \displaystyle\int_0^\infty J_1(2r_0 \sin \frac{\omega z}{2}) \sin \frac{\omega z}{2} e^{-z} dz - k r_0 \\ \\ r_0 \omega = \beta \displaystyle\int_0^\infty J_1(2r_0 \sin \frac{\omega z}{2}) \cos \frac{\omega z}{2} e^{-z} dz \end{cases} \tag{2.15}$$

which may be solved numerically to obtain constant-radius solutions. Note that these solutions correspond to an orbital trajectory whose radius r_0 remains constant for all time, and whose angle θ changes at a constant rate, *i.e.,* $\theta = \omega t$. In other words, the solutions to this system do not depend on time.

Substituting the ansatz $\mathbf{x} = (r_0 \cos \omega t,\ r_0 \sin \omega t)$ into our approximate system (2.14) gives us the algebraic system:

$$\begin{cases} \kappa r_0 \omega^2 + \beta J_0(r_0) J_1(r_0) - 2\beta \displaystyle\sum_{n=1}^{N} \left[J_n(r_0) \frac{1}{1+(n\omega)^2} \right] \left[\frac{1}{2}(J_{n-1}(r_0) - J_{n+1}(r_0)) \right] - k r_0 = 0 \\ \\ -r_0 \omega + 2\beta \displaystyle\sum_{n=1}^{N} \frac{n}{r_0} (J_n(r_0))^2 \frac{n\omega}{1+(n\omega)^2} = 0 \end{cases} \tag{2.16}$$

Both of the systems (2.15) and (2.16) are easily solved in MATLAB. The question that remains is what to choose for N in the approximation. Figures 2.3 and 2.4 show

plots of both r_0 and ω, respectively, plotted against the spring constant k—for several values of N and also for the exact system (2.15). We note that the axes in both figures are dimensionless: $k = (\frac{T_M}{D})k^*$, $r_0 = {r_0}^*/\lambda_F$ and $\omega = T_M\omega^*$, where the stars denote dimensional values.

For the discussion that follows, it is important to recall the concept of *memory* discussed in Section 2.1, and its relation to the memory parameter (bath forcing acceleration) γ: for higher γ, *i.e.,* γ close to 1, the system has high memory (in other words, the standing waves on the surface take longer to dissipate). For lower γ, the system has low memory (the standing waves dissipate quickly). As seen in Figures 2.3 and 2.4, we consider several memory regimes: that of relatively low memory ($\gamma = 0.82$), mid-memory ($\gamma = 0.94$), and high memory ($\gamma = 0.98$). As was observed in prior work [69], the exact solutions exhibit more oscillatory behavior in k as the memory is progressively increased. In general, we see that increasing the radial spring force k causes the orbital radius r_0 to become smaller and the angular frequency ω to become larger. An interesting feature of the system is that the number of terms N required to have a good approximation decreases as the forcing acceleration γ is increased. As is evident from Figure 2.3, a relatively small number of terms N is sufficient to capture the behavior of circular orbits for small r_0, while a higher value of N is required to accurately characterize larger orbits.

2.4 Time-Dependent Simulations

We will now present and discuss the more general, time-dependent solutions $\mathbf{x}(t) = \big(r(t)\cos\theta(t),\ r(t)\sin\theta(t)\big)$. To solve the time dependent system (2.14), we used an ODE solver in MATLAB based on Runge-Kutta methods for timestepping. For the initial condition, we first solved the (much simpler) time-independent system (2.16), discussed in Subsection 2.3.1, in which the solutions are assumed to be orbits of constant radius r_0 and constant angular frequency ω, which is simply an algebraic

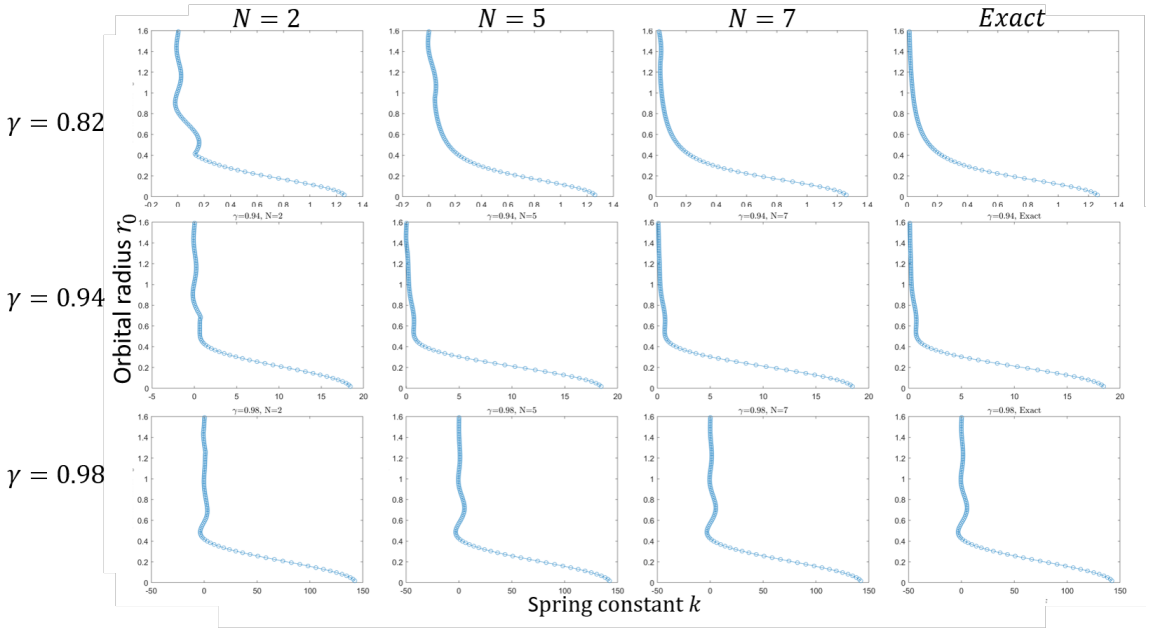

Figure 2.3 Plots of orbital radius r_0, plotted against spring constant k, for the systems (2.15) and (2.16). Note how in general, the orbital radius decreases with larger forcing k. The rows correspond to different memory parameter values γ, and the columns correspond to different values N of terms kept in the summation in (2.16), with the final column on the right corresponding to the exact solution obtained by solving (2.15). As we expect, keeping more terms leads to a more accurate plot.

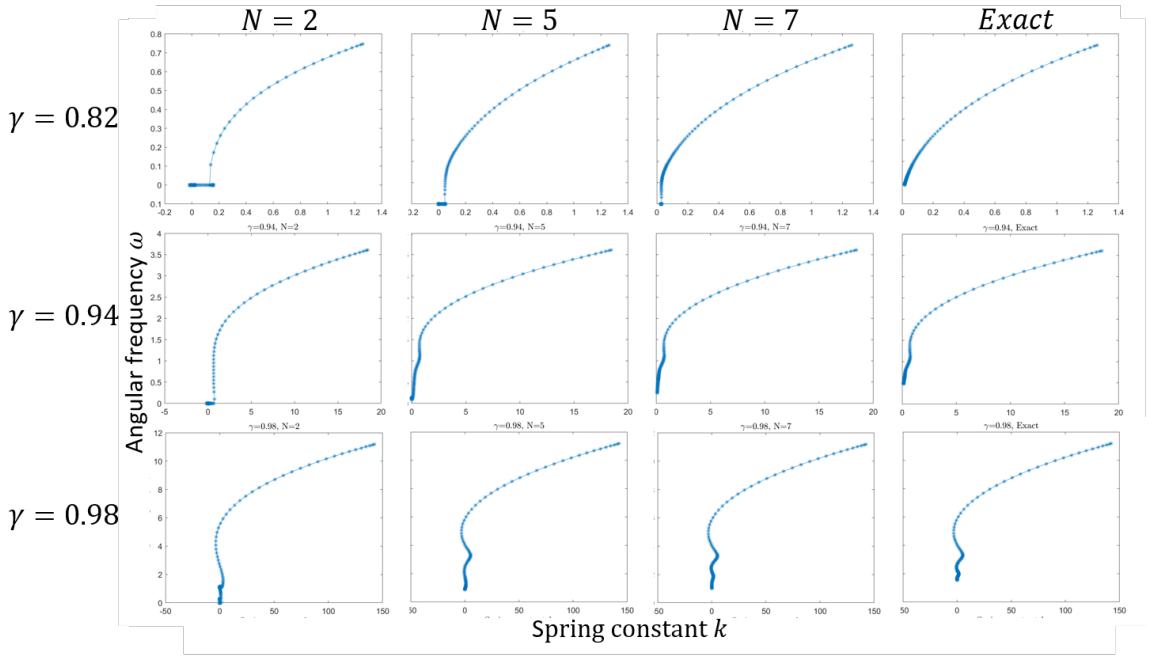

Figure 2.4 Plots of orbital angular frequency ω, plotted against spring constant k, for the systems (2.15) and (2.16). The angular frequency increases as the radial forcing k is increased. As in Figure 2.3, the rows correspond to different γ-values and the columns correspond to different N-values for (2.16).

system of 2 equations in 2 unknowns. Based on the results in Figures 2.3 and 2.4, we chose for our approximate model $N = 7$, *i.e.,* retaining the first 7 terms in each of the summations. We are thus solving a system of $2N+3 = 17$ ODEs in 17 unknowns. We then solved the system (2.14) using the initial values $r = r_0$, $\dot{r} = 0$ (corresponding to constant-r case), $\theta = 0$, and $\dot{\theta} = \omega$ with r_0 and ω obtained from solving (2.16). The initial values $c_n(0)$ and $d_n(0)$ are obtained by simply plugging in $r = r_0$ and $\theta = \omega t$ to the definitions of $c_n(t)$ and $d_n(t)$, which can be evaluated exactly for constant r_0 and ω.

Figure 2.5 shows a drop's trajectory, plotted from $t = 0$ to $t = 100$, for $\gamma = 0.940$. Note that at first, the solver has some difficulty finding the correct radius, but it quickly settles into a stable, circular orbit, as can be seen both in the trajectory plot in the xy-plane (left) and in the $r(t)$ vs. t plot, where $r(t) = \sqrt{(x(t))^2 + (y(t))^2}$.

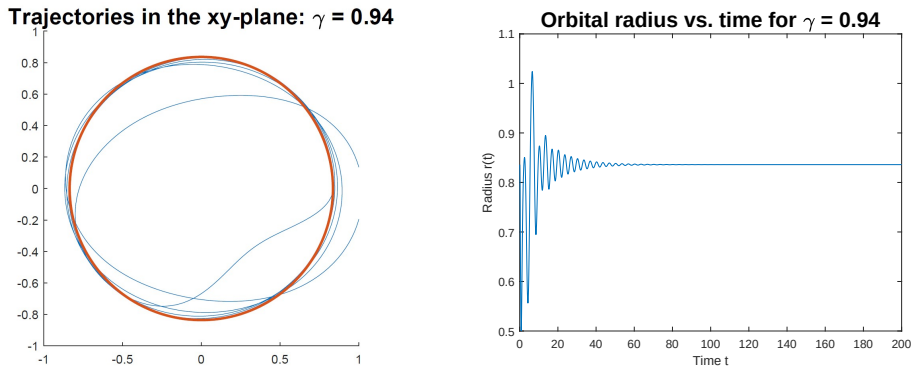

Figure 2.5 Plots of (left) a droplet's trajectory in the xy-plane, and (right) the orbital radius of the trajectory vs. time, for $\gamma = 0.94$. This is a stable, circular orbit of constant angular frequency.

2.5 Comparison of Results

We now present and discuss the results of our simulations of our finite approximation model, *i.e.* the system (2.14), and then compare these with the results obtained by Tambasco *et al.* [110] from the full model, Equation (2.6). To that end, we consider in Figure 2.6 the trajectories in the truncated system for a few different values of the memory parameter γ.

As we discussed in Section 2.1 and Subsection 2.3.1, the memory parameter γ dictates how long it takes for the wave field excited by the droplet to decay, and thus influences the behavior of the system. For lower values of γ (low memory), a single droplet is observed to travel in a stable, circular orbit. As γ is increased, the orbits begin to destabilize into a "wobbling state", and in the high-memory regime, other interesting behaviors become present—for γ near 1, chaotic trajectories are observed [110].

In order to see how many frequencies are present in the orbital radius $r(t)$ for higher values of γ, we computed the fast Fourier transform (FFT) of $r(t)$ and plotted the power spectrum. Figure 2.6 shows simulation results of the approximate system (2.14) for five different values of γ (represented by the rows in the figure). The first column shows the drop's trajectory (orbits) in the xy-plane, the second column

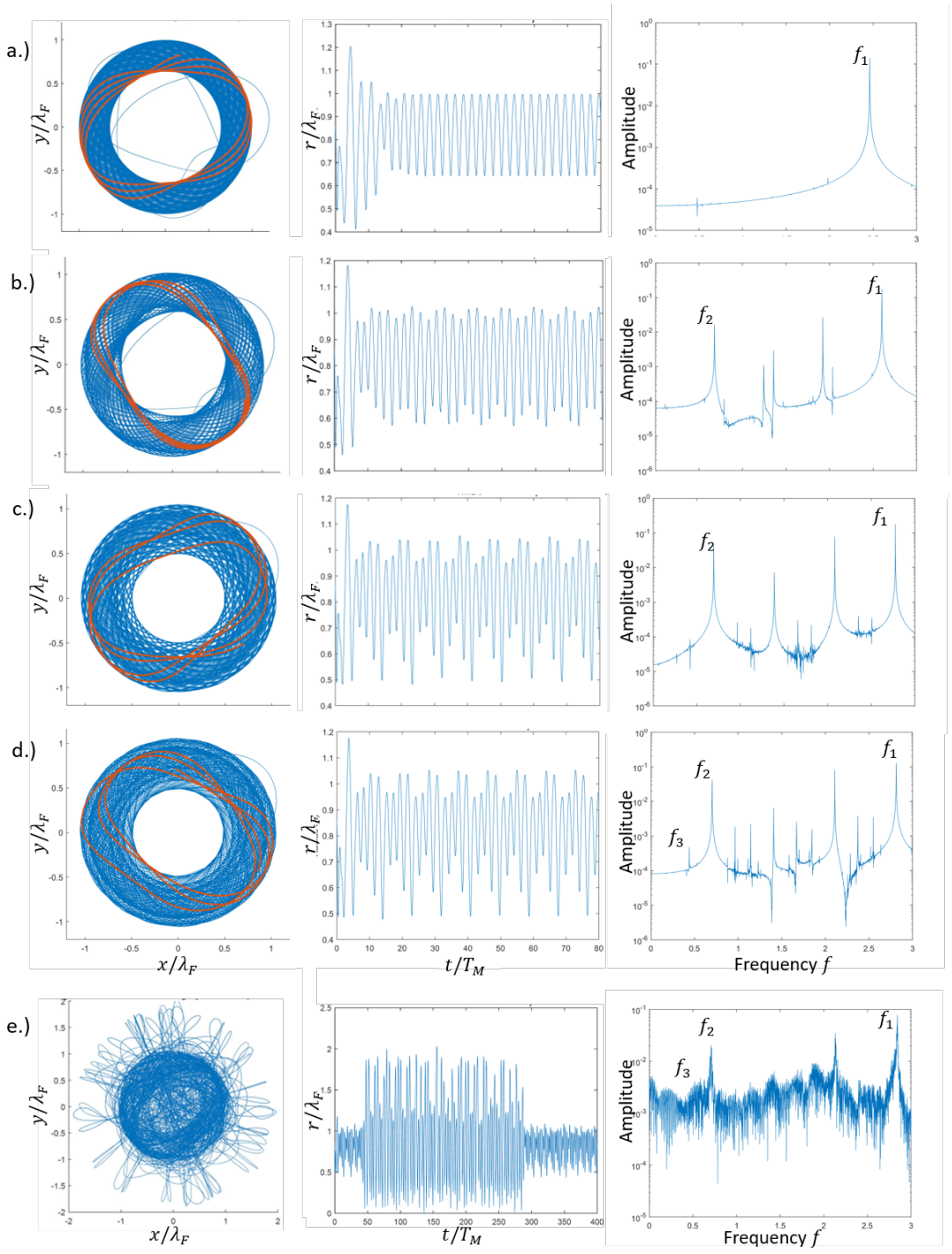

Figure 2.6 Plots of (left column): the droplet's trajectory in the xy-plane; (middle column) the orbital radius $r(t)$ of the trajectory vs. time, and (right column) the frequency spectrum of $r(t)$, for five different values of γ resulting in (from top to bottom): a.) an unstable wobbling orbit whose radius $r(t)$ is periodic in t; b.) an unstable wobbling orbit whose radius $r(t)$ is now *quasiperiodic*, having two frequencies; c.) a period-locked orbit; d.) an orbit whose radius $r(t)$ has three frequencies; and e.) a chaotic trajectory. The red curves in the trajectory plots highlight the last few orbits plotted, making the shape of the orbits more visible.

shows the orbital radius $r(t)$ plotted against time, and the third column shows the frequency spectrum of the radius $r(t)$.

The first row in Figure 2.6 corresponds to $\gamma = 0.955$; note that the trajectory is unstable: in contrast to Figure 2.5, it forms orbits that are no longer circular and that "wobble". The last few orbits are highlighted in red so this can be seen more easily. The plot of orbital radius $r(t)$ vs. t shows that the radius of the orbits is not constant, but $r(t)$ is periodic; the power spectrum shows only one peak, indicating that $r(t)$ oscillates periodically with a single frequency $f_1 \approx 2.46$. In the second row of Figure 2.6, γ is increased to 0.958. For this higher-memory simulation, notice that the radius $r(t)$ of the orbits is no longer periodic, but instead becomes quasiperiodic, having multiple frequencies instead of just one. This can be seen more clearly by looking at the power spectrum, which shows *two* frequency peaks, $f_1 \approx 2.6$ and $f_2 \approx 0.68$; note that the other peaks in the plot are linear combinations of these two. The third row ($\gamma = 0.960$) shows similar behavior: the power spectrum plot shows that $r(t)$ still oscillates with two frequencies f_1 and f_2 present; both have increased from $\gamma = 0.958$ to $\gamma = 0.960$ ($f_1 \approx 2.8$, $f_2 \approx 0.69$). However, a new feature has arisen: notice that $f_1 \approx 4f_2$. This is similar to the "frequency locking" [110] at high γ-values seen in the simulations of the full stroboscopic model (2.6). Though the fourth row ($\gamma = 0.9604$) has similar features to $\gamma = 0.960$, including the frequency locking between f_1 and f_2 in $r(t)$, we now observe the appearance of a third frequency $f_3 \approx 0.44$ in the power spectrum that was absent for $\gamma = 0.960$. The final row, $\gamma = 0.9608$, shows the onset of chaos—instead of distinct frequency peaks as in the other power spectrum plots, there is a broad spectrum of frequencies, as is characteristic of chaos. This pathway to chaos is reminiscent of the so-called Ruelle-Takens-Newhouse scenario [102], wherein a finite sequence of bifurcations gives rise to additional frequencies in the spectrum and after three such bifurcations, it is likely (but not guaranteed) that the system achieves a chaotic state.

2.6 Discussion and Future Work

We have presented an approximation to the integro-differential governing equation for droplet trajectories. Our approximation is somewhat flexible in that the number of terms retained in the sum may be changed, but we have found that for the parameters given in Section 2.2, keeping $N = 7$ terms in the sum yields simulation results that are qualitatively very similar to the results given by the full model [110], and are not far off quantitatively either.

Tambasco *et al.* include a plot [110] of the frequency of $r(t)$ as a function of γ. This plot is given in Figure 2.7. Note that, just as we saw in our simulations, at the onset of instability, $r(t)$ oscillates with a single frequency f_1, which changes slightly as γ is increased. At a certain value of γ, another frequency becomes present, making the plot of $r(t)$ quasiperiodic. This new frequency f_2 also increases as γ is increased, but the ratio f_2/f_1 decreases until f_2 is 1/4 the value of f_1. The ratio f_2/f_1 then "locks in" so that f_2 is always 1/4 the value of f_1, even as γ continues to be increased. At some higher value of γ, just before the onset of chaos, a third frequency f_3 appears.

We made a similar plot using our approximate model, *i.e.* the system (2.14); this plot is shown in Figure 2.8. There are a few quantitative differences: the values of f_3 in Figure 2.8 are roughly twice those in Figure 2.7, and the values of γ for which behaviors occur for the two plots are slightly different. In spite of this, the behaviors are qualitatively similar: specifically, the appearance of f_2, followed by the frequency locking between f_1 and f_2 at $f_1 = 4f_2$, and finally the appearance of f_3 just before chaos. The droplet trajectories simulated using our (approximate) system of 17 ODEs in 17 unknowns are thus seen to exhibit very similar behavior as is seen when using the full stroboscopic model, Equation (2.6).

We hope that our approximate model may be used in the future to simulate systems with many drops, such as chains [112], rings [26], and two-dimensional

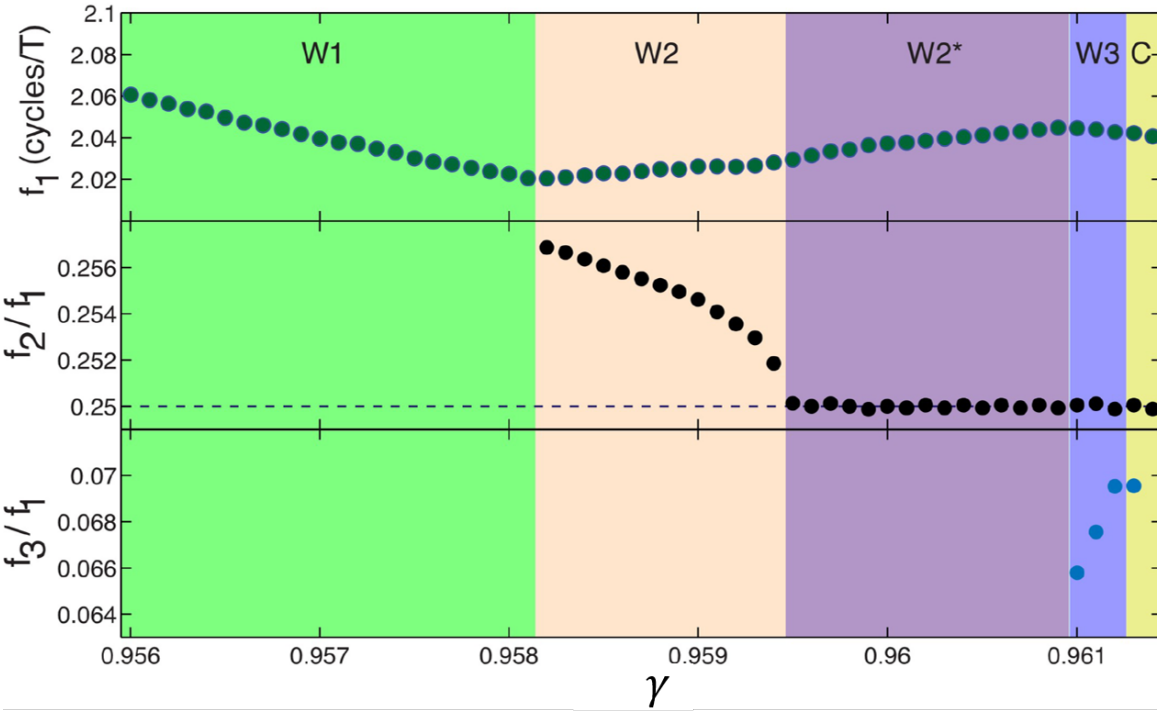

Figure 2.7 A plot from Tambasco *et al.* [110] of the frequencies of $r(t)$ as a function of γ, as obtained by identifying the peak frequencies in the power spectrum. As explained in the figure caption in Tambasco *et al.* [110], the top panel tracks the principal wobbling frequency f_1, which first appears when the circular orbit becomes unstable. As the forcing acceleration is increased further, a second independent frequency f_2 appears, which later becomes locked with f_1 at $f_2/f_1 = 1/4$, as shown in the second row. At higher accelerations, a third independent frequency f_3 appears that precedes the transition to a broadband spectrum in the chaotic regime, as shown in the third row. W1 is the single-frequency state, W2 the two-frequency quasiperiodic state, W2* the two-frequency frequency-locked state, W3 the state with a third incommensurate frequency, and C the chaotic orbital state. Note that, for the lower values of γ shown on this axis, only f_1 is present.

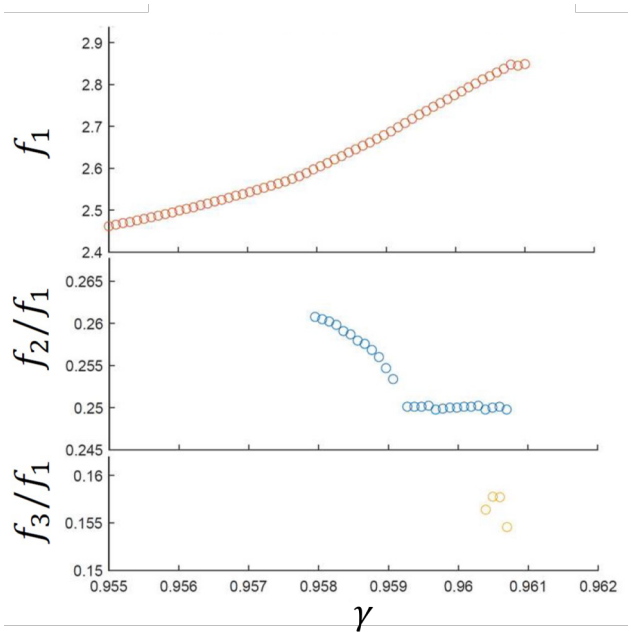

Figure 2.8 A plot similar to that in Figure 2.7, but using the approximate system (2.14). Note the qualitative similarity between this plot and the one in Figure 2.7.

(2D) lattices [94, 76, 41, 37], all of which would be difficult to simulate using the stroboscopic model due to the computational expense of solving an integro-differential equation. We also note that we ran several simulations of the approximate system with only $N = 3$ terms, but we found that the trajectories were significantly different from those of the full model, even by eye. Still, the number N of terms retained in the sum can be experimented with to allow for even less computation time, and a lower N (*i.e.,* $N < 7$) may afford a good approximation in certain parameter regimes.

CHAPTER 3

RESONANT INTERACTIONS IN DROPLET CHAINS

The discussion in this chapter is drawn from the paper "Resonant interactions in bouncing droplet chains" by L. Barnes, G. Pucci, and A. U. Oza, published in Comptes Rendus Mécanique [13].

3.1 Introduction and Background

In Chapter 2, we discussed the behaviors of a single walking droplet on the surface of a vertically vibrated fluid bath. In this chapter, we consider a one-dimensional (1D) chain of such droplets, in which each drop interacts not only with its own wave field, but also with the waves produced by the other drops in the chain. 1D rings and chains of bouncers and walkers have been shown to exhibit rich phenomenology. Strings of up to eleven walkers confined to a circular annulus move faster than an individual walker, with the speed increasing with the number of walkers [47, 97]. Thomson *et al.* [112] demonstrated that a ring of twenty bouncers confined within an annulus may exhibit small-amplitude binary oscillations, whereas a ring of forty bouncers exhibits a striking solitary wave-like instability (Figure 3.1(e)–(g)). Free rings of bouncing droplets destabilize into a variety of dynamical states as the bath's forcing acceleration is increased progressively, including steady rotational motion, periodic radial or azimuthal oscillations, azimuthal traveling waves and rearrangement into regular polygonal structures [26] (Figure 3.1(a)–(d)). This body of literature shows that lattices of bouncing droplets exhibit behavior reminiscent of crystal vibrations, which can be profitably clarified and extended by analyzing different ordered arrangements of bouncers.

We present here a theoretical investigation of free 1D chains of bouncing droplets, as depicted in Figure 3.2(a). Particular attention will be paid to driven

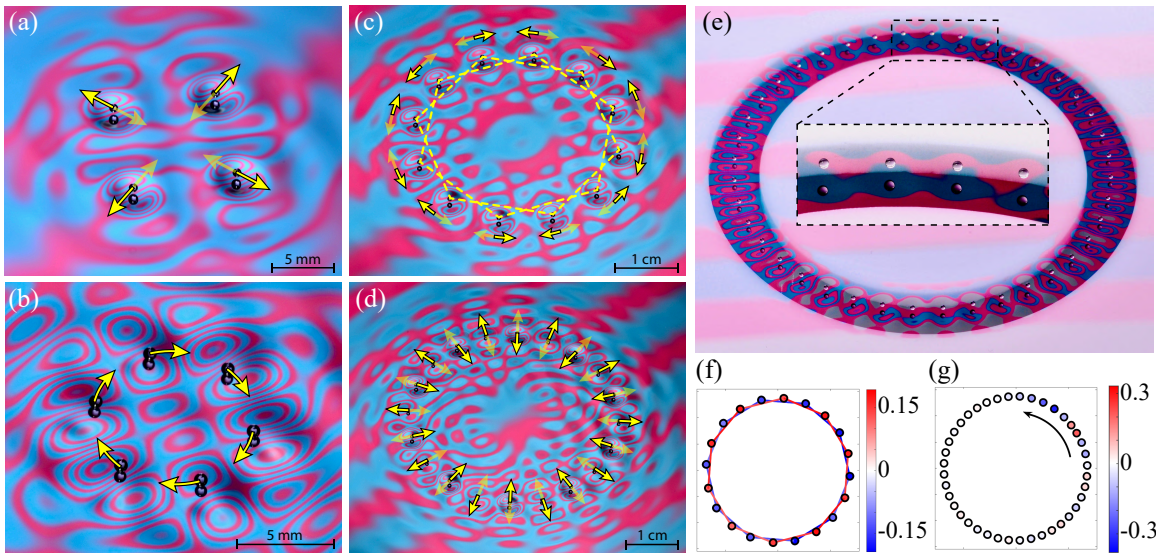

Figure 3.1 Free and confined rings of droplets bouncing on a fluid interface. Prior work [26] revealed that free rings can exhibit (a) in-phase radial instabilities, (b) orbital motion, (c) out-of-phase azimuthal oscillations and (d) out-of-phase radial oscillations. (e) Prior work [112] has shown that a collection of droplets confined to an annulus destabilize via either optical oscillations (panel (f)) or a propagating solitary wave (panel (g)). In panels (f) and (g), colors denote the droplets' instantaneous angular velocity in radians per second. Panels (a)–(d) are taken from Couchman *et al.* [26], and panels (e)–(g) are taken from Thompson *et al.* [112]. Compiled figure is found in Bush *et al.* [23].

droplet chains, in which the drop at one end of the chain is subjected to a time-periodic forcing in the horizontal direction (Figure 3.2(b)). We note that periodically-driven classical systems, both deterministic [63, 64] and stochastic [51], have a long history of study, and there has been recent interest in driven many-body quantum systems [54, 20]. However, relatively little is known about driven classical systems with temporally nonlocal interactions [113], as arise in droplet chains due to their path memory. While forced bouncing droplet collectives have not yet been studied experimentally, Perrard [85] applied periodic forcing to a single walker by encapsulating a drop of ferrofluid within an oil droplet, and then applying a vertical magnetic field with a radial gradient. By modulating the magnetic field strength, the dynamics of a walker in an oscillatory central force $F = -(k_0 + k_1 \sin \omega t)x$ could be probed. Periodic forcing of such droplets was also achieved by oscillating a magnet nearby (Supplementary Figure 3 in [88]).

Here we consider a system very similar to that in Chapter 2: a fluid bath with vertical acceleration $\gamma \sin(2\pi f_0 t)$, surface tension σ, density ρ, kinematic viscosity ν and depth H, and drops of mass m and radius R. Once again we denote γ_F as the Faraday instability threshold, and consider the drops to be in the (2,1) bouncing mode [53] described in Section 2.2.

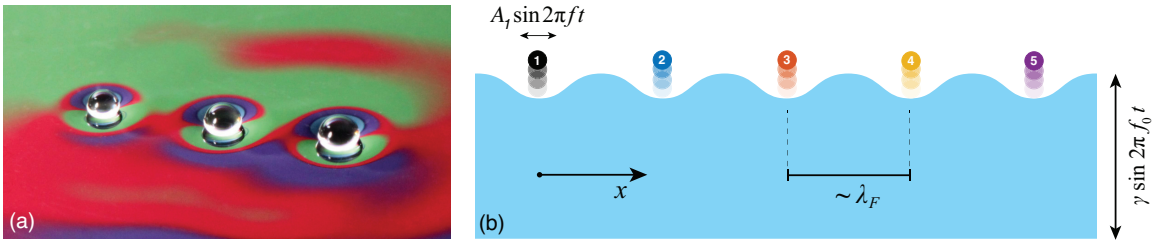

Figure 3.2 (a) A chain of three droplets bouncing on a vertically vibrating fluid bath. Photo credit: Daniel M. Harris. (b) Schematic of a periodically-forced chain of five droplets, as considered in Section 3.3. The first drop is forced sinusoidally in the horizontal direction with amplitude A_1 and frequency f, and the bath is vibrated vertically with peak acceleration γ and frequency f_0. The Faraday wavelength is denoted λ_F. Drops 1, 2, 3, 4 and 5 are indicated in black, blue, red, yellow, and purple, respectively, a color scheme that is repeated throughout the chapter.

In this chapter, we consider not a single droplet, but a chain of N droplets, and assume the droplet to move in the x- and z-directions only; thus, the stroboscopic model employed here accounts only for motion in the x-direction, as the vertical bouncing is not modeled.

The non-dimensional trajectory equation for the ith droplet in an N-droplet chain is thus given by:

$$\kappa\ddot{x}_i + \dot{x}_i = \beta \sum_{j=1}^{N} \int_{-\infty}^{t} J_1(x_i(t) - x_j(s)) e^{-(t-s)} ds, \quad i = 1, 2, ..., N \tag{3.1}$$

where, as in Chapter 2, $\kappa = m/DT_M$ and $\beta = mgAk_F{}^2T_M{}^2/DT_F$ are the dimensionless mass and wave force coefficient, respectively; again, recall that $T_M = \frac{T_d}{1-\gamma/\gamma_F}$ is the memory time, *i.e.,* the memory increases as γ increases toward γ_F.

Since this chapter is concerned with chains of bouncers, we restrict our attention to the parameter regime $0.65 < \gamma/\gamma_F < 0.78$. According to the regime diagrams presented by Moláček & Bush [78] and Wind-Willassen *et al.* [119], the lower bound corresponds to the onset of the $(2, 1)$ bouncing mode for drops with vibration number $2\pi f_0/\sqrt{\sigma/\rho R^3} \approx 0.86$. The upper bound corresponds to the walking threshold $\beta = 2$ for a single drop [82], specifically, the critical vibrational acceleration above which the bouncing state destabilizes into a steadily translating walking state.

3.2 Equilibrium Solutions and Linear Stability

We first consider an equilibrium state of bouncers located at the fixed positions $x_i(t) = \chi_i$, where $\chi_i < \chi_j$ for $i < j$. Substituting this into Equation (3.1), we find that the positions χ_i satisfy the system of equations $\sum_{j=1}^{N} \mathrm{J}_1(\chi_i - \chi_j) = 0$ for $i = 1, \ldots, N$. These conditions imply that the horizontal component of the wave force on each drop vanishes. An equivalent system is given by

$$-\sum_{j=1}^{i-1} \mathrm{J}_1 \left(\sum_{k=j}^{i-1} d_k \right) + \sum_{j=i}^{N-1} \mathrm{J}_1 \left(\sum_{k=i}^{j} d_k \right) = 0, \quad i = 1, \ldots, N-1. \tag{3.2}$$

where $d_i = \chi_{i+1} - \chi_i$ for $i = 1, \ldots, N-1$. Note that these equations may be summed to obtain the corresponding equation for $i = N$.

For the rest of this chapter, we will focus on chains of $N = 5$ droplets, for *symmetric* equilibrium solutions, *i.e.,* $d_1 = d_4$ and $d_2 = d_3$. We make these choices for simplicity: in this case, the system (3.2) becomes a system of just 2 equations in 2 unknowns d_1 and d_2, whose solutions correspond to the intersections of the zero-level curves of F_1 and F_2 defined below and shown in Figure 3.3 and thus can readily be solved for numerically:

$$\begin{aligned} F_1(d_1, d_2) &\equiv \mathrm{J}_1(d_1) + \mathrm{J}_1(d_1 + d_2) + \mathrm{J}_1(d_1 + 2d_2) + \mathrm{J}_1(2d_1 + 2d_2) = 0, \\ F_2(d_1, d_2) &\equiv -\mathrm{J}_1(d_1) + \mathrm{J}_1(d_2) + \mathrm{J}_1(2d_2) + \mathrm{J}_1(d_1 + 2d_2) = 0. \end{aligned} \tag{3.3}$$

We will discuss these equilibrium solutions in more detail after a more general discussion of the stability of any general equilibrium solution.

To assess the stability of any equilibrium bouncing state, we first linearize the system of governing equations around the equilibrium solution by substituting $x_i(t) = \chi_i + \epsilon\tilde{x}_i(t)$ into Equation (3.1) and retaining terms at leading order in ϵ. Dropping the tildes in what follows, we obtain the linear system

$$\kappa\ddot{x}_i + \dot{x}_i = \beta \sum_{j=1}^{N} \mathrm{J}_1'(\chi_i - \chi_j) \int_{-\infty}^{t} (x_i(t) - x_j(s))\mathrm{e}^{-(t-s)}\,\mathrm{ds}. \tag{3.4}$$

This may be recast as a system of ordinary differential equations by introducing the variables $X_i(t) = \int_{-\infty}^{t} x_i(s)\mathrm{e}^{-(t-s)}\,\mathrm{ds}$:

$$\kappa\ddot{x}_i + \dot{x}_i = \beta \sum_{j=1}^{N} \mathrm{J}_1'(\chi_i - \chi_j)(x_i - X_j), \quad \dot{X}_i = -X_i + x_i. \tag{3.5}$$

We may write Equation (3.5) as a system of first-order ordinary differential equations, $\dot{z} = Qz$, where

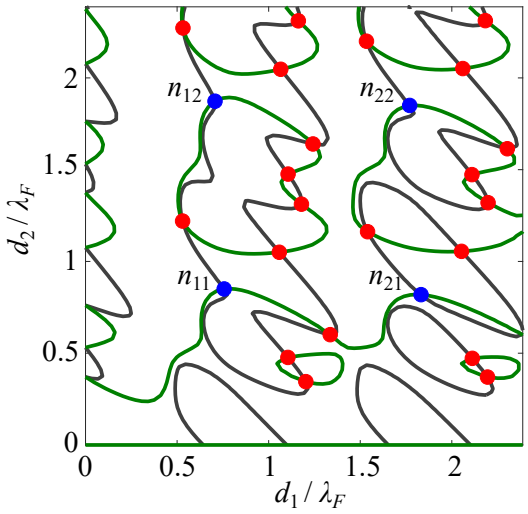

Figure 3.3 The gray and green curves denote the zero-contours of the the functions $F_1(d_1, d_2)$ and $F_2(d_1, d_2)$, respectively, defined in the system (3.3). Here, d_1 is the distance between the first and second drop, which equals that between the fourth and fifth drop; d_2 is the distance between the second and third drop, which equals that between the third and fourth drop. The intersections of the contours correspond to bouncing states, which are color-coded on the basis of the linear stability analysis presented in Section 3.2. Specifically, blue (red) dots denote stable (unstable) solutions at the lowest memory considered, $\gamma/\gamma_F = 0.66$. The stable states are labeled n_{11}, n_{12}, n_{21} and n_{22}. The Faraday wavelength is denoted by λ_F.

$z = (x_1, \ldots, x_N, X_1, \ldots, X_N, \dot{x}_1, \ldots, \dot{x}_N)$. The matrix Q has the block form

$$Q = \begin{pmatrix} Z & Z & I \\ I & -I & Z \\ \frac{\beta}{\kappa} S & -\frac{\beta}{\kappa} P & -\frac{1}{\kappa} I, \end{pmatrix}, \quad \text{where} \quad P_{ij} = \mathrm{J}_1'(\chi_i - \chi_j), \quad S_{ij} = \delta_{ij} \sum_{k=1}^{N} \mathrm{J}_1'(\chi_i - \chi_k), \tag{3.6}$$

Z is the $N \times N$ zero-matrix, I the $N \times N$ identity matrix and δ_{ij} the Kronecker delta. The stability of the bouncing state defined by Equation (3.2) is determined by the eigenvalue s^* of Q with the largest real part. Specifically, the state is stable if $\mathrm{Re}(s^*) < 0$, and unstable otherwise. Note that one eigenvalue of Q is identically zero and is thus neglected from consideration; indeed, the corresponding eigenvector $(\vec{1}, \vec{1}, \vec{0})$ reflects the translation invariance of the trajectory equation (3.1), $\vec{1}$ and $\vec{0}$ being vectors in R^N of ones and zeros, respectively.

Assessing the stability for several of the smallest equilibrium solutions (*i.e.,* for small d_1 and d_2) at the lowest bath forcing acceleration considered, γ/γ_F, we found both stable and unstable equilibrium solutions. The stable equilibria may be labeled as n_{ij} , where the indices i and j denote increasing values of the inter-drop distances d_1 and d_2, respectively. For the rest of this dissertation, most of our focus will be on the four smallest stable solutions, n_{11}, n_{12}, n_{21}, and n_{22}.

Our linear stability analysis on these four equilibria shows that the real part of the least stable eigenvalue s^* increases with the forcing acceleration γ, and the imaginary part is nonzero, indicating that each of these states goes unstable to an oscillatory instability as γ is increased progressively. The instability threshold is the lowest for the state n_{11}; this result may be understood on the basis of the fact that the oscillation amplitude of the wave kernel $\mathrm{J}_0(k_F x)$ decreases with x, indicating that the force between droplets generally weakens as the distance between them increases.

The eigenvector $\mathbf{z}^*$ corresponding to the unstable mode at the onset of instability ($\mathrm{Re}(s^*) = 0$) is depicted by the arrows in Figure 3.4. We note that each of the bouncing states exhibits a qualitatively similar unstable mode, with the drops in the interior oscillating roughly out-of-phase with respect to the ones at the edges. The second and fourth drops exhibit weaker oscillations than the others, and remain roughly stationary for the n_{21}–bouncing state. With the exception of the n_{12}–state, the drop in the middle exhibits the strongest oscillations, with oscillation amplitudes nearly twice that of the drops on the edges for the n_{21}–state. This result is qualitatively consistent with the observation of Eddi *et al.* [36], who conducted experiments on quasi-1D aggregates of bouncers consisting of more than ten drops along one direction and three drops in the transverse direction. They observed that the aggregates effectively "melt" from the center as the bath's vibrational acceleration is increased progressively, in contrast to classical melting processes that occur along the edges of a material.

The oscillation frequency of the droplet chain is obtained by numerically computing the eigenvalues of the matrix Q in Equation (3.6). An estimate for these frequencies may be obtained by considering the simplified case of two drops interacting in the low-memory regime, for which we may approximate $X_i \approx x_i$ in the system (3.5). The linearized equation (3.5) then assumes the form of a spring-mass system with dimensionless mass κ and spring constant $-\beta \mathrm{J}_1'(d)$, d being the equilibrium distance between the drops that satisfies $\mathrm{J}_1(d) = 0$. The dimensional form of the effective frequency of oscillation is thus

$$f = \frac{1}{2\pi}\sqrt{\frac{Ak_F^2|\mathrm{J}_1'(k_F d)|gT_M}{T_F}}. \tag{3.7}$$

Using the value of T_M for $\gamma/\gamma_F = 0.74$, which corresponds to the onset of instability for the n_{11}–state (Figure 3.5(a)), and the separation distance $d/\lambda_F = 0.61$, which corresponds to the first nonzero solution of $\mathrm{J}_1(k_F d) = 0$, we obtain

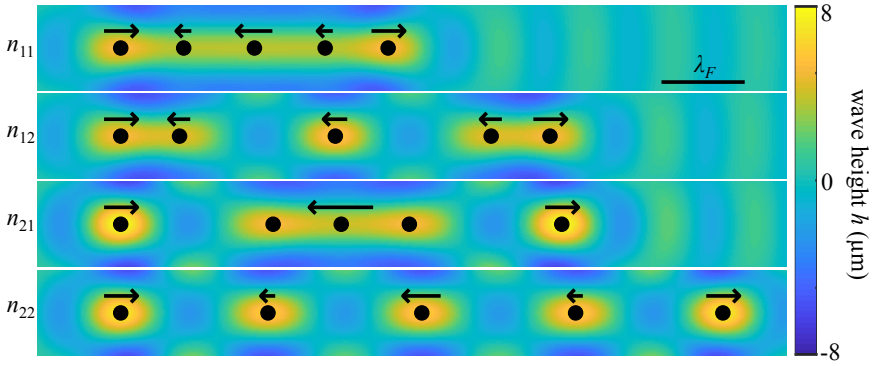

Figure 3.4 Schematic of the four symmetric bouncing states n_{11}, n_{12}, n_{21} and n_{22} described in Section 3.2. The colormap indicates the corresponding wave field $h(x) = (AT_M/T_F)\sum_{i=1}^{N} \mathrm{J}_0(k_F|x-(\chi_i,0)|)$ at the onset of the chain's oscillatory instability. Black dots indicate the drop positions χ_i, as determined by solving the system (3.3). The eigenvector z^* corresponding to the unstable mode is depicted by the arrows; the size of the arrow indicates the magnitude of each component of z^*, and the direction the approximate phase. The components of z^* for drops 2 and 4 in the n_{21}–state are small and thus not depicted. The scale bar shows the Faraday wavelength λ_F.

the frequency $f = 1.3$ Hz from Equation (3.7). This result agrees well with the experimental results of Eddi *et al.* [36], who measured oscillation frequencies of $f = 1$ Hz for quasi-1D and 2D hexagonal lattices, and $f = 1.3$ Hz for 2D square lattices.

3.3 Forced Droplet Chains

We now investigate the response of a droplet chain to a time-periodic forcing applied to the drop at one end, as depicted in Figure 3.2(b). Specifically, we assume that the horizontal motion of the first drop is prescribed, $x_1(t) = A_1 \sin(2\pi f t)$, where the oscillation amplitude A_1 and frequency f are given. As in Section 3.2, we restrict our attention to the four equilibrium states n_{11}, n_{12}, n_{21} and n_{22} depicted in Figure 3.4, and pay particular attention to the state n_{11} for which the drops are closest to each other, $d_1 \approx d_2 \approx 0.8\lambda_F$. We consider the parameter regime $0.66 \leq \gamma/\gamma_F \leq 0.74$, the lower bound corresponding to the onset of the (2,1) resonant bouncing mode (see Section 3.1), and the upper bound being just above the onset of the oscillatory instability for the n_{11}–bouncing state (Figure 3.5(a)). We also assume the forcing

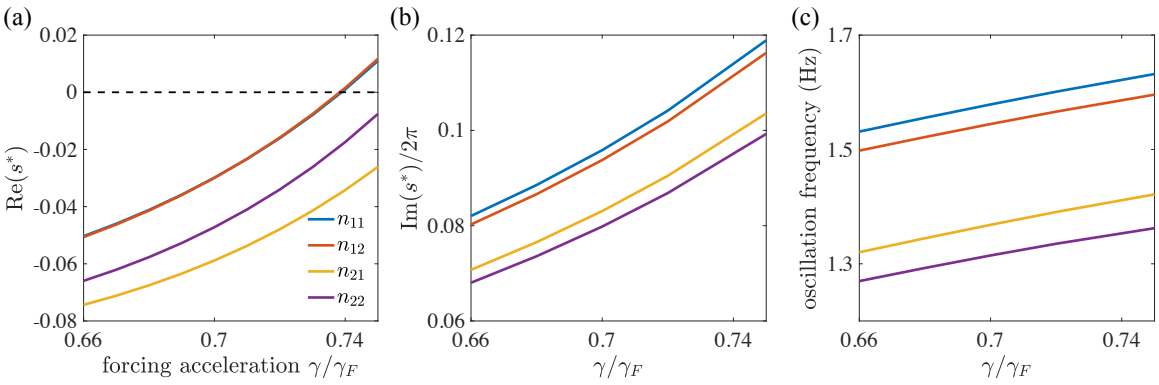

Figure 3.5 Stability analysis of symmetric bouncing states of a five-droplet chain, performed using the procedure described in Section 3.3. Specifically, s^* denotes the nontrivial eigenvalue of the matrix Q with the largest real part, where Q is defined in Equation (3.6). Colors denote the different bouncing states n_{11}, n_{12}, n_{21} and n_{22}, as shown in the legend of panel (a). The dimensionless forcing acceleration of the bath is denoted γ/γ_F. (a) Real part of s^*, which determines the stability of the bouncing state, $\mathrm{Re}(s^*) < 0$ ($\mathrm{Re}(s^*) > 0$) corresponding to stable (unstable) states. (b) Imaginary part of s^*. (c) The dimensional oscillation frequency $\mathrm{Im}(s^*)/(2\pi T_M)$ of the chain, T_M being the memory time defined in the equations (2.3).

frequency to be much less than the bouncing frequency $f_0/2 = 40$ Hz, $f \ll f_0/2$, a regime in which we expect the bouncing dynamics to remain periodic and thus the stroboscopic model, Equation (3.1), to remain valid. Specifically, we restrict our attention to the regime $fT_M \leq 0.3$, which corresponds to forcing frequencies less than 6 Hz for $\gamma/\gamma_F \geq 0.66$.

3.3.1 Linear theory

We begin by assessing the linear response of a droplet chain when Drop 1 (on the left end of the chain) is forced periodically with small oscillation amplitude, $A_1 \ll \lambda_F$ and some frequency f. To that end, letting $\omega = 2\pi f$, we substitute $x_i(t) = A_i e^{i\omega t}$ and $X_i(t) = A_i e^{i\omega t}/(1 + i\omega)$ into the linear equation (3.5), which describes the small-amplitude oscillations of a chain of bouncers around their equilibrium positions. We thus obtain a linear system of equations for the complex amplitudes A_i, which may be written in the matrix form $M\mathbf{a} = \mathbf{v}$, where $\mathbf{a} = (A_2, \ldots, A_N)/A_1$. Here, M is

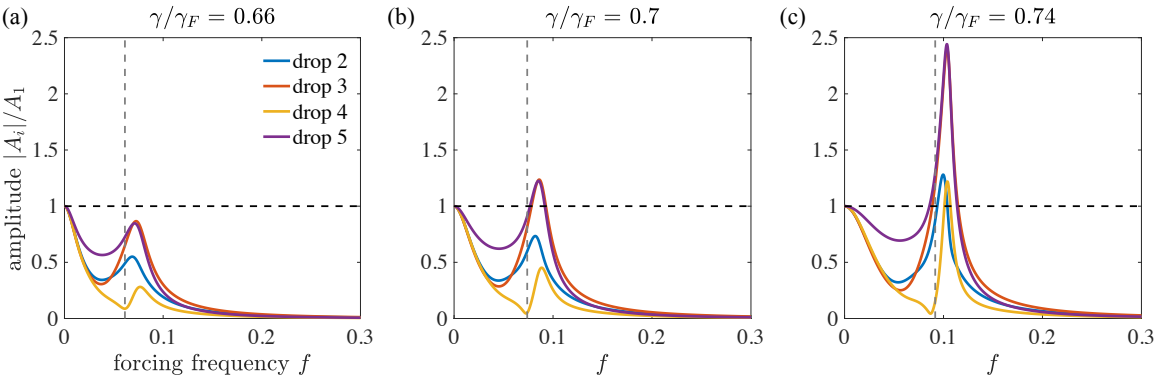

Figure 3.6 Dependence of the oscillation amplitude $|A_i|$ on the dimensionless forcing frequency f for a chain of five drops initialized in the n_{11}–bouncing state, as predicted by the linear theory described in Section 3.3.1 (Equation (3.8)). The amplitudes are normalized by the forcing amplitude A_1 applied to the first drop. The colors correspond to the different drops in the chain, as indicated by the legend in panel (a). Three values of the bath's forcing acceleration are shown: (a) $\gamma/\gamma_F = 0.66$, (b) $\gamma/\gamma_F = 0.7$ and (c) $\gamma/\gamma_F = 0.74$. The dashed gray lines denote the resonant frequency of an unforced droplet chain, as approximated by Equation (3.7).

a $(N-1)\times(N-1)$ matrix and $\mathbf{v}$ a vector in C^{N-1} with entries

$$M_{ij} = \begin{cases} -\kappa\omega^2 + \mathrm{i}\omega - \beta\left(\sum_{k\neq i}^{N-1} \mathrm{J}_1'(\chi_{i+1}-\chi_{k+1}) + \mathrm{J}_1'(\chi_{i+1}) + \frac{\mathrm{i}\omega}{1+\mathrm{i}\omega}\mathrm{J}_1'(0)\right) & \text{if } i = j \\ \frac{\beta}{1+\mathrm{i}\omega}\mathrm{J}_1'(\chi_{i+1}-\chi_{j+1}) & \text{if } i \neq j \end{cases},$$

$$v_i = -\frac{\beta}{1+\mathrm{i}\omega}\mathrm{J}_1'(\chi_{i+1}). \tag{3.8}$$

Figure 3.6 shows the dependence of the amplitudes $|A_i|/A_1$ on the forcing frequency f for a chain of five drops initialized in the n_{11}–bouncing state. The corresponding results for the other bouncing states n_{12}, n_{21} and n_{22} are shown in Figure 3.7. The qualitative features of the curves in Figures 3.6 and 3.7 may be interpreted on the basis of the oscillatory modes depicted in Figure 3.4. Specifically, for the n_{11} and n_{22} states, drops 3 and 5 exhibit substantially larger oscillation amplitudes than drops 2 and 4. This is not so for the other bouncing states; specifically, all of the drops exhibit comparable oscillation amplitudes for the n_{12}–state, and drops 2 and 4 have rather low amplitudes for the n_{21}–state (Figure 3.7).

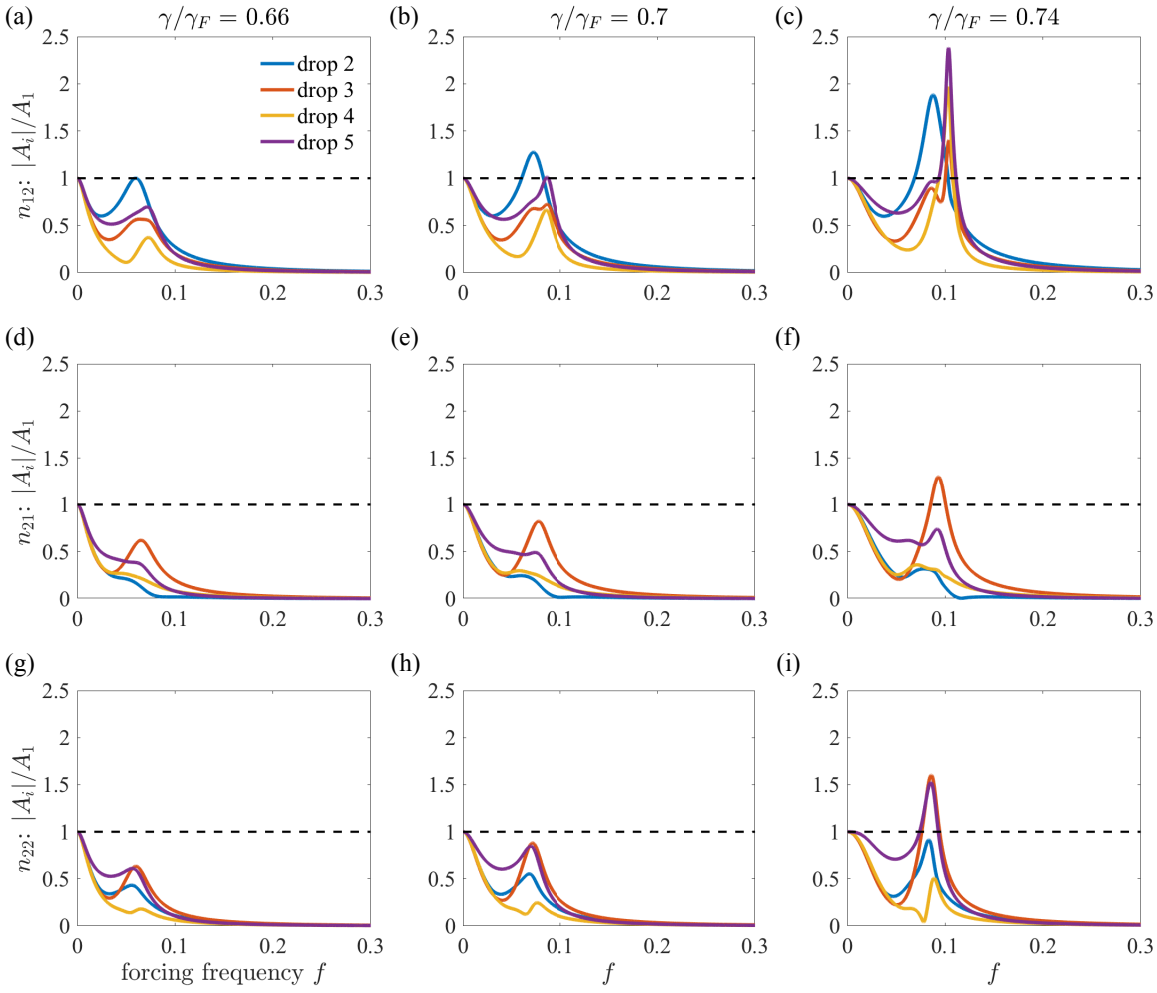

Figure 3.7 The figures show the dependence of the oscillation amplitude $|A_i|$ on the dimensionless forcing frequency f for a periodically-forced chain of five drops, as computed using the linear theory presented in Subsection 3.3.1. The procedure described in the caption of Figure 3.6 is repeated for droplet chains initialized in the n_{12} (Panels (a)–(c)), n_{21} (panels (d)–(f)), and n_{22} (panels (g)–(i)) bouncing states. Three values of the bath's forcing acceleration are shown: $\gamma/\gamma_F = 0.66$ (left panels), $\gamma/\gamma_F = 0.7$ (middle panels) and $\gamma/\gamma_F = 0.74$ (right panels).

Note that $|A_i|/A_1 \to 1$ in the limit $f \to 0$, which is evident from inspection of the system (3.8). Moreover, $|A_i|/A_1 \to 0$ in the high-frequency limit $f \to \infty$, a regime that will be treated in Subsection 3.3.3. For intermediate values of the forcing frequency, the oscillation amplitudes are maximized for a critical value of the forcing frequency. This resonant frequency is approximated well by the characteristic frequency of a droplet pair in the low-memory limit, as given by Equation (3.7) and depicted by the dashed lines in Figure 3.6. Moreover, the maximum amplitude increases with memory and may even exceed the imposed amplitude A_1, as can be seen in Figure 3.6(b) and 3.6(c). This result suggests that relatively large-amplitude oscillations may be excited for forcing frequencies near the droplet chain's intrinsic resonant frequency, particularly as the waves become more persistent. While the theory presented in this subsection is strictly valid for small-amplitude oscillations, such resonant oscillations will be revisited using numerical simulations of droplet chains, the results of which are presented in the following subsection.

3.3.2 Nonlinear oscillations of forced droplet chains

While the linear equation (3.8) is straightforward to solve, numerical simulations of the trajectory equation (3.1) are required to assess the nonlinear response of a droplet chain to finite-amplitude oscillations. To that end, we adapt the numerical method described by Oza *et al.* [84] to solve the system (3.1), which consists of using a fourth-order Adams-Bashforth method for time-stepping combined with Simpson's rule for computing the integrals. The histories of each of the drops must also be specified, which we take to correspond to an equilibrium bouncing state, specifically, $x_i(t) = \chi_i$ for $t < 0$, where the constants χ_i are determined by solving the system (3.3). The trajectories are evolved up to a final time $t_{\max} \geq \max(50T, 600)$, and the dimensionless time step is taken to be $\Delta t = \min(2^{-4},\ T/40)$, where $T = 1/f$ is the forcing period.

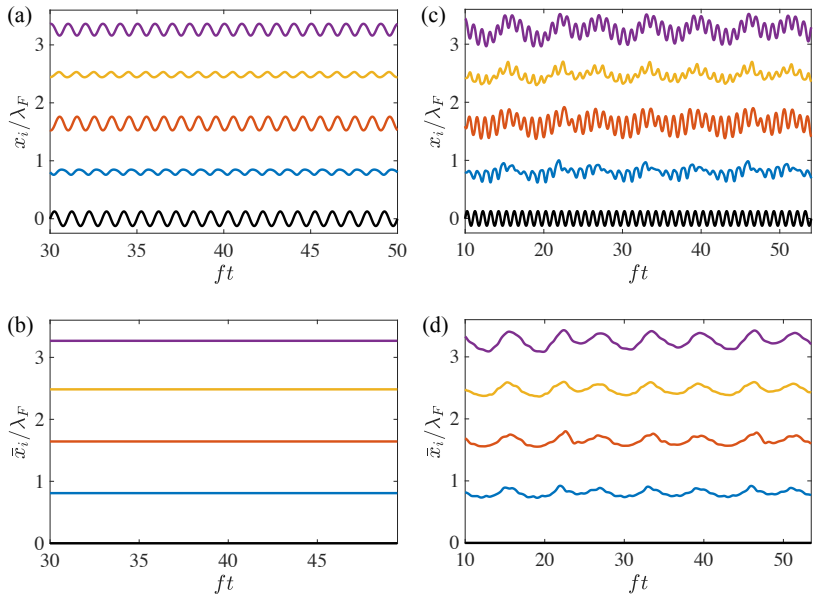

Figure 3.8 Numerical solutions of the trajectory equation (3.1) for a chain of $N = 5$ drops initialized in the n_{11}–bouncing state. The first drop (black curve) is subjected to a periodic forcing of amplitude $A_1 = \lambda_F/8$. Panels (a) and (c) show the drop trajectories $x_i(t)$, the time ft given in units of the forcing period $T = 1/f$. Panels (b) and (d) show the cycle-averaged drop position $\bar{x}_i(t)$, as defined in Equation (3.9). Simple periodic oscillations are evident in Panels (a) and (b), corresponding to $f = 0.08$ and bath vibrational acceleration $\gamma/\gamma_F = 0.7$. Aperiodic oscillations are shown in panels (c) and (d), corresponding to $f = 0.09$ and $\gamma/\gamma_F = 0.74$. The frequencies f correspond to those for which the third and fifth drops exhibit the largest oscillations, as shown in Figure 3.9(b) and 3.9(c).

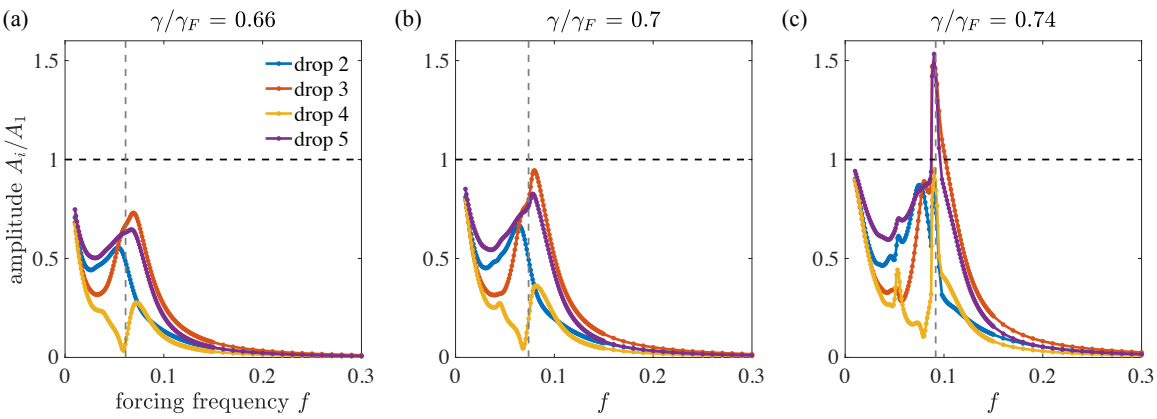

Figure 3.9 Dependence of the oscillation amplitude A_i on the dimensionless forcing frequency f for a chain of five drops initialized in the n_{11}–bouncing state, as obtained from numerical simulations of the trajectory equation (3.1). The amplitudes are normalized by the forcing amplitude $A_1 = \lambda_F/8$ applied to the first drop. The colors correspond to the different drops in the chain, as indicated by the legend in Panel (a). Three values of the bath's forcing acceleration are shown: (a) $\gamma/\gamma_F = 0.66$, (b) $\gamma/\gamma_F = 0.7$ and (c) $\gamma/\gamma_F = 0.74$. The dashed gray lines denote the resonant frequency of an unforced droplet chain, as approximated by Equation (3.7).

Simulated trajectories for a droplet chain initialized in the n_{11}–bouncing state are shown in Figure 3.8. At relatively low memory, the drops exhibit simple oscillations (Figure 3.8(a)), and the drop at the end of the chain (purple) oscillates roughly in-phase with the forced drop (black) and out-of-phase with the drops in the interior; this is consistent with the predictions of the linear stability analysis of unforced chains presented in Figure 3.4. At higher memory, the drops often exhibit complex aperiodic oscillations (shown in Figure 3.8(c)), whose envelope can be characterized by defining the cycle-averaged drop position

$$\bar{x}_i(t) = \frac{1}{T}\int_{t-T/2}^{t+T/2} x_i(s)\,\mathrm{ds}. \tag{3.9}$$

This quantity is constant for the simple oscillatory motion occurring at low memory (Figure 3.8(b)), but exhibits oscillations on a timescale long relative to the forcing period T for the complex motion arising at higher memory (Figure 3.8(d)).

To quantify the dependence of the oscillation amplitude A_i of each drop on the forcing frequency f, we define

$$A_i = \left[\frac{2}{t_0}\int_{t_{\max}-t_0}^{t_{\max}} \left(x_i(t) - \langle x_i \rangle\right)^2 \, \mathrm{dt}\right]^{1/2}, \quad \text{where} \quad \langle x_i \rangle = \frac{1}{t_0}\int_{t_{\max}-t_0}^{t_{\max}} x_i(t) \, \mathrm{dt} \quad (3.10)$$

and $t_0 \leq 5T$.

Figure 3.9 shows the oscillation amplitudes A_i/A_1 of a droplet chain in the n_{11}–bouncing state, with the first drop subjected to a forcing amplitude $A_1 = \lambda_F/8$. We note that the predictions of the linear theory (Figure 3.6) are qualitatively consistent with the simulations; specifically, the oscillation amplitude of each drop is maximized for a critical value of the forcing frequency f, which is approximated well by Equation (3.7) (gray dashed line). Moreover, the maximum oscillation amplitude increases with memory. At the highest memory considered, $\gamma/\gamma_F = 0.74$, the amplitudes of drops 3 and 5 exceed that of the first drop, indicating that a vibrating chain of droplets can effectively draw energy from the surface waves and thus execute oscillations whose amplitude exceeds that which is imposed. We note that the maximum amplitudes in simulations (Figure 3.9) are smaller than those predicted by the linear theory (Figure 3.6), indicating that nonlinear effects serve to effectively damp the forced oscillations. Similar conclusions may be drawn for droplet chains forced in the n_{12}, n_{21} and n_{22}–bouncing states, the results for which are shown in Figure 3.11(a)–(c), 3.11(d)–(f) and 3.11(g)–(i), respectively.

Figure 3.10 shows the results for a droplet chain initialized in the n_{11}–bouncing state and forced with a larger amplitude, $A_1 = \lambda_F/4$. The behavior is qualitatively different from that predicted by the linear theory (Figure 3.6); specifically, the second drop (blue) rather than the third (red) exhibits the largest oscillations for a critical forcing frequency f, which in turn is overestimated by the approximate formula given in Equation (3.7) (gray dashed line). Moreover, the oscillation amplitudes may exhibit maxima at multiple values of the forcing frequency f even at low memory

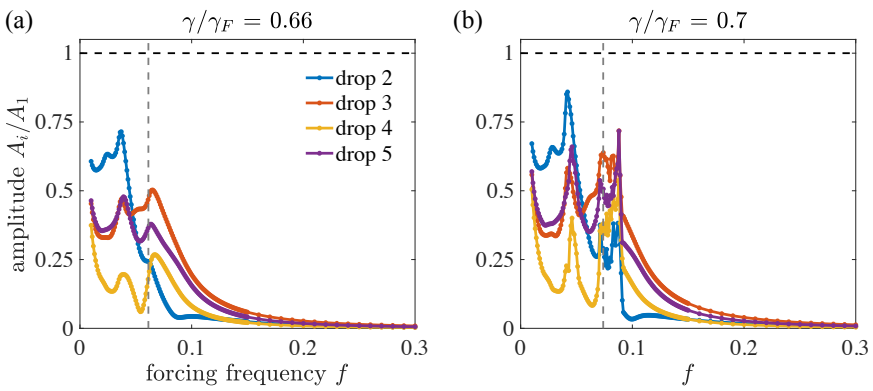

Figure 3.10 The procedure described in the caption of Figure 3.9 is repeated for a larger value of the forcing amplitude, $A_1 = \lambda_F/4$.

(Figure 3.10(a)), an effect absent at the lower forcing amplitude (Figure 3.9(a)). The results for higher memory are not shown because the simulated trajectories exhibit intersections in this parameter regime for certain values of the forcing frequency f. These unphysical solutions are an artifact of the stroboscopic model's poor characterization of the waves in the near field. Indeed, the model given by the system (2.2) was derived under the assumption that the drops are point sources of waves [78], an approximation that is known to be inadequate when the distance between the drops is comparable to their diameter [83].

For relatively large memory and forcing amplitude A_1, the droplets execute aperiodic and presumably chaotic trajectories, as shown in Figure 3.12(a). To understand the qualitative features of this complex dynamics, we plot in Figure 3.12(b) the cycle-averaged distances between neighboring drops, $\bar{d}_i(t) = \bar{x}_{i+1}(t) - \bar{x}_i(t)$, where $\bar{x}_i(t)$ is defined in Equation (3.9). The dashed lines indicate the mean inter-drop distances $(d_1 + d_2)/2$ of the symmetric unforced bouncing states n_{11}, n_{22} and n_{33}, as predicted by the system (3.3). We observe that $\bar{d}_i(t)$ exhibits oscillations around the dashed lines, punctuated by intermittent transitions between them. Unlike the solutions observed for lower forcing amplitude A_1 (Figure 3.8), the droplet chain

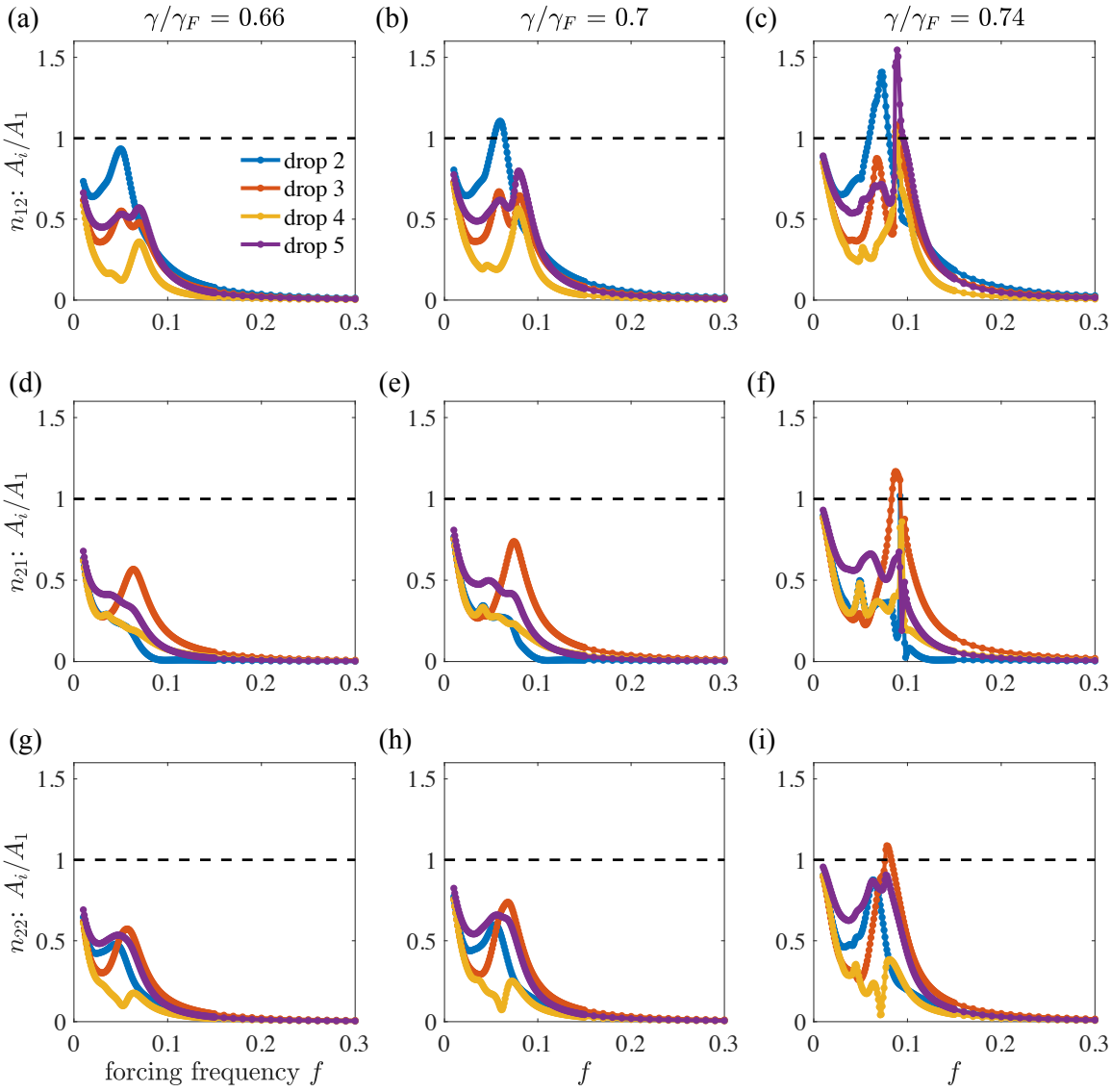

Figure 3.11 The figures show the dependence of the oscillation amplitude A_i on the dimensionless forcing frequency f for a periodically-forced chain of five drops. The amplitudes are computed using numerical simulations of the trajectory equation (2.4). Specifically, the procedure described in the caption of Figure 3.9 is repeated for droplet chains initialized in the n_{12} (Panels (a)–(c)), n_{21} (panels (d)–(f)), and n_{22} (panels (g)–(i)) bouncing states. Three values of the bath's forcing acceleration are shown: $\gamma/\gamma_F = 0.66$ (left panels), $\gamma/\gamma_F = 0.7$ (middle panels) and $\gamma/\gamma_F = 0.74$ (right panels).

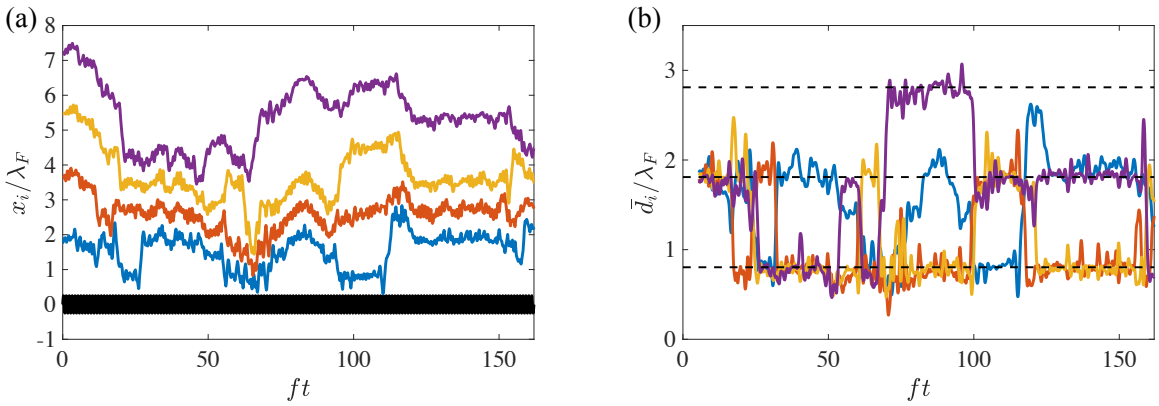

Figure 3.12 Complex aperiodic oscillations observed in simulating a chain of $N = 5$ drops initialized in the n_{22}–bouncing state on a bath with vibrational forcing acceleration $\gamma/\gamma_F = 0.74$. The first drop (black) is subjected to a periodic forcing of amplitude $A_1 = \lambda_F/4$ and dimensionless frequency $f = 0.09$. (a) Trajectories $x_i(t)$ of each drop, plotted as a function of the dimensionless time ft. (b) Cycle-averaged inter-drop distances $\bar{d}_i(t) = \bar{x}_{i+1}(t) - \bar{x}_i(t)$ for $i = 1$ (blue), 2 (red), 3 (yellow) and 4 (purple). The dashed lines indicate the mean inter-drop distances $(d_1 + d_2)/2$ of the symmetric unforced bouncing states n_{11}, n_{22} and n_{33}, as given by the system (3.3).

chaotically jumps between different equilibrium solutions without settling near any of them.

3.3.3 High-frequency limit $f \to \infty$

As shown in Figures 3.6, 3.9 and 3.10, the drops' oscillation amplitudes go to zero in the limit of large forcing frequency, $A_i \to 0$ as $f \to \infty$. In this limit, we find that the chain effectively settles into a new bouncing state that is dynamically stabilized by the periodic forcing applied to the first drop. To rationalize this observation, we substitute into Equation (3.1) the expressions $x_1(t) = A_1 \sin \omega t$ and $x_i(t) = \chi_i$ for $i = 2, \ldots, N$, where $\omega = 2\pi f$, and obtain

$$\frac{1}{\omega}\int_0^\infty \mathrm{J}_1(\chi_i - A_1 \sin(\tau - \sigma))\mathrm{e}^{-\sigma/\omega}\,\mathrm{d}\sigma + \sum_{\mathrm{j}=2}^{\mathrm{N}} \mathrm{J}_1(\chi_\mathrm{i} - \chi_\mathrm{j}) = 0, \tag{3.11}$$

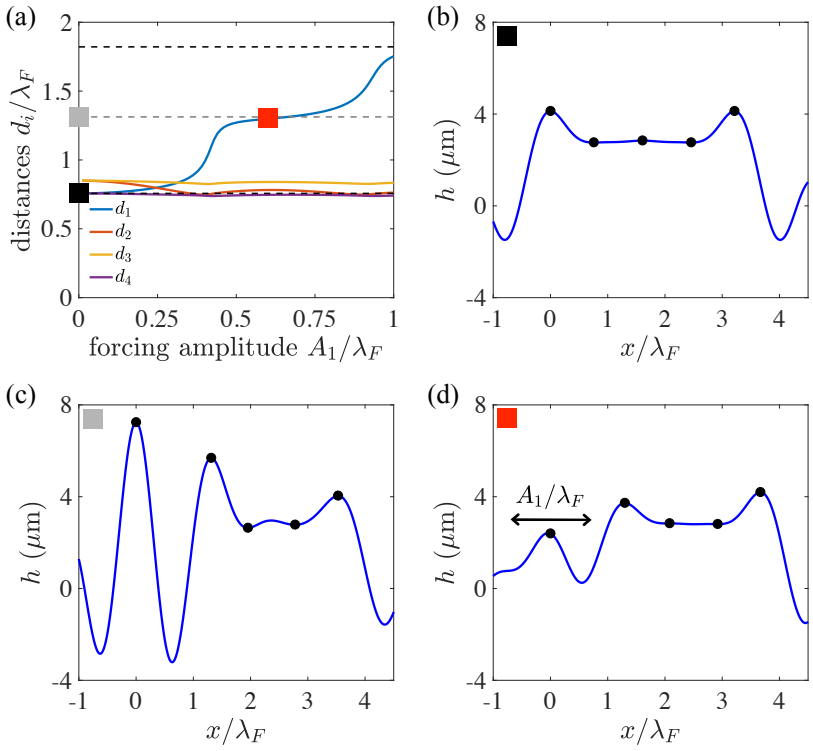

Figure 3.13 Bouncing states of a chain of five drops forced in the limit of high frequency, $f \to \infty$. (a) The dependence of the inter-drop distances $d_i = x_{i+1} - x_i$ on the forcing amplitude A_1, as obtained by solving Equation (3.12). The dashed lines denote the values of d_1 for an unforced droplet chain, black (gray) lines corresponding to stable (unstable) solutions for $\gamma/\gamma_F = 0.66$. Panels (b)–(d) show the wave profiles $h(x)$ in microns, as given by Equation (3.13) (blue curves), and drop positions (black dots), corresponding to three configurations: (b) an unforced stable chain in the n_{11}–bouncing state (black square), (c) an unforced unstable chain (gray square), and (d) a chain forced with amplitude $A_1/\lambda_F = 0.6$ (red square).

where $\tau = \omega t$. Since the integral in Equation (3.11) is a 2π–periodic function of τ, it can be simplified in the limit $\omega \to \infty$ using the geometric series formula, to get:

$$\frac{1}{2\pi}\int_0^{2\pi} \mathrm{J}_1(\chi_i - A_1 \sin\sigma)\,\mathrm{d}\sigma + \sum_{\mathrm{j}=2}^{\mathrm{N}} \mathrm{J}_1(\chi_\mathrm{i} - \chi_\mathrm{j}) = 0, \quad \mathrm{i} = 2, \ldots, \mathrm{N}. \tag{3.12}$$

We solve Equation (3.12) using numerical continuation in the parameter A_1 starting from $A_1 = 0$, the corresponding solution being the n_{11}–bouncing state as defined by the system (3.3). Figure 3.13(a) shows the dependence of the inter-drop distances $d_i = \chi_{i+1} - \chi_i$ on the forcing amplitude A_1. While the distances d_2 (red), d_3

(orange) and d_4 (purple) remain roughly constant over the range of forcing amplitudes considered, the distance d_1 (blue) between drops 1 and 2 increases dramatically near $A_1/\lambda_F \approx 0.4$ and $A_1/\lambda_F \approx 0.8$, with plateaus in between. The plateaus are approximated well by the dashed lines in Figure 3.13(a), which denote the values of d_1 for unforced droplet chains, as predicted by the system (3.2). Specifically, the dashed line with the lowest value of $d_1 \approx 0.8\lambda_F$ corresponds to the n_{11} symmetric bouncing state, whereas the other lines with $d_1 \approx 1.3\lambda_F$ and $d_1 \approx 1.8\lambda_F$ correspond to asymmetric bouncing states, for which $d_1 \neq d_4$ and $d_2 \neq d_3$.

We proceed by assessing the stability of the unforced bouncing states (dashed lines in Figure 3.13(a)) for the lowest memory considered, $\gamma/\gamma_F = 0.66$, using the procedure described in Section 3.2. Specifically, we find the eigenvalues of the matrix Q in Equation (3.6), and find that states with $d_1 \approx 0.8\lambda_F$ and $d_1 \approx 1.8\lambda_F$ (black dashed lines) are stable, whereas the one with $d_1 \approx 1.3\lambda_F$ (gray dashed line) is unstable. Note that the wave field associated with the unstable bouncing state has a relatively large amplitude at the positions of the first and second drop (Figure 3.13(c)), as compared to the stable n_{11}–state (Figure 3.13(b)) and the dynamically stabilized state (Figure 3.13(d)), where the wave field of a droplet chain forced in the limit of high frequency $f \to \infty$ is given by

$$h(x) = \frac{AT_M}{T_F}\left[\frac{1}{2\pi}\int_0^{2\pi} \mathrm{J}_0(k_F(x - A_1\sin\sigma))\,\mathrm{d}\sigma + \sum_{\mathrm{j}=2}^{\mathrm{N}} \mathrm{J}_0(\mathrm{k_F(x-\chi_j)})\right]. \qquad (3.13)$$

The physical picture is that high-frequency forcing applied to the first drop may be used to drive transitions between bouncing states, wherein the distance d_1 between the first two drops increases in increments of size roughly $\lambda_F/2$ as the forcing amplitude A_1 is increased progressively, and the distances between the other drops remain roughly constant. Moreover, an unstable bouncing state may be effectively stabilized by a high-frequency periodic forcing of sufficiently large amplitude A_1, which leads to a wave field of diminished amplitude at the position of the second

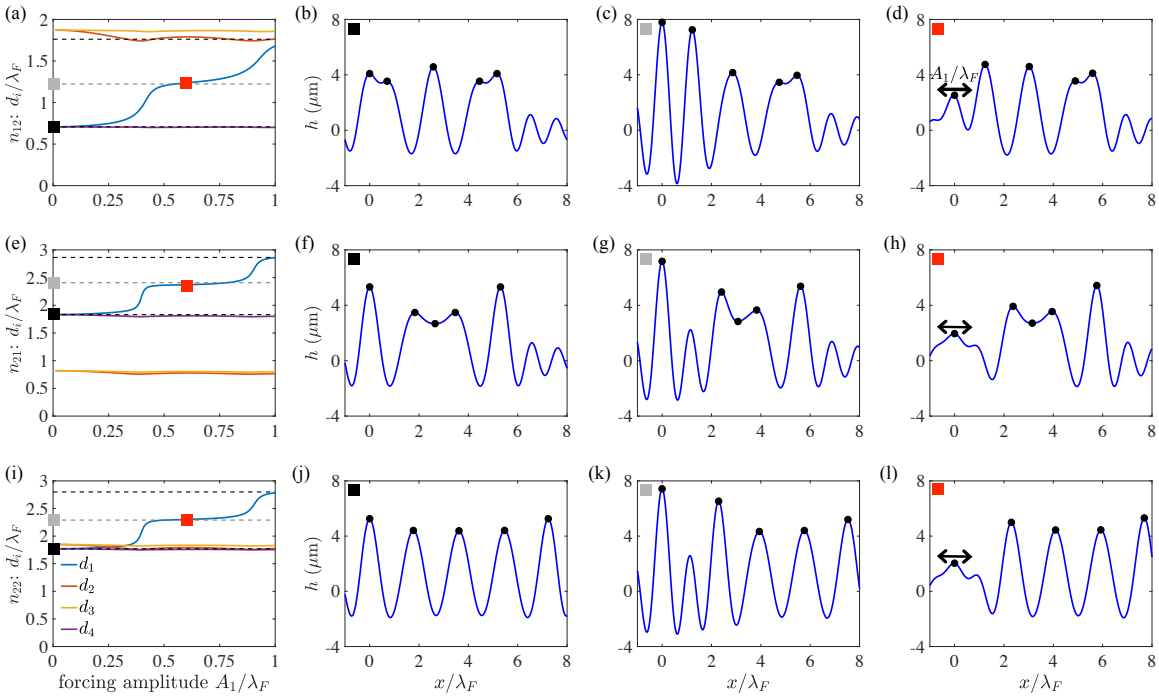

Figure 3.14 Bouncing states of a chain of five drops obtained in the limit of high forcing frequency, $f \to \infty$. The procedure in Figure 3.13 is repeated for chains initialized in the bouncing states n_{12} (Panels (a)–(d)), n_{21} (Panels (e)–(h)), and n_{22} (Panels (i)–(l)).

drop. We note that dynamical stabilization of bouncing states through a qualitatively similar mechanism is observed for droplet chains initialized in the n_{12}, n_{21} and n_{22}–states, as shown in Figure 3.14.

3.4 Discussion and Future Work

We have presented the results of a theoretical and numerical investigation into chains of bouncing droplets. We have characterized the equilibrium configurations of chains of five droplets, and found that they go unstable to an oscillatory instability as the bath's forcing acceleration γ/γ_F is increased progressively. We have observed that, with the exception of the n_{12}–bouncing state, the drop in the middle of the chain exhibits the largest oscillations at the onset of the instability (Figure 3.4). These results are qualitatively consistent with the experiments of Eddi *et al.* [36], who found

that quasi-1D aggregates of bouncers effectively melt from the interior at a critical value of the bath's forcing acceleration. We have also derived an approximation (Equation (3.7)) for the oscillation frequency of a droplet chain at the onset of the instability, whose associated prediction $f \approx 1$ Hz agrees well with the observations of Eddi *et al.* [36].

We have found that droplet chains may exhibit a complex dynamics when the drop at one end is subjected to sinusoidal forcing in the horizontal direction. Specifically, simple oscillatory motion is observed at relatively low memory (Figure 3.8(a) and (b)), while complex aperiodic behavior is observed at higher memory (Figure 3.8(c) and (d)). As is evident by comparing Figures 3.6 and 3.9, the dependence of the drop oscillation amplitude A_i on the forcing frequency f is described well by the linear theory presented in Subsection 3.3.1, provided the forcing amplitude A_1 on the first drop is relatively small, $A_1 \ll \lambda_F$. The dependence of A_i on f is more complex for larger values of A_1 (Figure 3.10), a regime in which nonlinear effects are expected to play an important role. At relatively high memory, the drops may oscillate with an amplitude larger than that prescribed (Figure 3.9(c)), $A_i > A_1$, suggesting that the drops effectively extract energy from the collective wave field and convert it to kinetic energy.

At the largest forcing amplitude A_1 and memory considered, periodic forcing may be used as a mechanism to generate chaotic dynamics (Figure 3.12(a)). In this regime, the droplet chain exhibits intermittent oscillations between the different bouncing states without settling near any of them (Figure 3.12(b)). This physical picture of a walker jumping chaotically between states has been reported in a number of settings, for example, in a rotating frame [55, 84], harmonic potential [88, 87, 86, 19], and circular [57, 32] and elliptical corrals [105]. While a walker's dynamics under periodic forcing has received less attention, Perrard [85] subjected a walker to a

periodically oscillating central force, $F = -(k_0 + k_1 \sin \omega t)x$, and observed transitions between circular orbits and lemniscates for suitable values of k_1 and ω.

In the limit in which the applied oscillation frequency of the first drop is large, $f \to \infty$, new bouncing states may be dynamically stabilized provided the forcing amplitude A_1 is sufficiently large (Figure 3.13(a)). This phenomenon is similar to the so-called Kapitza pendulum, in which a fast oscillation of the pivot point stabilizes the upward vertical position of the pendulum and destabilizes the downward vertical position [63, 64, 73]. We note that dynamic stabilization of unstable quantum states has also been achieved experimentally, for example in potassium Rydberg atoms subjected to strong pulsed electric fields [99] and atomic Bose-Einstein condensates subjected to periodic microwave pulses [59].

Our results indicate that a droplet chain exhibiting relatively large-amplitude oscillations may be viewed as a damped oscillator forced near resonance. Equation (3.5), which describes the linear small-amplitude oscillations of a chain of bouncers around their equilibrium positions, may thus be compared with the equations of motion of spring-mass-damper chains, which comprise a series of masses connected by linear springs and subjected to friction forces [98]. This analogy was noted by Borghesi *et al.* [17] in their study of promenading pairs of walking droplets. However, three significant differences are evident: first, the damping term $\dot{x}_i$ in the droplet chain is due to a drag, and thus depends only on the velocity of each particle instead of the particles' relative velocities $\dot{x}_i - \dot{x}_j$. Second, the interactions are long-range, unlike the nearest-neighbor interactions of spring-mass-damper chains: each drop experiences a wave field that results from the sum of the waves generated by all other drops. Third, the drops are coupled by a fluid-mediated memory and thus temporally nonlocal forces, as the wave force on each droplet is due to the waves generated in each droplet's past. Mathematically, the forces are not proportional to the difference $x_i - x_j$, as for linear springs, but rather to $x_i - X_j$, where X_j is an exponentially-weighted integral

of the position of drop j. In the low-memory regime, the effective spring constant is proportional to the memory time T_M, as is evident from Equation (3.7). The drop oscillation amplitude increases with T_M (Figures 3.9 and 3.10), a behavior consistent with the fact that the resonant oscillation amplitude in mass-spring systems increases with the spring constant [98]. We note that spring-mass lattices are the basic model for the description of phonons in crystalline solids [65], and that analogues of phonons have also been observed in a 1D microfluidic crystal, which consists of a chain of immiscible drops in a liquid-filled channel [14].

It is our hope that the theoretical predictions presented herein may be validated experimentally, a possible avenue being the protocol described by Perrard [85] for periodically forcing droplets using an oscillating magnetic field. Longer droplet chains ($N \gg 5$) may also be studied theoretically, although the stroboscopic model (Equation (2.2)) would need to be modified to account for the exponential decay of the surface waves in the far field [26]. A worthwhile future direction would be to explore hydrodynamic analogues of Floquet engineering [20], wherein a time-dependent forcing is tuned in order to control a quantum system. While the present study was restricted to chains of bouncers forced sinusoidally at one end, different forms of periodic forcing could be used to control the structure and dynamics of more complex bouncing droplet lattices.

CHAPTER 4

PHASE SEPARATION IN COLLOID-POLYMER MIXTURES

In this chapter, we describe our work on phase transitions in colloid-polymer suspensions. This work was supported by the NASA grant #80NSSC20K0274, entitled "Phase transitions in colloid-polymer mixtures in microgravity," with PI A. U. Oza (Department of Mathematical Sciences, NJIT) and co-PIs B. Khusid (Chemical and Materials Engineering, NJIT), L. Kondic (Department of Mathematical Sciences, NJIT) and W. V. Meyer (Universities Space Research Association at NASA Glenn Research Center).

4.1 Introduction and Background

We begin by giving a brief historical introduction to the study of colloidal suspensions. The seminal computer simulations of Alder & Wainwright [7] first demonstrated that a system of hard spheres could exhibit a fluid-to-crystal phase transition. This prediction was confirmed in experiments by Pusey & Van Megen [96], who progressively increased the concentration of colloids in a suspension and observed a progression from colloidal fluid, to fluid and crystal phases in coexistence, to full crystallization. These phase transitions are now understood to be driven by entropy alone; while counterintuitive, at relatively large colloid concentrations the system's entropy is actually *increased* in a more ordered (crystalline) state, as the particles are afforded more "wiggle room" as compared to the disordered fluid phase.

Pusey & van Megen [96] also observed that, for a colloidal suspension in the crystalline phase, as the colloidal concentration was progressively increased the system transitioned to a glass-like state, wherein the colloidal particles were jammed in a disordered fashion. This tantalizing discovery motivated the experiments of Zhu *et al.* [121], who analyzed microgravity experiments conducted on the Space Shuttle

(STS-73). While they observed the phase transition from liquid to crystal, they did not observe the glass state, indicating that the glass state may be an artifact of gravitational effects. The crystalline state observed in these experiments was shown by Cheng *et al.* [25] and more recently in the ACE-T11 experiments (2021) to have face-centered cubic geometry. Zhu *et al.* [121] also observed that the crystals grew via dendritic growth; rather than growing radially outward in a symmetric fashion, the crystals grew a few "arms" or dendrites to which colloidal particles were progressively added.

The growth of colloidal crystals has been modeled theoretically by Russel *et al.* [103], who considered a phase-field description of the growth of a single colloidal crystal. Specifically, they proposed that the colloid concentration inside and outside the crystal be given by two different continuum fields, each of which evolves according to its own diffusion equation. The two fields are coupled by boundary conditions at the edge of the crystal, a coupling that determines the crystal growth rate. This work was recently extended by Lam *et al.* [70], who both theoretically and numerically investigated the effects of a concentration-dependent diffusion coefficient on the crystal growth.

While colloidal suspensions are interesting in their own right, the addition of non-adsorbing polymer to a colloidal suspension makes the phase behavior even richer. The seminal work of Asakura & Oosawa [11] first proposed a theory for the so-called "depletion interactions" that arise when two solid bodies (*i.e.,* colloids) are immersed in a solution of polymers. This mechanism will be described in detail in Subsection 4.3.1. Gast *et al.* [52] and Lekkerkerker *et al.* [74] built on this work and investigated the phase behavior of colloid-polymer suspensions. Lekkerkerker *et al.* [74] found that, for sufficiently small polymers (relative to colloid size), a colloid-polymer mixture admits two equilibrium phases, a fluid and a crystal, analogous to the colloid-only system described in the preceding paragraphs. Above a critical

polymer size, the system was found to admit three phases: a gas, a crystal, and an intermediate liquid phase.

These predictions were confirmed in the terrestrial experiments of Ilett *et al.* [61], who studied suspensions consisting of polymethylmethacrylate (PMMA) spheres and the polymer polystyrene in the solvent cis-decalin. Subsequent experiments investigated the structure of the suspensions near the triple point, a regime in which the gas, liquid and crystalline phase coexist [79]. The kinetics of phase separation was also studied experimentally [91, 75], where it was found that the three phases can emerge via distinct pathways depending on the colloid volume fraction and polymer concentration. These kinetic pathways were rationalized using a "toy" Cahn-Hilliard model by Evans *et al.* [45]. The role of an intermediate liquid phase in unbinding a gas-solid interface has also been studied studied theoretically using a generic Cahn-Hilliard theory [44, 42, 43].

Microgravity experiments on the International Space Station were first analyzed by Bailey *et al.* [12], who presented evidence that spinodal decomposition at early stages of the experiment eventually gave way to fluid-driven coarsening at long timescales (Figure 4.1). Other microgravity experiments were studied by Sabin *et al.* [104], who found that, in certain parameter regimes, gas-liquid phase separation could be arrested due to the formation of a so-called crystal gel consisting of crystalline strands that run through the entire sample. The goal of this chapter is to process the images from additional microgravity experiments, and to formulate a theoretical model for the phase separation dynamics.

4.1.1 Experimental details and overview

In their online database, NASA has provided plentiful information on their BCAT (Binary Colloid Alloy Test) experiments [1]. The four BCAT experiments conducted, BCAT-3, 4, 5 and 6, each consist of ten samples. For all of these, the absolute

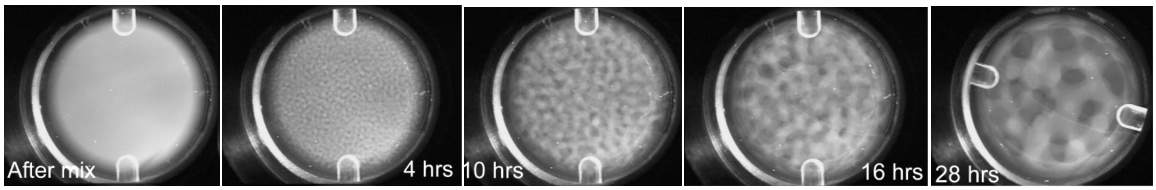

Figure 4.1 Images from Bailey *et al.* [12] showing microgravity experiments of phase separation in a colloid-polymer suspension. The time after mixing is shown, and sample cell is 2 cm in diameter.

temperature was approximately $T \approx 295.15$ K (22° Celsius) [5]. Each sample has different values for system parameters such as initial (homogenized) colloid volume fraction ϕ, polymer concentration ρ, and colloid particle size. Several of the samples were aimed toward studying other phenomena such as seeded crystal growth, and include colloids of varying sizes; others have only colloids and no polymer. Those samples are not considered in this dissertation, as we are interested in the phase behavior in colloid-polymer suspensions. There were also a few samples for which the images were of low quality and not amenable to analysis; we exclude these also. The relevant samples for the purposes of this dissertation are Samples 1, 2, 4 and 6 of BCAT-3, Samples 1-3 of BCAT-4, and Samples 4-8 of BCAT-5. In all of these samples, the colloids are polymethyl-methacrylate (PMMA) spheres, the solvent is a mixture of decalin and tetralin, and the polymer is polystyrene [2, 5]. The dimensions of the "visible volume" of the sample cells are $4 \times 10 \times 20$ mm [104]. Other system parameter values (colloid size, colloid volume fraction, polymer size, and polymer concentration) for each of the samples are given in Tables 4.1, 4.2, and 4.3. The parameter n_R in the last column of each table is related to the polymer concentration, and will be defined in Section 4.3.

NASA has documented their BCAT experiments by photographing the colloid-polymer mixture just after mixing it and then approximately every thirty minutes after that. Figure 4.2 shows two of the BCAT images: one taken 13 hours after mixing,

Table 4.1 Details, parameters, and specifications for BCAT-3 Samples 1, 2, 4 and 6 [2, 5].[a]

Sample	*Colloid volume fraction* ϕ	*Colloid radius* a	*Polymer concentration* ρ	*Polymer radius of gyration* δ	*Ratio* $\xi = \delta/a$	$\frac{4\pi\delta^3}{3} n_R$
1	0.2273	97 nm	0.814 mg/mL	120 nm	1.24	24.58
2	0.22	97 nm	0.781 mg/mL	120 nm	1.24	18.57
4	0.21	97 nm	0.737 mg/mL	120 nm	1.24	12.83
6	0.2112	97 nm	0.742 mg/mL	120 nm	1.24	13.40

[a]For all samples in this table, the solvent composition is 47:53 decalin/tetralin, and the temperature is $T = 295.15$ K.

Table 4.2 Details, parameters, and specifications for BCAT-4 Samples 1, 2, and 3 [2, 5].[a]

Sample	*Colloid volume fraction* ϕ	*Colloid radius* a	*Polymer concentration* ρ	*Polymer radius of gyration* δ	*Ratio* $\xi = \delta/a$	$\frac{4\pi\delta^3}{3} n_R$
1	0.2237	97 nm	0.797 mg/mL	120 nm	1.24	21.37
2	0.2173	97 nm	0.770 mg/mL	120 nm	1.24	16.80
3	0.2151	97 nm	0.760 mg/mL	120 nm	1.24	15.48

[a]For all samples in this table, the solvent composition is 47:53 decalin/tetralin, and the temperature is $T = 295.15$ K.

Table 4.3 Details, parameters, and specifications for BCAT-5 Samples 4-8 [2, 5, 104].[a]

Sample	*Colloid volume fraction* ϕ	*Colloid radius* a	*Polymer concentration* ρ	*Polymer radius of gyration* δ	*Ratio* $\xi = \delta/a$	$\frac{4\pi\delta^3}{3} n_R$
4	0.223	216 nm	0.797 mg/mL	120 nm	0.56	0.92
5	0.2173	216 nm	0.770 mg/mL	120 nm	0.56	0.85
6	0.24	229 nm	0.88 mg/mL	120 nm	0.52	0.99
7	0.29	229 nm	0.72 mg/mL	120 nm	0.52	1.23
8	0.35	229 nm	0.55 mg/mL	120 nm	0.52	1.81

[a]For all samples in this table, the solvent composition is 45:55 decalin/tetralin, and the temperature is $T = 295.15$ K.

and the other taken 65 hours after mixing. The images illustrate the separation of the two phases (gas and liquid) as time progresses—specifically, the gas and liquid phase domains become progressively larger. Bailey *et al.* [12] found that the domains grew with a power law behavior $\sim t^{1/3}$ at short times, and $\sim t$ at later times. They hypothesized that fluid flows were responsible for the long-time growth, but this hypothesis has not yet been validated in numerical simulations.

Our main objective in the work presented in this dissertation is to present, simulate, and validate a new model that utilizes the Cahn-Hilliard equation for phase separation, but modifies it to account for fluid flow. Specifically, we have written and implemented a spectral code that solves the Cahn-Hilliard equation both with and without fluid flow. In order to validate and improve upon our new model, we have compared our simulation results with actual experimental images from NASA, a process which required both pre-processing and analysis of these images.

We proceed by discussing the two principal research objectives of this project. In Section 4.2, we describe the process used to prepare and enhance the images after downloading them from NASA's database, as well as the image analysis we have done in order to describe the change in domain size (phase separation) in time. In Section 4.3, we present a mathematical model that accounts for hydrodynamic effects by coupling the incompressible Stokes equations with the Cahn-Hilliard equation. We then show results from numerical simulations of our model in Section 4.4, and compare these results with the experimental data obtained from the image analysis described in Section 4.2. Finally, we discuss future directions for the project in Section 4.5.

4.2 Image Processing and Analysis

As mentioned in Section 4.1, NASA has an extensive database of photographic images of their BCAT experiments [1]. Our goal was to directly compare and contrast results

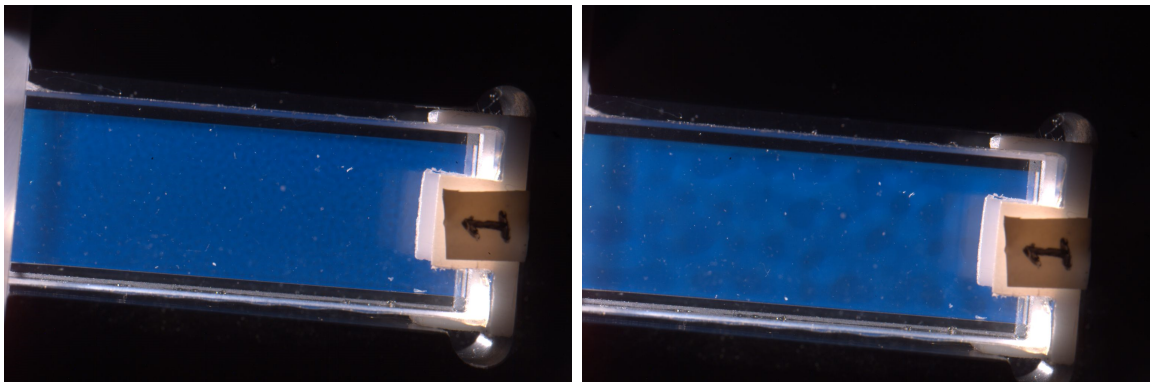

Figure 4.2 Images taken by NASA [1] of their BCAT experiment at (left) $t = 13$ hours and (right) $t = 65$ hours. Notice how the liquid and gas domains are much bigger for the $t = 65$ image than they are for the $t = 13$ image; this illustrates the transition of the mixture from one homogeneous phase to two distinct liquid and gas phases.

from simulations of our model with these images. Doing this requires a way of quantitatively describing the rate of the domain coarsening exhibited in the images.

To this end, we had to process the images first to make them amenable to quantitative analysis. This was done using the free software ImageJ; the details are given in Subsection 4.2.1. Then, a quantitative description of the size of the liquid and gas domains for a given image was needed; we adapted an existing MATLAB code by Dr. Michael Lam to compute the characteristic domain length using an autocorrelation matrix. This algorithm is detailed in Subsection 4.2.2. Finally, we validated our method by comparing our results with those of Sabin *et al.* [104].

4.2.1 Image processing

The image processing procedure can be further subdivided into two distinct operations: *cropping* and *enhancement* of the images; the details of each are given in the paragraphs below. The cropping was performed using an algorithm we wrote in MATLAB. The enhancement was performed in ImageJ, using a package called MIJ [4, 3] that allows an instance of ImageJ to be opened from within a MATLAB script. In this way, ImageJ commands and macros can be conveniently implemented

on image matrices directly from within MATLAB. We note here that automating the cropping and enhancement processes for each sample required using MATLAB to read in the .txt file corresponding to that set of images, which was also provided in the NASA PSI database. These files contained information such as the filename of each image, along with the exact date and time at which the image was taken. This allowed us not only to load each image using a for-loop in MATLAB, but also to save an array containing the corresponding times for all images so that we could produce a time-accurate plot later on after conducting the image analysis described in Subsection 4.2.2.

Cropping Our first step in processing the raw images (Figures 4.2 and 4.3(a)) from NASA's PSI database was to convert them all to .png format. This was easily done in MATLAB. The next step was to crop out the sample cell and extraneous labels, leaving only the cell's contents (the colloid-polymer mixture) in the frame.

Accomplishing this for all images proved to be a nontrivial task: the location and angle of the sample in the frame is not consistent across all images, indicating that the camera was moved around over the course of the experiments. Thus, each image had to be individually straightened so that the sample appeared straight in the frame, and then cropped. Because we downloaded several thousand images from the database, rotating and cropping each image by hand would be impractical. Thus, we automated this process by developing an algorithm in MATLAB that first rotates (straightens) each image and then crops it to eliminate the dark background, the frame of the cell containing the sample, and the sample number label, leaving only the sample domain.

To straighten a given image, our algorithm locates the top edges of the sample cell container as follows, an analogous procedure being used for the bottom edges. Let $I(i, j)$ be the image matrix, with values representing the grayscale intensity of the

image and $1 \leq i \leq N$, $1 \leq j \leq M$. For a given j, we define $V_i^{(j)} \equiv \text{std}\{I(N/2+k, j) : 1 \leq k \leq i\}$ for $1 \leq i \leq N/2$, where std$\{\cdot\}$ denotes the standard deviation of the list of values specified in the brackets. Specifically, the list of image values inside the brackets grows with i, and thus corresponds to vertical slices of the image of increasing length. We have assumed that N is even for simplicity of exposition; the procedure can be easily generalized to handle odd N. Note also that generally the pixels in the center of the image fall somewhere within the sample domain and not on the sample container, label, or background. We then take the forward difference (in i) of the values $V_i^{(j)}$, $\Delta V_i^{(j)} \equiv V_{i+1}^{(j)} - V_i^{(j)}$, and identify the value of i at which $\Delta V_i^{(j)}$ is maximized. This point is identified as the top of the image, for the particular value of j under consideration. This process is repeated for all values of j, and a line of best fit is drawn through the identified values of i, which demarcates the top of the image. The slopes of the fit lines for the top and bottom are then used to determine the angle at which the image must be rotated in order to make it straight, and the image is adjusted accordingly. With the top and bottom of the container already located, our MATLAB code then crops the image in the vertical direction by eliminating the pixels above the top line and below the bottom line.

A similar process is then used to locate the left and right boundaries of the container, and the outer pixels are then eliminated accordingly in the horizontal direction, resulting in our cropped image. For most of the image sets, we cropped a few additional rows (columns) of pixels from the top and bottom (sides) at this stage due to visible differences in the phase domain structures at the boundaries of the sample cell. We seek results that we can compare as closely as possible with our model simulations, which describe behavior in the absence of (or far away from) boundaries.

Enhancement After the cropping of images is completed, the image is converted to grayscale and is ready to be enhanced. The steps towards an enhanced image are outlined in the caption of Figure 4.3. The process is automated by running ImageJ as a "macro" from within MATLAB. In summary, the original image (Figure 4.3(a)) contains the sample cell and extraneous labels, which are first removed (Figure 4.3(b)) as described in the paragraphs above. The brightness/contrast is then adjusted (Figure 4.3c), and then the background is subtracted (Figure 4.3d). The contrast is enhanced again (Figure 4.3e). The image is then smoothed and despeckled, which generates the final enhanced image shown in Figure 4.3f.

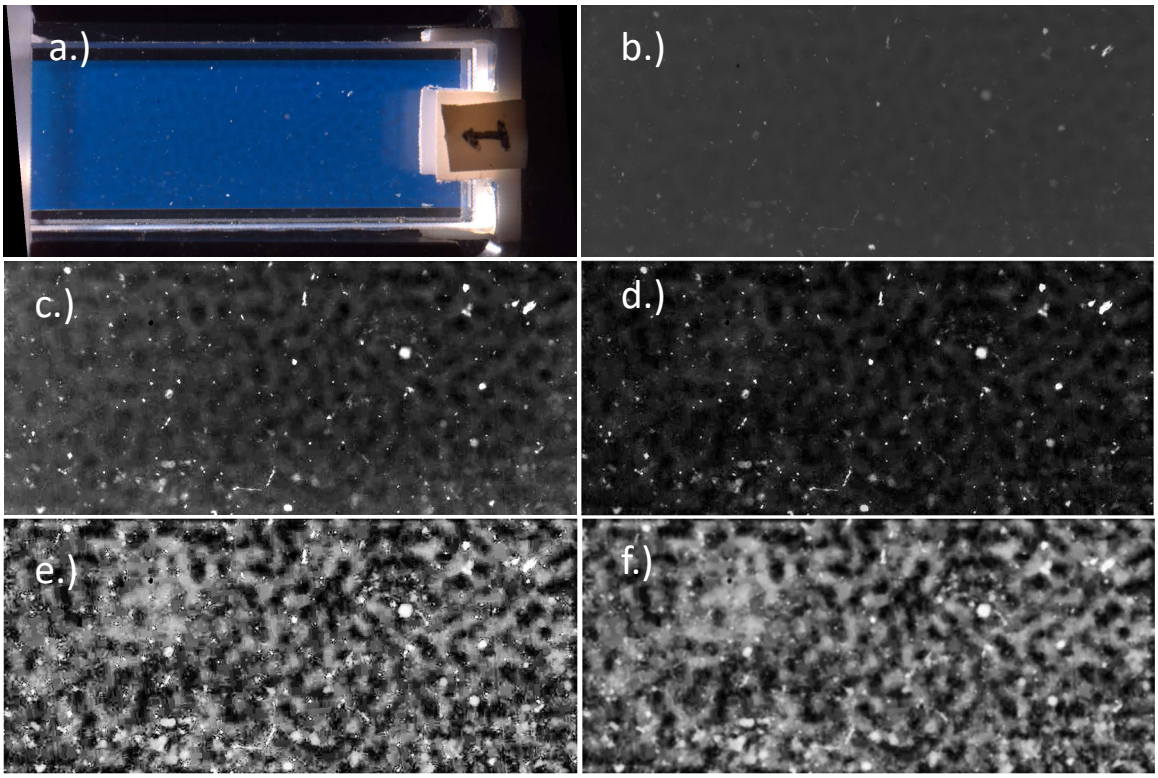

Figure 4.3 Image processing steps described in Subsection 4.2.1, applied to a single image from BCAT-3 Sample 1. (a) Original image. (b) Image converted to grayscale, and after sample cell and background are removed. (c) Image after brightness/contrast is adjusted. (d) Image after the background is subtracted, with the rolling ball radius set to 30. (e) Image after contrast is enhanced. (f) Image after it is smoothed and despeckled, which corresponds to the final image.

The background subtraction step (Figure 4.3d) deserves further explanation. The background is subtracted using the so-called *rolling-ball algorithm* [108]; briefly, the idea is to represent a 2D grayscale image as a 3D surface, and then roll a sphere (or paraboloid) along this surface so that a background surface is created [101]. Subtracting this background surface from the original image allows for background fluctuations to be removed. Determining the appropriate value of the rolling ball radius can be difficult [101]; for instance, a large radius will create artificial large domains that give the appearance of advanced phase separation, while a small radius will make an image look pixelated. For BCAT-3 Sample 1, we decided to let the rolling ball radius increase linearly with time; specifically, we set the radius as the maximum of $r_{min} = 15$ and $r_0 + (r_1 - r_0)(t - t_0)/(t_1 - t_0)$, where $(t_0, r_0) = (19.5, 30)$ and $(t_1, r_1) = (78.5, 300)$ are the time (in hours) and radius values corresponding to the images "iss013e33636" and "iss013e34600." We deliberately selected one early-time image, for which the phase separation was visible but the domains were still very small, and one later-time image, for which the phase domains had grown relatively large but the phase separation had not completely finished. We then experimented with the rolling-ball radius values on these two images to find the best value for each of them; we took these values to be our r_0 and r_1. The reason we have defined a minimum value r_{min} for the rolling-ball radius is because, in some cases, the values prescribed for very early times by our linear formula are too small even for the earliest images. Thus, we select r_{min} based on how the very earliest images look, by eye, with the rolling-ball radius set to that value. Thus, the formula we use for the rolling-ball radius for the image corresponding to each time t is given by:

$$\max\big(r_{min}, r_0 + (r_1 - r_0)(t - t_0)/(t_1 - t_0)\big) \tag{4.1}$$

We repeated the same process for the other samples. For some of these samples, at very late times the phase separation tends to slow down significantly or even become

stagnant. For this reason, the rolling-ball radius prescribed by our linear formula can increase to be too large for images at times after which this slowing down has occurred. To avoid this, we also set a maximum value r_{max} for the rolling-ball radius. Note that this was only necessary for certain samples; for these, we simply modify the formula (4.1) as follows:

$$\min\Big(r_{max}, \max\big(r_{min}, r_0 + (r_1 - r_0)(t - t_0)/(t_1 - t_0)\big)\Big) \tag{4.2}$$

It is important to note that r_0, r_1, r_{min} and r_{max} are in pixels. For this reason, the appropriate values for these parameters depend not only on the actual size of the phase domains, but also on the size, in pixels, of the images. In looking through the database, we found that the resolution of the experimental images varied somewhat between samples. In addition, the photographs were taken from a further distance away for some of the samples than for others, effectively resulting in a discrepancy in image resolution.

We use one of (4.1) or (4.2), as appropriate, for each of the BCAT samples, choosing appropriate values for t_0, t_1, r_0, r_1, and r_{min} (and r_{max}, if applicable) for each sample's image set. These values, for all of the samples we analyzed, are given in Table 4.4.

Figures 4.4-4.14 illustrate the progression of the phase domain coarsening in time, as seen in the enhanced images. Subsection 4.2.2 describes our algorithm that characterizes this growth quantitatively; the image enhancement makes it much easier for our algorithm to distinguish between colloid-rich "light" and colloid-poor "dark" phases. Note that the round plastic object in the BCAT-3 Sample 6 images taken at $t = 10$ and $t = 20$ hours (Figure 4.7) is the magnetic stir bar used by the astronauts to mix the samples. Because the stir bar entered the frame at a very early time and remained, moving to different locations at different times, until approximately $t = 55$

Table 4.4 Parameters for the linear equations (4.1) and (4.2) for obtaining appropriate values for the rolling-ball radius in the image processing algorithm, for all of the samples we have analyzed.

BCAT-Sample	r_0 (pixels)	r_1 (pixels)	t_0 (hours)	t_1 (hours)	r_{min} (pixels)	r_{max} (pixels)
3-1	30	300	19.5	78.5	15	n/a
3-2	20	100	20	327	15	n/a
3-4	15	40	57.72	172.72	8	n/a
3-6	40	50	119.45	470.21	20	n/a
4-1	2	9	7.64	40.21	5	n/a
4-2	8	300	13	73	5	n/a
4-3	11	100	5.46	81.46	5	250
5-4	20	90	3.77	35.22	15	n/a
5-5	50	450	10.71	67.61	25	n/a
5-6	5	55	0.93	17.93	3	57
5-7	10	55	1.96	44.48	5	57
5-8	10	60	2.72	24.02	5	100

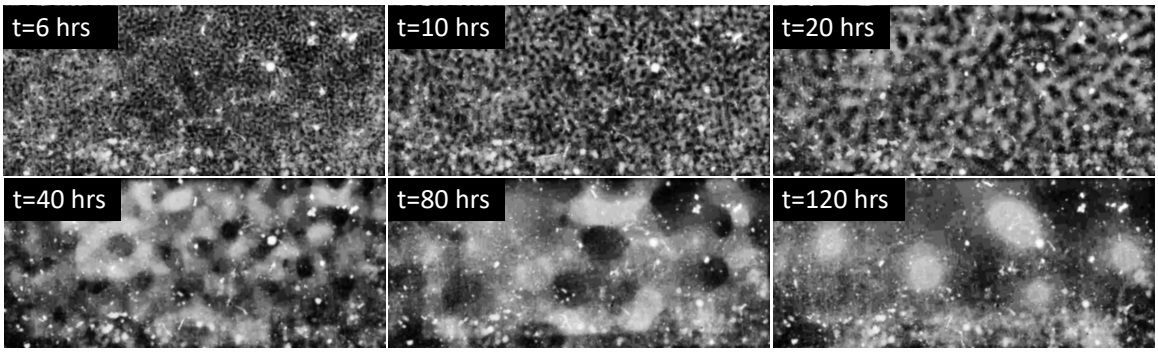

Figure 4.4 Time evolution of BCAT-3, Sample 1. Images are taken from the NASA PSI database and processed according to the procedure described in Subsection 4.2.1. Light (dark) areas indicate colloid-rich (poor) regions. The height, in millimeters, of the sample domains pictured in these images is ≈ 10 mm.

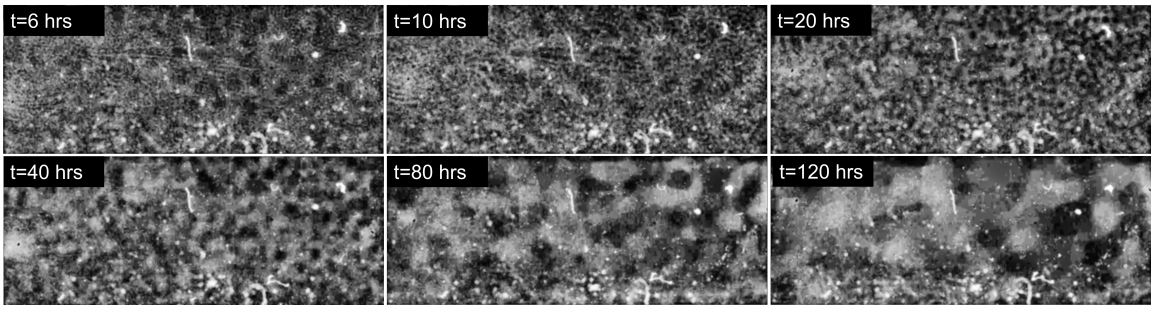

Figure 4.5 Time evolution of BCAT-3, Sample 2. Images are taken from the NASA PSI database and processed according to the procedure described in Subsection 4.2.1. Light (dark) areas indicate colloid-rich (poor) regions. The height, in millimeters, of the sample domains pictured in these images is ≈ 10 mm.

hours, we omitted the early-time images from the BCAT-3 Sample 6 phase domain growth curve in Figure 4.16.

4.2.2 Image analysis: quantifying phase domain growth

It is evident simply from looking at the enhanced images (Figures 4.4-4.14) that the phase domains coarsen as time progresses. In order to quantify this phase domain growth, we implemented an algorithm in MATLAB that measures the dominant length scale for each given image, as described in the paragraphs below. Note that the image enhancement procedure described in Subsection 4.2.1 makes it much easier for our algorithm to detect the difference between colloid-rich (light) regions, whose

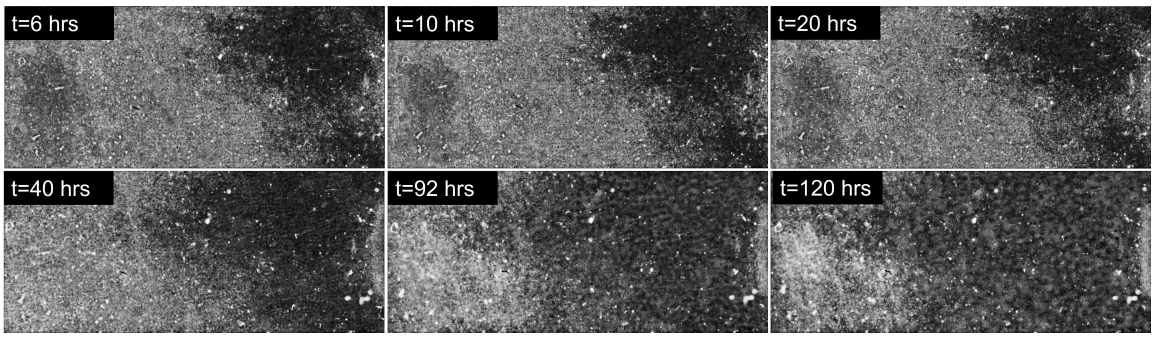

Figure 4.6 Time evolution of BCAT-3, Sample 4. Images are taken from the NASA PSI database and processed according to the procedure described in Subsection 4.2.1. Light (dark) areas indicate colloid-rich (poor) regions. The height, in millimeters, of the sample domains pictured in these images is ≈ 10 mm.

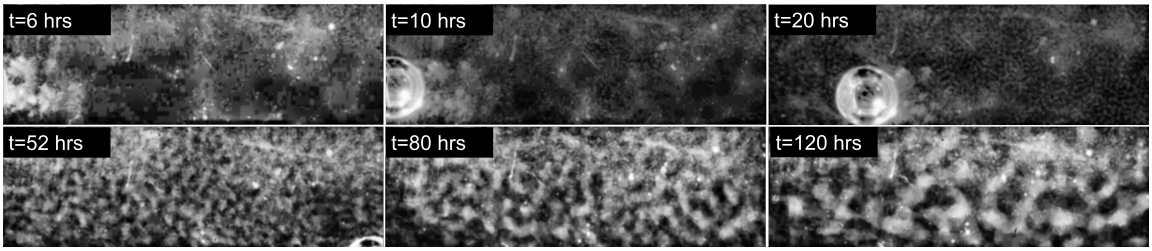

Figure 4.7 Time evolution of BCAT-3, Sample 6. Images are taken from the NASA PSI database and processed according to the procedure described in Subsection 4.2.1. Light (dark) areas indicate colloid-rich (poor) regions. The height, in millimeters, of the sample domains pictured in these images is ≈ 10 mm. The circular object in the images taken at $t = 10$ and $t = 20$ hours is the magnetic stir bar used by the astronauts to mix the samples; we omitted all images where this was present from the autocorrelation curve in Figure (4.16).

pixels have higher grayscale values, and colloid-poor (dark) regions, whose pixels have lower values.

Our phase domain growth characterization algorithm measures the dominant length scale for each image using an autocorrelation function. The autocorrelation matrix C for an $N \times M$ (in pixels) image I is a $(2N-1) \times (2M-1)$-matrix with entries

$$C_{ij} = \sum_{k=0}^{N-1} \sum_{l=0}^{M-1} I(k,l)I(k-i,l-j), \qquad -(N-1) \leq i \leq N-1$$
$$-(M-1) \leq j \leq M-1. \tag{4.3}$$

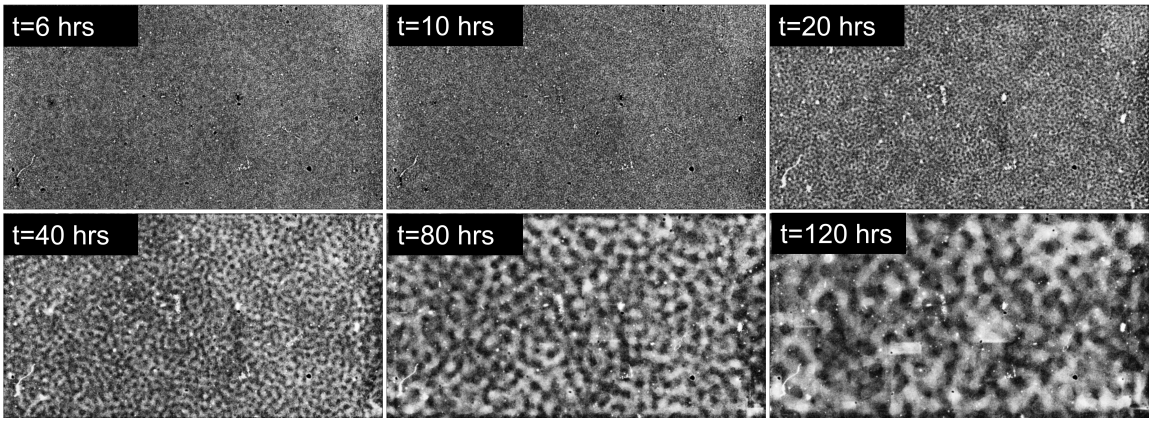

Figure 4.8 Time evolution of BCAT-4, Sample 2. Images are taken from the NASA PSI database and processed according to the procedure described in Subsection 4.2.1. Light (dark) areas indicate colloid-rich (poor) regions. The height, in millimeters, of the sample domains pictured in these images is ≈ 10 mm.

For each image, we compute the autocorrelation matrix C in MATLAB, and then we select the largest-possible centered square box of data. Since the image (and thus the autocorrelation matrix) is shorter in the vertical direction than in the horizontal direction, *i.e.,* $N < M$, this is done by selecting the $(2N-1) \times (2N-1)$ matrix from the horizontal center of the autocorrelation matrix. We do this for several reasons: 1) our model simulations are done on a square domain, and 2) projecting onto one dimension, as described in the paragraphs below, is more easily implemented on a square matrix.

This 2D autocorrelation matrix C, an example of which is shown in Figure 4.15(a), is then averaged in the azimuthal direction, thus obtaining the radial autocorrelation function $\tilde{C}(r)$. Practically, this is done by converting to polar coordinates and integrating C with respect to the angle θ using the trapezoidal rule. The characteristic length scale λ_a for a given image is found by selecting the first maximum of the curve $\tilde{C}(r)$, as shown in Figure 4.15(b). This value is a measure of the typical distance between colloid-rich (or colloid-poor) domains. Plotting λ_a vs. time t, as depicted in Figure 4.15(c), gives a quantitative description of how the phase domains are growing

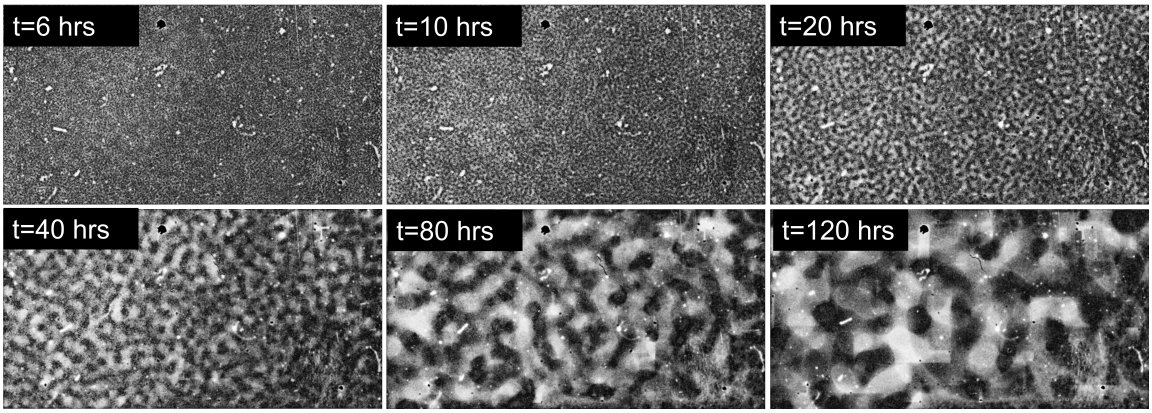

Figure 4.9 Time evolution of BCAT-4, Sample 3. Images are taken from the NASA PSI database and processed according to the procedure described in Subsection 4.2.1. Light (dark) areas indicate colloid-rich (poor) regions. The height, in millimeters, of the sample domains pictured in these images is ≈ 10 mm.

in time. The results for all of the samples listed in Tables 4.1, 4.2 and 4.3 are shown in Figures 4.16, 4.17, and 4.18, respectively.

In the BCAT-3 plot (Figure 4.16), it appears that higher colloid volume fraction ϕ_0 and polymer concentration ρ correspond with faster growth of the phase domains. Note that the colloid radius a and polymer radius of gyration δ are the same for all of the samples in Figure 4.16; the only parameters that vary between samples are ϕ_0 and ρ (see Table 4.1). In addition, the values of ϕ_0 and ρ in this sample set are decreased together across the sample number: both values are largest for Sample 1, followed by Sample 2, followed by Sample 6, and smallest for Sample 4. Thus, it is unclear which of these parameters is more influential in the increase of the phase domain growth rate; the values of the slopes of the autocorrelation curves increase with both ϕ_0 and ρ.

In BCAT-4 (Figure 4.17), ϕ_0 and ρ are similarly decreased together going from Samples 1 through 3, and a and δ are the same for all samples (see Table 4.2.) The slopes of Samples 1 and 2 follow the same trend as in Figure 4.16, since ϕ_0 and ρ are larger in Sample 1 than in Sample 2, and so are the slopes of the autocorrelation curves. On the other hand, Sample 3 does not follow this rule: despite having the

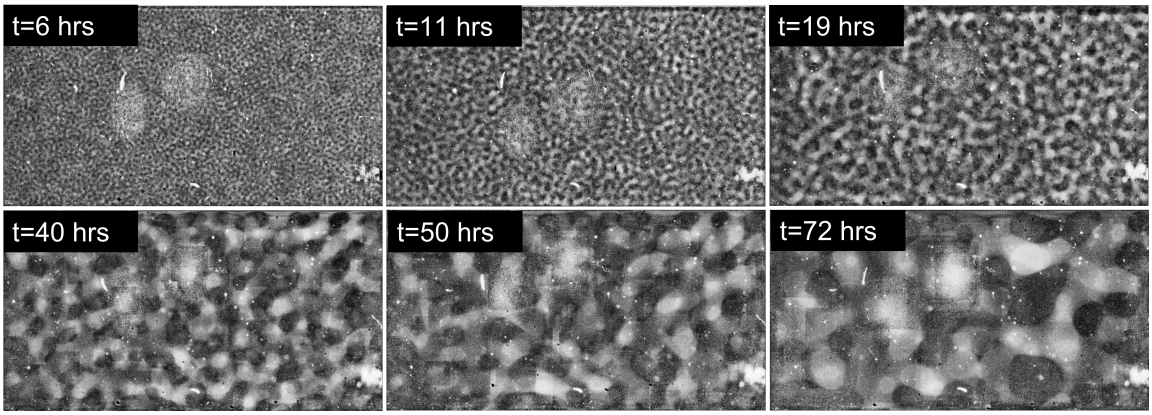

Figure 4.10 Time evolution of BCAT-5, Sample 4. Images are taken from the NASA PSI database and processed according to the procedure described in Subsection 4.2.1. Light (dark) areas indicate colloid-rich (poor) regions. The height, in millimeters, of the sample domains pictured in these images is ≈ 10 mm.

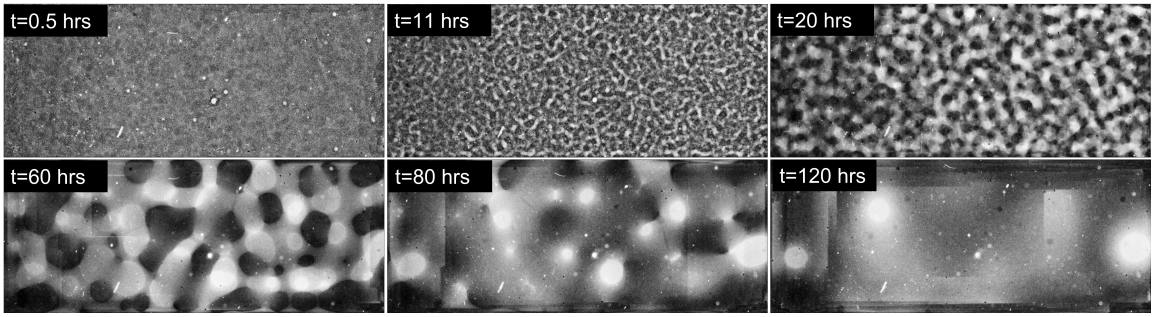

Figure 4.11 Time evolution of BCAT-5, Sample 5. Images are taken from the NASA PSI database and processed according to the procedure described in Subsection 4.2.1. Light (dark) areas indicate colloid-rich (poor) regions. The height, in millimeters, of the sample domains pictured in these images is ≈ 10 mm.

smallest ϕ_0 and ρ values, its autocorrelation curve has the steepest slope. It is unclear why this is the case, making this single sample an outlier. We also note that the gap in data points in the Sample 1 curve is due to lack of images corresponding to those times in the NASA PSI database. This was likely a result of the camera malfunctioning. Due to the sparseness of image data, we chose not to include an enhanced image time-evolution figure like Figures 4.4- 4.14 for BCAT-4 Sample 1.

Unlike in BCAT-3 and BCAT-4, the values of a and δ in BCAT-5 are not the same for all samples (see Table 4.3.) In addition, the colloids used in all of the BCAT-5 samples are more than twice the size of those used in BCAT-3 and BCAT-4.

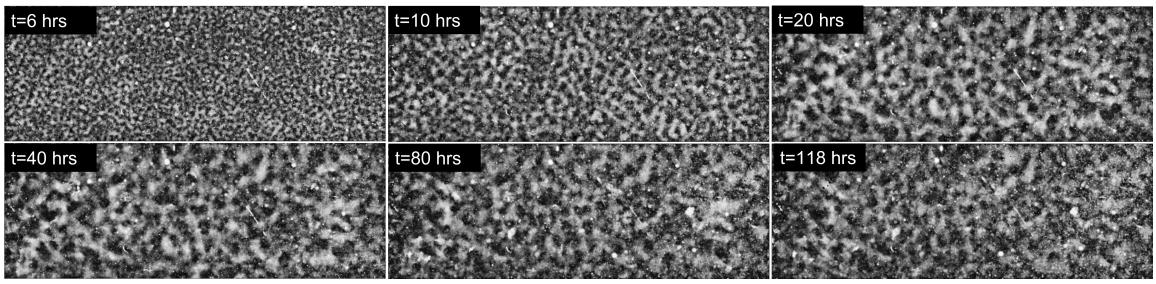

Figure 4.12 Time evolution of BCAT-5, Sample 6. Images are taken from the NASA PSI database and processed according to the procedure described in Subsection 4.2.1. Light (dark) areas indicate colloid-rich (poor) regions. The height, in millimeters, of the sample domains pictured in these images is ≈ 10 mm.

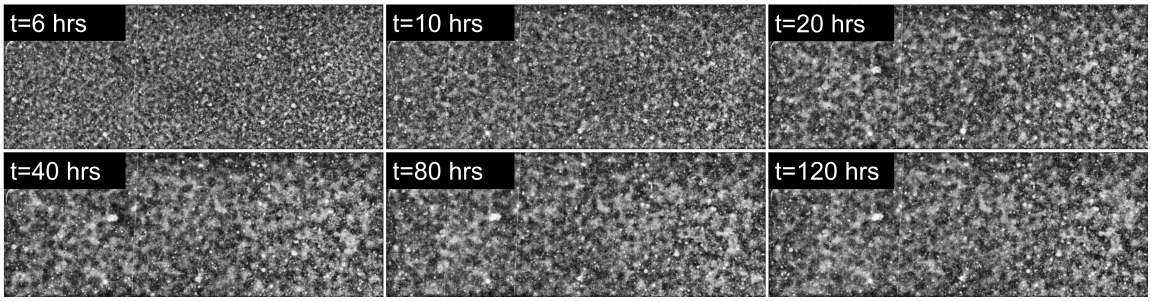

Figure 4.13 Time evolution of BCAT-5, Sample 7. Images are taken from the NASA PSI database and processed according to the procedure described in Subsection 4.2.1. Light (dark) areas indicate colloid-rich (poor) regions. The height, in millimeters, of the sample domains pictured in these images is ≈ 10 mm.

The colloid radius a is largest in Samples 6, 7 and 8, while δ remains the same; the ratio $\xi = \delta/a$ is thus smaller for these samples than it is for any of the others. As discussed in Section 4.1, the value of ξ plays a critical role in controlling the topology of the phase diagram for colloid-polymer mixtures. We note that, despite the smaller value of ξ for the BCAT-5 samples, three-phase coexistence is still predicted in the equilibrium theory proposed by Lekkerkerker *et al.* [74].

The λ_a curves for BCAT-5 Samples 4 and 5 (Figure 4.18) grow at a faster rate than any of the BCAT-3 or BCAT-4 samples in spite of having ϕ_0 and ρ values that are very similar to those in the BCAT-3 and BCAT-4 samples. Moreover, domain growth proceeds roughly linearly in time in BCAT-5 Samples 4 and 5, similar to the behavior of the samples in BCAT-3 and BCAT-4. The values of both ϕ_0 and ρ in

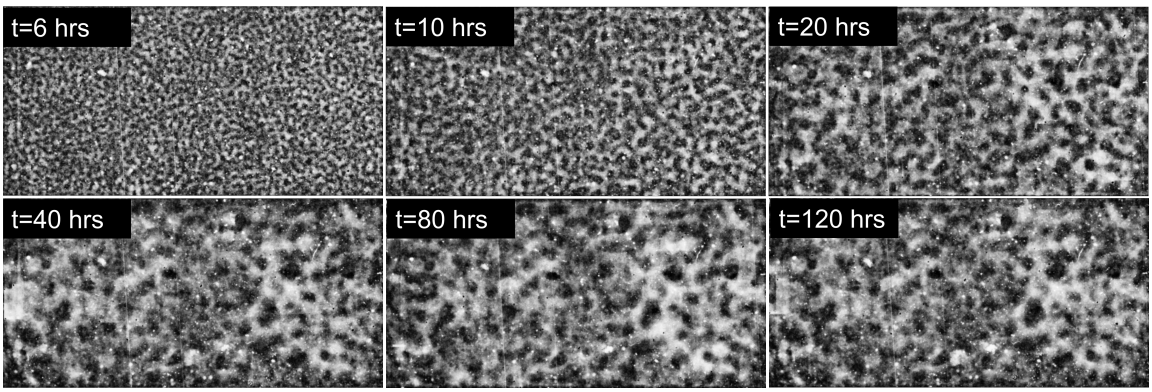

Figure 4.14 Time evolution of BCAT-5, Sample 8. Images are taken from the NASA PSI database and processed according to the procedure described in Subsection 4.2.1. Light (dark) areas indicate colloid-rich (poor) regions. The height, in millimeters, of the sample domains pictured in these images is ≈ 10 mm.

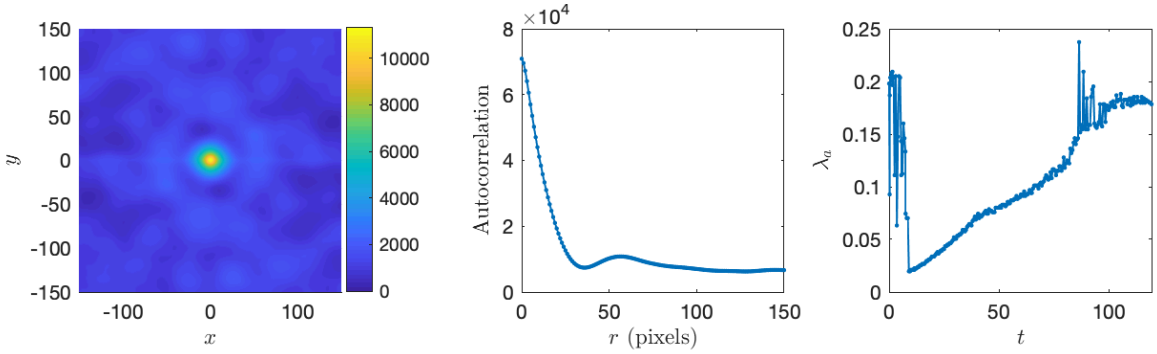

Figure 4.15 (a) Plot of the autocorrelation matrix C, as defined in Equation (4.3), for an image from BCAT-3 Sample 1, taken approximately 30 hours after mixing. (b) Azimuthally-averaged autocorrelation function $\tilde{C}(r)$ corresponding to the image in Panel (a). (c) Length scale λ_a (in cm) as a function of time (in hours).

Sample 5 are smaller than those of Sample 4, yet Sample 5 has a faster growth rate than Sample 4, which is the opposite of the behavior among the BCAT-3 samples in Figure 4.16.

The λ_a curves for BCAT-5 Samples 6, 7, and 8 (Figure 4.18) exhibit qualitatively different behavior from any of the others: the curves increase, at first, in a near-linear fashion like the others, but then suddenly flatten out and stop growing, indicating that the phase domain coarsening has stopped. The Sample 6 curve is the first to begin flattening out after approximately 13 hours, followed by Samples 7 and 8, which cease

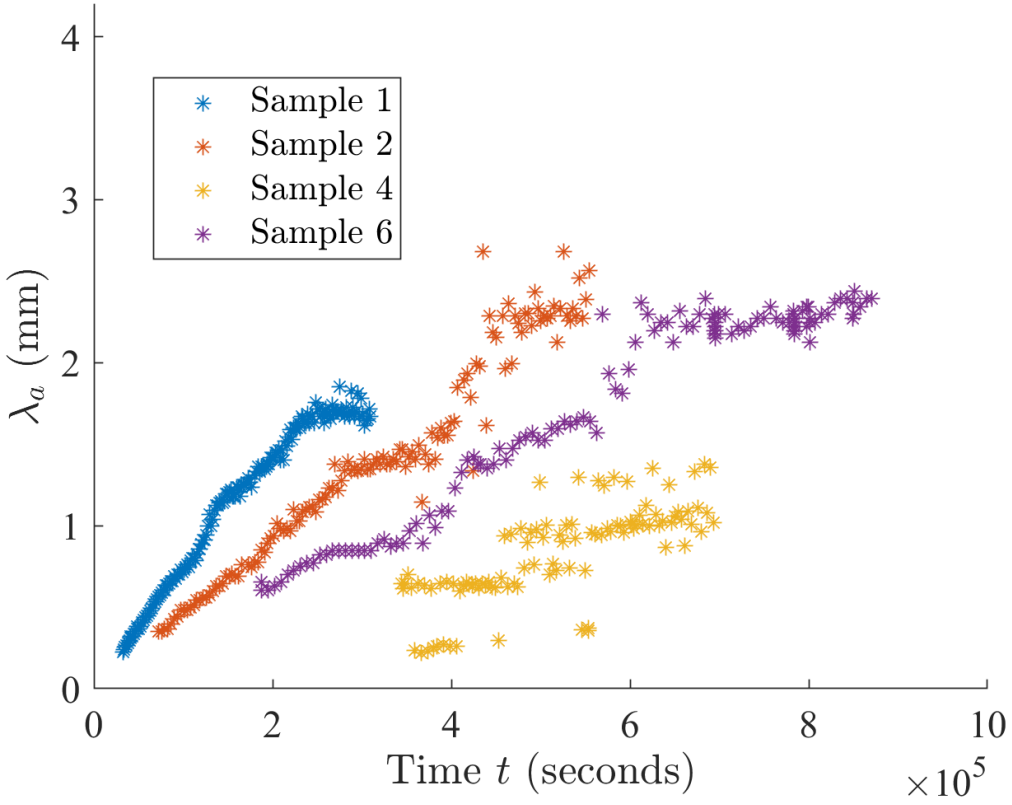

Figure 4.16 Characteristic domain length λ_a (in millimeters), plotted as a function of time t (in seconds), for BCAT-3 Samples 1, 2, 4, and 6. The values λ_a were obtained by running the algorithm described in Subsection 4.2.2 on the sample images from the NASA database. The legend indicates the sample number. The parameter values corresponding to each sample are listed in Table 4.1.

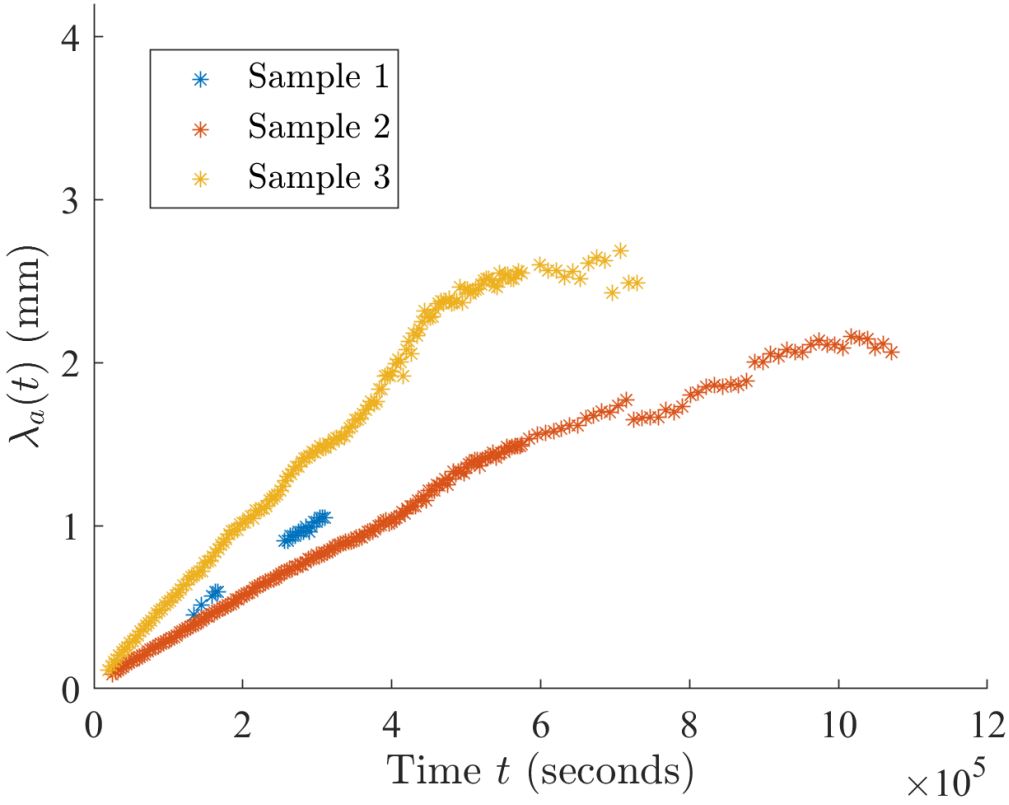

Figure 4.17 Characteristic domain length λ_a (in millimeters), plotted as a function of time t (in seconds), for BCAT-4 Samples 1, 2, and 3. The values λ_a were obtained by running the algorithm described in Subsection 4.2.2 on the sample images from the NASA database. The legend indicates the sample number. The parameter values corresponding to each sample are listed in Table 4.2.

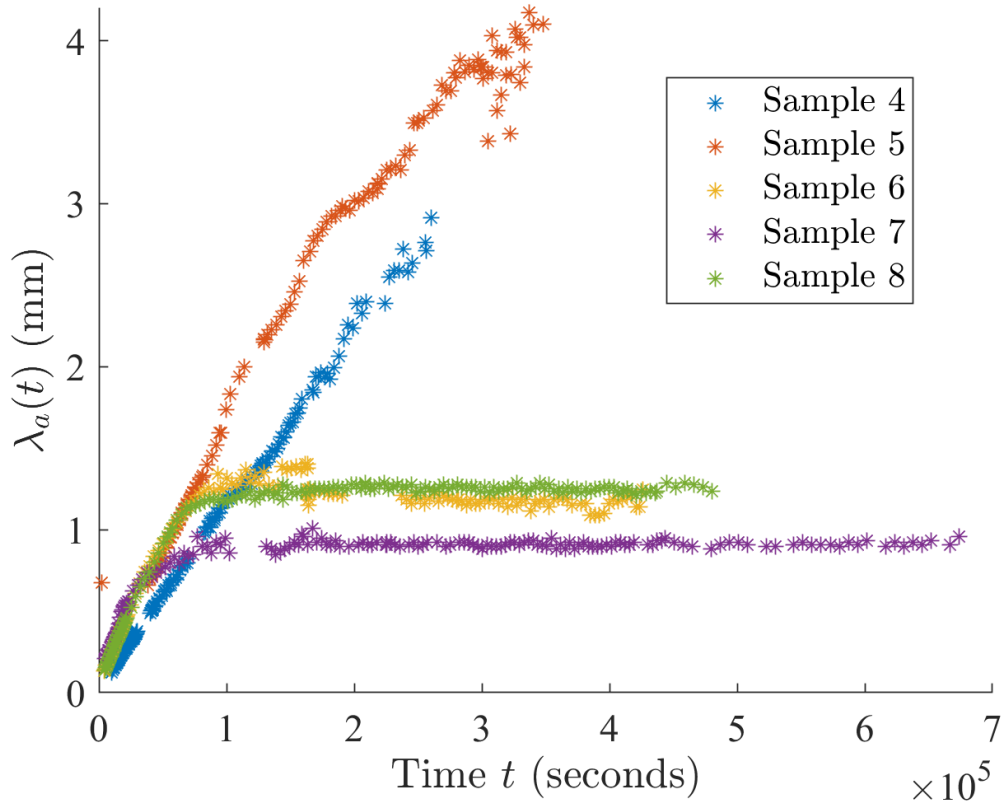

Figure 4.18 Characteristic domain length λ_a (in millimeters), plotted as a function of time t (in seconds), for BCAT-5 Samples 4, 5, 6, 7, and 8. The values λ_a were obtained by running the algorithm described in Subsection 4.2.2 on the sample images from the NASA database. The legend indicates the sample number. The parameter values corresponding to each sample are listed in Table 4.3.

to exhibit linear growth at around the same time ($t \approx 20$ hours.) These results are consistent with those of Sabin *et al.* [104], who reported the formation of crystallites having an arresting effect on the phase separation. A side-by-side comparison of our results with those of [104] is given in Figure 4.19, showing that the two compare favorably.

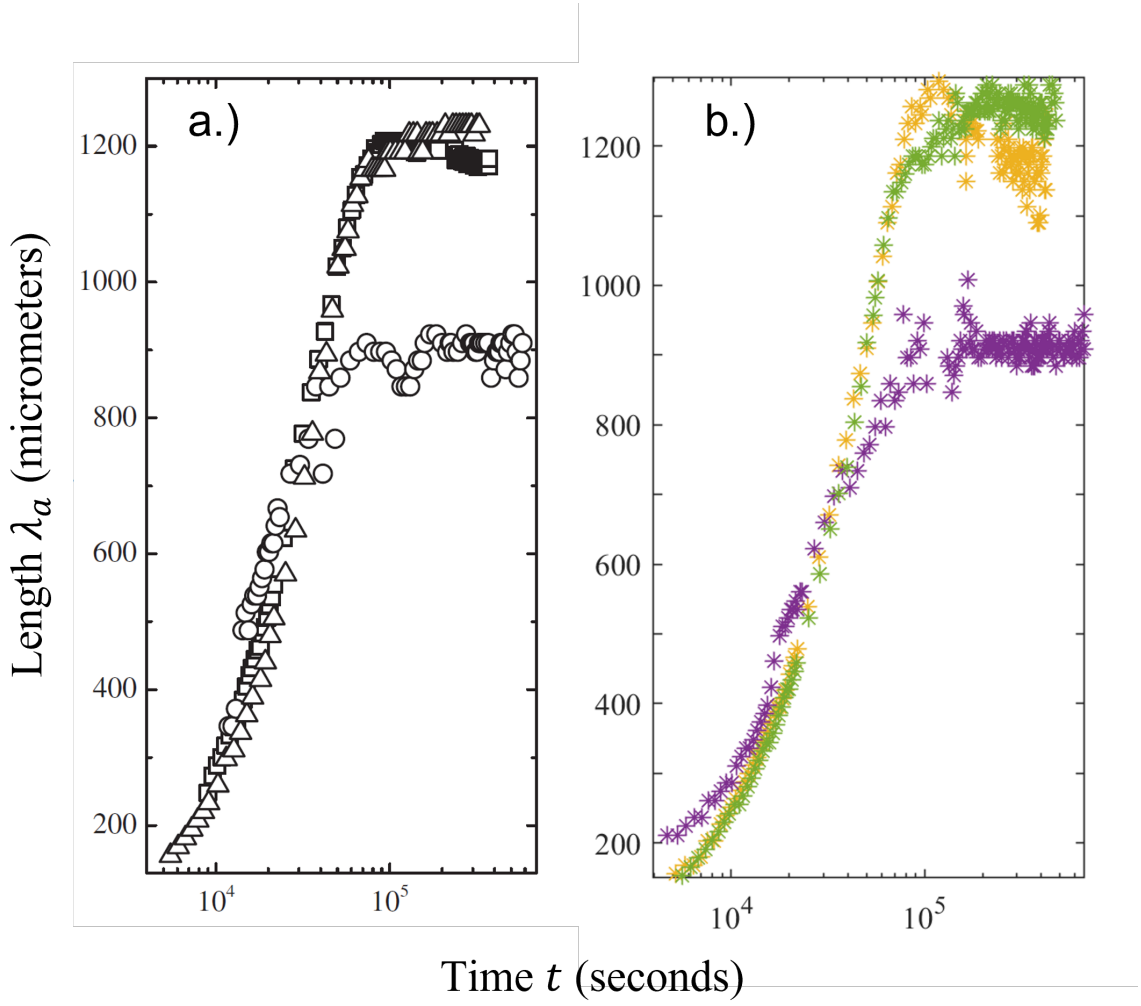

Figure 4.19 (a) Plot taken from [104], showing the characteristic domain length λ_a (in μm) for BCAT-5 Samples 6, 7, and 8. (b) Our plot of λ_a for BCAT-5 Samples 6, 7 and 8, plotted on a semilog scale and with the λ_a-axis in μm, to obtain a more direct comparison between our results and those of [104] in Panel (a).

At early times before the BCAT-5 Samples 6, 7 and 8 curves flatten out, the slopes of the curves are steeper than those of the BCAT-3 or BCAT-4 samples and

appear to be approximately the same as the slope of BCAT-5 Sample 5. Due to the eventual flattening of these three curves, their λ_a-values at very late times are smaller than any of the others, with two exceptions: 1) the final values are around the same as those of BCAT-3 Sample 4, and 2) BCAT-4 Sample 2 appears to still be growing but was "cut short" as there are no more data points after approximately 86 hours. It is evident that the low λ_a-values in BCAT-5 samples 6–8 is due to the fact that the autocorrelation curves flatten when the phase separation is arrested.

4.3 Model for Phase Separation in Colloid-Polymer Mixtures

As discussed in Section 4.1, the starting point for our model is the well-known Cahn-Hilliard equation for phase separation, which we then couple with the incompressible Stokes equations to incorporate effects of fluid flow. By itself, the Cahn-Hilliard equation does not account for hydrodynamic interactions. We begin this section by describing the Cahn-Hilliard equation in the specific form that describes our system, along with a linear stability analysis we conducted, in Subsection 4.3.1. We then describe the coupled Cahn-Hilliard-Stokes system in Subsection 4.3.2.

4.3.1 Cahn-Hilliard equation

The well-known Cahn-Hilliard equation is given by:

$$\phi_t = \nabla \cdot \left[\Gamma(\phi) \nabla \Big(\mu_c(\phi) - K \nabla^2 \phi \Big) \right] \tag{4.4}$$

where $\phi(\mathbf{x}, t)$ is the colloid volume fraction, Γ the mobility, $\sqrt{K}$ the length of the transition region between phase domains, and μ_c the colloid chemical potential.

The mobility $\Gamma(\phi)$ describes the extent to which the colloid particles are free to move about. We use the expression given by van Megen *et al.* [117], which was also used in a prior numerical study on crystallite growth in a colloidal suspension [70]:

$$\Gamma(\phi) = \begin{cases} \Gamma_0 \Big(1 - \dfrac{\phi}{0.57} \Big)^{2.6} & \text{if } \ \phi < 0.57 \\ 0 & \text{if } \ \phi \geq 0.57. \end{cases} \tag{4.5}$$

The factor Γ_0 is obtained from the Stokes-Einstein relation and has a value of $\Gamma_0 = 1/6\pi\eta_0 a$, where a is the colloid radius and η_0 the viscosity of the solvent in the absence of polymer. The critical value $\phi = 0.57$ is the value at which the glass transition occurs and the colloids are effectively no longer able to move freely [117]. Although negative values of ϕ have no physical meaning, (4.4) is a phase-field model and so it must be well-defined for *all* values of ϕ. Thus, for the purposes of our simulations, we have actually defined Γ to be

$$\Gamma(\phi) = \begin{cases} \Gamma_0 & \text{if } \phi \leq 0 \\ S_G(\phi) & \text{if } 0 < \phi \leq 0.01 \\ \Gamma_0\Big(1 - \dfrac{\phi}{0.57}\Big)^{2.6} & \text{if } 0.01 < \phi \leq 0.57 \\ 0 & \text{if } \phi > 0.57 \end{cases} \tag{4.6}$$

where $S_G(\phi)$ is a seventh-order polynomial spline interpolant for $\phi \in (0,\ 0.01]$, defined in such a way that Γ has three continuous derivatives. The "cutoff" value at which the spline interpolant begins is somewhat arbitrary; we chose it to be $\phi = 0.01$ in order to preserve the shape of (4.5) while simultaneously ensuring that the coefficients of the polynomial interpolant S_G are not problematically large. A plot of the mobility defined by (4.6) is shown in Figure 4.20.

The colloid chemical potential μ_c is proportional to the first derivative of the Helmholtz free energy function $f(\phi)$, which may be split into two parts: that of a pure colloid without polymer, and that of an ideal gas of polymer with a constant number density N_P [45, 74]. The function $f(\phi)$ has the form of a double (triple)-well potential for a system that admits two (three) equilibrium phases; the wells correspond to the ϕ-values of the different phases [45]. A plot of f and its corresponding μ_c, in the triple-well case, is shown in Figure 4.21(a).

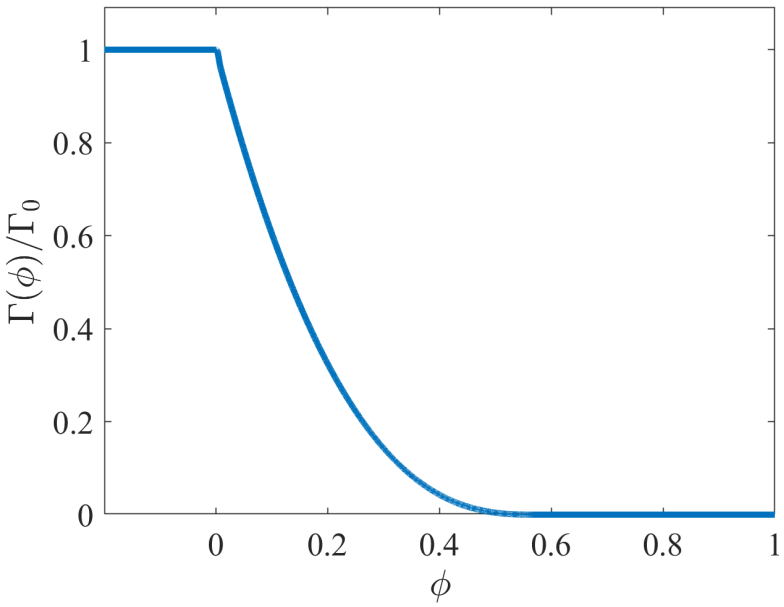

Figure 4.20 The mobility $\Gamma(\phi)$ as defined in (4.6), scaled by $\Gamma_0 = 1/6\pi\eta_0 a$. For $\phi \approx 0$, the low-ϕ "gas" phase, the (scaled) mobility Γ/Γ_0 is close to 1, and the colloids are free to move about. As ϕ increases, the mobility decreases until the glass transition takes place at $\phi = 0.57$, where Γ becomes zero and the colloids can no longer move at all.

Our expression for $\mu_c(\phi)$ is piecewise-defined, as follows:

$$\mu_c(\phi) = \begin{cases} \mathrm{S}_1(\phi) & \text{for } \phi \leq 0.01 \\ {\mu_c}^F(\phi) & \text{for } 0.01 < \phi \leq 0.495 \\ S_2(\phi) & \text{for } 0.495 < \phi < 0.54 \\ {\mu_c}^S(\phi) & \text{for } \phi \geq 0.54 \end{cases} \tag{4.7}$$

Here, the functions ${\mu_c}^F$ and ${\mu_c}^S$ are each valid only for ϕ-values in the *fluid* ($\phi \leq 0.495$) and *solid* ($\phi \geq 0.54$) phases, respectively. The functions $S_1(\phi)$ and $S_2(\phi)$ are spline interpolants: S_2 is a seventh-order polynomial defined so as to join ${\mu_c}^F$ and ${\mu_c}^S$ in such a way that μ_c is smooth and three times differentiable; S_1 is a fourth-order polynomial implemented in order to sidestep numerical issues with the logarithmic singularity in ${\mu_c}^F$ near $\phi = 0$ while preserving the qualitative behavior and three continuous derivatives. Each of the expressions ${\mu_c}^F$ and ${\mu_c}^S$ has the form [74]:

$${\mu_c}^X = k_B T \left(\int \frac{Z_X(\phi)}{\phi} d\phi + Z_X(\phi) - \frac{4}{3}\pi a^3 n_R \frac{d\alpha}{d\phi} \right) + \text{const} \tag{4.8}$$

where k_B is the Boltzmann constant, T the absolute temperature, $Z(\phi)$ the hard-sphere compressibility and $\alpha(\phi)$ the free volume fraction. The parameter n_R describes the polymer concentration within the free volume. We take it to be constant, an assumption that is equivalent to assuming the polymer chemical potential is constant [74]. The added constant term is simply an integration constant and does not influence the system's behavior.

Note that the only difference between the expressions for ${\mu_c}^F$ and ${\mu_c}^S$ in (4.8) is the hard-sphere compressibility, Z. The expression for $Z(\phi)$ in the fluid [24] and solid [107] phases will be denoted as $Z_F(\phi)$ and $Z_S(\phi)$, respectively; these are given by:

$$Z_F(\phi) = \frac{1 + \phi + \phi^2 - \phi^3}{(1-\phi)^3} \ , \qquad Z_S(\phi) = \frac{3}{1 - \phi/\phi_M} - A_2 \frac{\phi/\phi_M - B_2}{\phi/\phi_M - C_2} \tag{4.9}$$

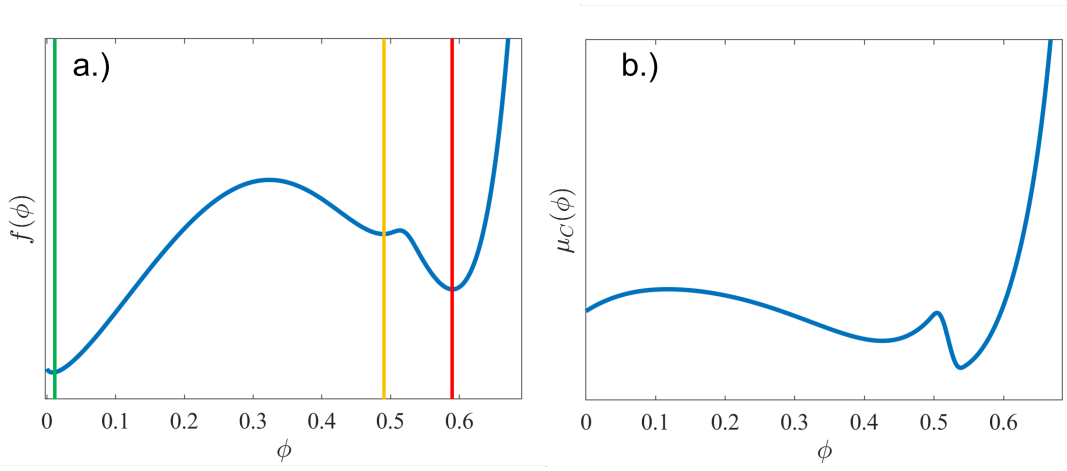

Figure 4.21 (a) The Helmholtz free energy f in the case of three-phase coexistence, plotted as a function of ϕ. The vertical lines corresponding to gas (green), liquid (yellow), and crystal (red) phases. The system parameters in this plot are $\phi_0 = 0.22$, $\rho = 0.80$ mg/mL, $a = 300$ nm, $\delta = 120$ nm. (b) The colloid chemical potential μ_c, which is proportional to the derivative of f, for the same parameter values as in Panel (a).

where $A_2 = 0.5935$, $B_2 = 0.7080$, $C_2 = 0.601$, and $\phi_M = \sqrt{2}\pi/6$ is the maximum value for ϕ, *i.e.,* when the colloid spheres are most efficiently packed.

The free-volume fraction $\alpha(\phi)$ from (4.8) describes the ratio of the "free" volume in which the polymer coils can move to the total volume of the system. The latter, of course, remains constant, but the free volume depends on ϕ. The ratio $\xi = \delta/a$, where δ is the radius of gyration of the polymer coils and a is the colloid radius, also enters into the expression for $\alpha(\phi)$ since the polymer coils are not permitted to move within a certain radius of a colloid particle due to the depletion zones [45, 90] as depicted in Figure 4.22. The expression for $\alpha(\phi)$ is [74]:

$$\alpha(\phi) = (1-\phi)e^{-A\frac{\phi}{1-\phi} - B(\frac{\phi}{1-\phi})^2 - C(\frac{\phi}{1-\phi})^3} \tag{4.10}$$

where $A = 3\xi + 3\xi^2 + \xi^3$, $B = 9\xi^2/2 + 3\xi^3$, and $C = 3\xi^3$. A plot of $\alpha(\phi)$ is shown in Figure 4.23.

The quantity n_R in Equation (4.8) should, in theory, be inversely proportional to the free volume fraction $\alpha(\phi)$ [74], specifically, $n_R = N_P/\alpha(\phi)V$, where N_P is the

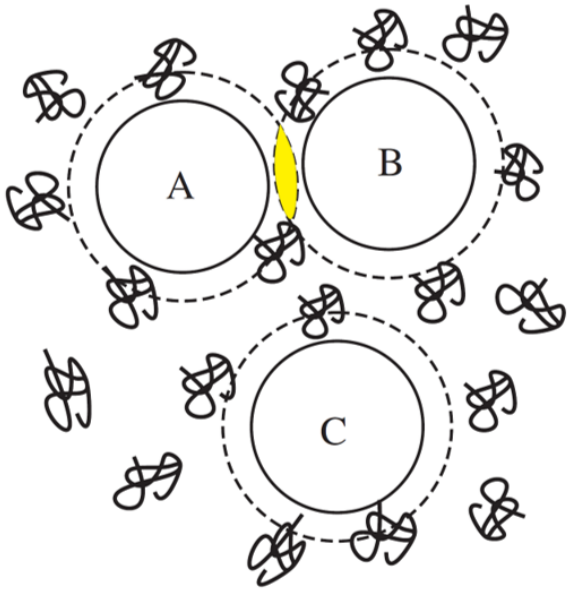

Figure 4.22 Schematic taken from [90], illustrating the depletion interactions that occur between the polymer coils and colloidal spheres. The circles A, B and C represent colloids, and the dotted circle around each colloid is the "depletion zone" inside of which the center of a polymer coil cannot pass; the thickness of these zones is approximately equal to the polymer coils' radius of gyration. When two colloids A and B are sufficiently close to one another so that their depletion zones overlap, no polymer can be present in the overlap region and a net osmotic force pushes the colloids closer together, thus acting as an attractive force between the colloids [90].

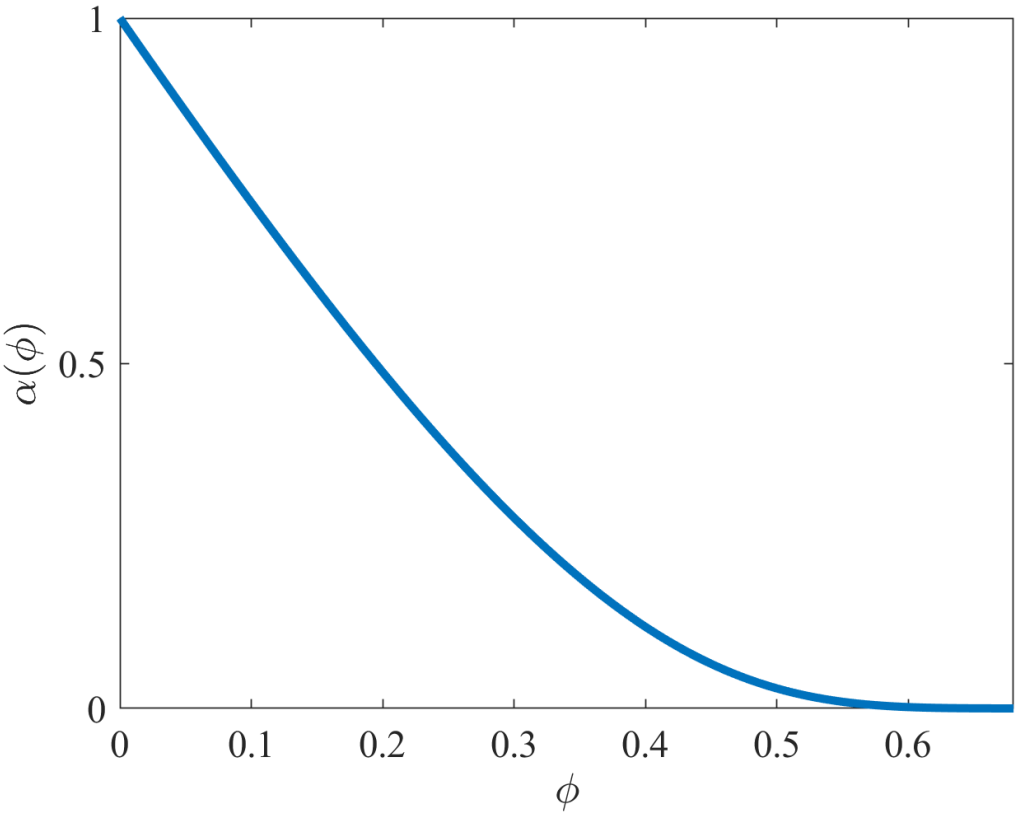

Figure 4.23 The free volume fraction $\alpha(\phi)$, as defined by (4.10), for the same parameters listed for Figure 4.21.

number of polymer coils in the system and V is the total volume of the system. We make an estimation of n_R, as discussed before, by taking it to be constant; we define $n_R = N_P/\alpha(\phi_0)V$, where ϕ_0 is the value of ϕ at the mixture's initial state when homogenized.

Linear stability analysis We now perform a linear stability analysis of the constant-density state $\phi = \phi_0$. To linearize the equation (4.4) about this base state ϕ_0, we plug in the ansatz:

$$\phi(\mathbf{x}, t) = \phi_0 + \epsilon\hat{\phi}e^{i(\mathbf{k}\cdot\mathbf{x})+\beta t} \tag{4.11}$$

where ϕ_0 and $\hat{\phi}$ are constants, $\mathbf{k} = [k_1,\ k_2]$ is the 2D wave vector, and $\mathbf{x} = [x,\ y]$ is the 2D position vector. Plugging (4.11) into (4.4) and Taylor expanding the function $\Gamma(\phi_0 + \epsilon\hat{\phi}e^{i(\mathbf{k}\cdot\mathbf{x})+\beta t}) = \Gamma(\phi_0) + \epsilon\hat{\phi}e^{i(\mathbf{k}\cdot\mathbf{x})+\beta t}\Gamma'(\phi_0) + O(\epsilon^2)$ (and similarly for ${\mu_c}'$), we drop all terms of $O(\epsilon^2)$ and higher to get:

$$\epsilon\beta\hat{\phi}e^{i(\mathbf{k}\cdot\mathbf{x})+\beta t} = \Gamma(\phi_0){\mu_c}'(\phi_0)\big(-\epsilon\hat{\phi}|\mathbf{k}|^2e^{i(\mathbf{k}\cdot\mathbf{x})+\beta t}\big) - \Gamma(\phi_0)K\epsilon\hat{\phi}|\mathbf{k}|^4e^{i(\mathbf{k}\cdot\mathbf{x})+\beta t} \tag{4.12}$$

We simplify this expression to arrive at the dispersion relation:

$$\beta = -\Gamma(\phi_0)|\mathbf{k}|^2\bigg(|\mathbf{k}|^2K + {\mu_c}'(\phi_0)\bigg). \tag{4.13}$$

In order for the solutions to be unstable, we need $\beta > 0$, *i.e.,* we can only have unstable solutions when $|\mathbf{k}| < \sqrt{-\frac{{\mu_c}'(\phi_0)}{K}}$, since Γ is always positive. For $K = 1$, we have:

$$\beta = -\Gamma(\phi_0)|\mathbf{k}|^2\bigg(|\mathbf{k}|^2 + {\mu_c}'(\phi_0)\bigg), \tag{4.14}$$

which can only be positive when ${\mu_c}'(\phi_0)$ is negative and $-{\mu_c}'(\phi_0) > |\mathbf{k}|^2$.

The linear stability analysis thus tells us that spinodal decomposition will only take place if the initial colloid volume fraction ϕ_0 of the homogeneous mixture is in

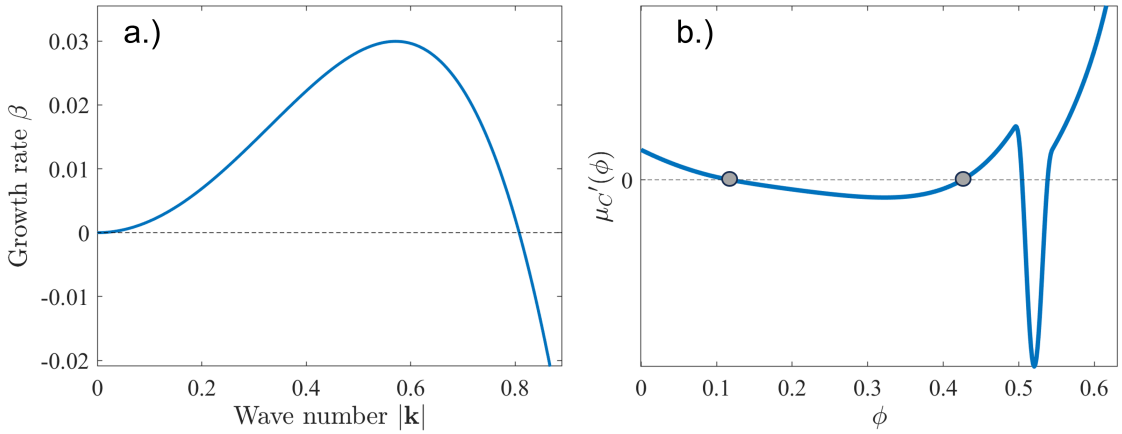

Figure 4.24 (a) The dispersion relation (4.14), in dimensionless variables, for the parameter values $\phi_0 = 0.22$, $\rho = 0.80$ mg/mL, $a = 300$ nm, and $\delta = 120$ nm. (b) Plot of the first derivative μ_c' of the colloid chemical potential, for the same parameters as in Panel (a). The region between the two gray dots is the spinodal region, where (4.15) is satisfied. We note that the small region to the right of the gray dots for which (4.15) is also satisfied is excluded from consideration, since the ϕ-values in this region are significantly higher than the homogenized "base state" values of ϕ_0 corresponding to any of the BCAT experiments.

the so-called "spinodal region," defined by the condition

$$\mu_c'(\phi_0) < 0. \tag{4.15}$$

Figure 4.24 shows a plot of μ_c' for a given set of system parameters, with the upper and lower bounds of the spinodal region indicated by gray dots. The small, higher-ϕ region to the right of the gray dots, for which (4.15) is also satisfied, will be excluded from consideration in this thesis since the ϕ-values in this region are significantly higher than the homogenized "base state" values of ϕ_0 corresponding to any of the BCAT experiments. We note also that this region is an artifact of the curvature of the spline function we used to interpolate between the expressions μ_c^F and μ_c^S for the fluid and solid phases, as given in (4.7).

4.3.2 Coupled system: Cahn-Hilliard equation with hydrodynamic interactions

By itself, (4.4) does not account for the hydrodynamic interactions that occur between colloid particles and the surrounding fluid: as spinodal decomposition takes place, the colloids exert stresses on surrounding fluid elements as they move around, generating a fluid flow. The colloids, in turn, are advected by this fluid flow. In order to account for these hydrodynamic interactions, we couple the Cahn-Hilliard equation with the incompressible Stokes equations, resulting in the system [62]

$$\begin{aligned} \phi_t + \mathbf{u}\cdot\nabla\phi &= \nabla\cdot\left[\Gamma(\phi)\nabla\Big(\mu_c(\phi) - K\nabla^2\phi\Big)\right], \\ \nabla\cdot\mathbf{u} &= 0, \\ \nabla\cdot\Big[\eta(\phi)\Big(\big(\nabla\mathbf{u}\big) + \big(\nabla\mathbf{u}\big)^T\Big)\Big] &= \nabla p + \kappa\frac{K}{V_c}\nabla\cdot\Big(\nabla\phi\nabla\phi - |\nabla\phi|^2\mathbf{I}\Big). \end{aligned} \tag{4.16}$$

Here, the expressions $\phi(\mathbf{x},t)$, $\Gamma(\phi)$, $\mu_c(\phi)$, and K are defined as before; $\mathbf{u}(\mathbf{x},t)$ denotes the fluid velocity, $p(\mathbf{x},t)$ the pressure, $V_c = 4\pi a^3/3$ the volume of a colloid particle, and $\eta(\phi)$ the dynamic viscosity of the fluid [60]:

$$\eta(\phi) = C_v e^{D_v\left(\frac{\phi}{\phi_m-\phi}\right)} \tag{4.17}$$

where $C_v = 1$, $D_v = 1.15$, and $\phi_m = 0.638$. Equation (4.17) was obtained by fitting to experimental data, as shown in Figure 4.25. This empirical formula describes the sharp increase in suspension viscosity as the colloid volume fraction increases. In Equation (4.16), the stress term on the right-hand side of the Stokes equation is the so-called Korteweg stress, which describes the stress exerted by the colloid particles on the fluid in a phase-field description [62]. For a homogeneous binary fluid in which each component species has the same molar mass, we would have $\kappa = 1$ [71]; however, in this work the solvent (typically *cis*-decalin or tetralin) and solute (colloid particles)

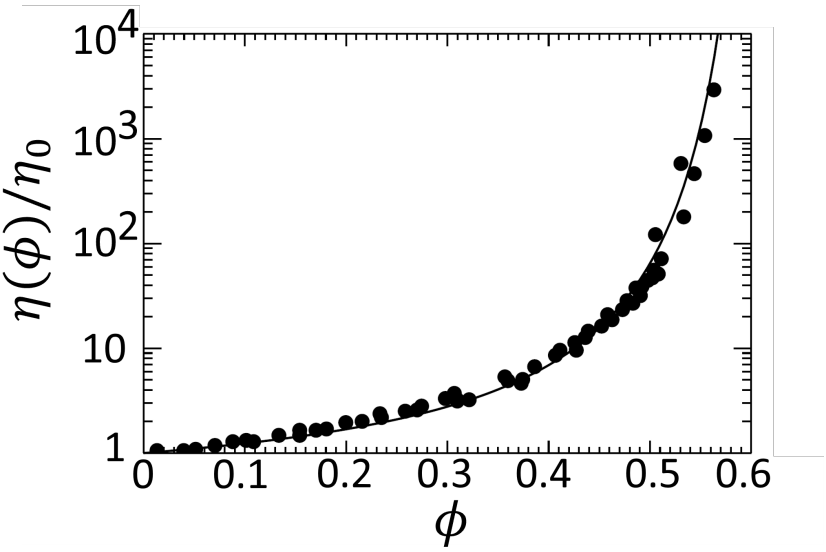

Figure 4.25 Scaled low shear viscosities at different ϕ for various colloidal suspensions of nearly monodisperse hard spheres, normalized by the viscosity η_0 of the pure solvent. The fit line is to Equation (4.17). Plot taken from [60].

have different molar masses, making it difficult to obtain a simple expression for the stress [72]. We thus take κ as a free parameter in our model.

Note that there are now *two* quantities we must solve for: we must first solve the second and third equations in (4.16) for $\mathbf{u}$, and then use that to solve the first equation in (4.16) for ϕ.

Non-dimensionalization To non-dimensionalize (4.16), we begin by considering the Cahn-Hilliard equation (4.4) *without fluid*, using the results of the linear stability analysis to inform the correct scales to use. Using Einstein's relation $\Gamma = D/k_BT$, where $D(\phi)$ is the diffusivity, k_B is the Boltzmann constant, and T is the absolute temperature of the system, (4.4) is equivalent to:

$$\phi_t = \nabla \cdot \left[\frac{1}{k_B T} D(\phi) \nabla \Big(\mu_c(\phi) - K \nabla^2 \phi \Big) \right]. \tag{4.18}$$

We begin by defining the dimensionless quantities:

$$\tilde{\mu}_c = \frac{\mu_c}{k_B T}, \quad \tilde{D} = \frac{D}{D_0}, \quad \tilde{\mathbf{x}} = \frac{\mathbf{x}}{L}, \quad \tilde{t} = \frac{t}{\tau} \tag{4.19}$$

where $D_0 = \Gamma_0 k_B T$ is a characteristic diffusivity constant and L and τ are length and time scales, respectively, to be determined. We also assign K the value $K = k_B T \ell^2$, where ℓ is a length parameter to be determined. Plugging these definitions into (4.18) and canceling factors, we get

$$\frac{1}{\tau}\phi_{\tilde{t}} = \frac{1}{L^2}\nabla \cdot \left[D_0 \tilde{D}(\phi_D)|\tilde{\mu}_c'(\phi_{sc})| \frac{\tilde{D}(\phi)}{\tilde{D}(\phi_D)} \nabla \left(\frac{\tilde{\mu}_c(\phi)}{|\tilde{\mu}_c'(\phi_{sc})|} - \frac{\ell^2}{|\tilde{\mu}_c'(\phi_{sc})|L^2}\nabla^2 \phi \right) \right], \quad (4.20)$$

where ∇ now denotes the derivative with respect to the dimensionless spatial coordinate $\tilde{\mathbf{x}}$. Note that we have multiplied and divided in the right-hand side by $|\tilde{\mu}_c'(\phi_{sc})|$, which is a characteristic value of the derivative of the chemical potential, and by $\tilde{D}(\phi_D)$, a characteristic value of the diffusivity. To get factors to cancel, we thus choose the length and time scaling factors L and τ to be

$$L = \frac{\ell}{\sqrt{|\tilde{\mu}_c'(\phi_{sc})|}}, \quad \tau = \frac{\ell^2}{|\tilde{\mu}_c'(\phi_{sc})|^2 D_0 \tilde{D}(\phi_D)}. \quad (4.21)$$

Plugging in these definitions, we arrive at the dimensionless equation

$$\phi_{\tilde{t}} = \nabla \cdot \left[\frac{\tilde{D}(\phi)}{\tilde{D}(\phi_D)} \left(\frac{\tilde{\mu}_c'(\phi)}{|\tilde{\mu}_c'(\phi_{sc})|} - \nabla^2 \right) \nabla \phi \right] \quad (4.22)$$

To gain an understanding of the correct scales to use, we recall the result (4.14) from our linear stability analysis, which can be straightforwardly repeated for the dimensionless equation (4.22) to obtain the dimensionless growth rate

$$\sigma = \frac{\tilde{D}(\phi_0)}{\tilde{D}(\phi_D)} \left(- \frac{\tilde{\mu}_c'(\phi_0)}{|\tilde{\mu}_c'(\phi_{sc})|} |\mathbf{k}|^2 - |\mathbf{k}|^4 \right). \quad (4.23)$$

Assuming $\tilde{\mu}_c'(\phi_0) < 0$, *i.e.,* that the base state ϕ_0 is in the spinodal region, the wavenumber of maximum growth, k^*, and its growth rate, σ^*, are given by

$$k^* = \sqrt{\frac{|\tilde{\mu}_c'|}{2|\tilde{\mu}_c'(\phi_{sc})|}}, \quad \sigma^* = \frac{\tilde{D}}{\tilde{D}(\phi_D)} \left(\frac{|\tilde{\mu}_c'|}{2|\tilde{\mu}_c'(\phi_{sc})|} \right)^2. \quad (4.24)$$

For convenience we choose to define:

$$|\tilde{\mu}_c'(\phi_{sc})| = \max_{\phi \in spinodal} \big(|\tilde{\mu}_c'(\phi)|\big), \quad \phi_{sc} = \text{argmax}\Big(|\tilde{\mu}_c'(\phi)| : \quad \tilde{\mu}_c'(\phi) < 0\Big),$$
$$\tilde{D}(\phi_D) = \max\big(\tilde{D}(\phi)\big) = \tilde{D}(0), \quad \phi_D = \text{argmax}\ \tilde{D}(\phi) = 0,$$

and thus, k^* and σ^* are bounded above by $1/\sqrt{2}$ and $1/4$, respectively. Since $\tilde{D}(0) = 1$ for the expression for the mobility in Equation (4.6), we omit the $\tilde{D}(\phi_D)$ for the rest of this discussion.

We now turn our attention to the full model, (4.16), using the same scalings derived above. For the fluid velocity $\mathbf{u}$, we define the scaling to be $\tilde{\mathbf{u}} = \mathbf{u}/U$, with the scaling factor U to be determined. For the fluid viscosity $\eta(\phi)$, we define $\tilde{\eta} = \eta/\eta_0$, where η_0 is the viscosity of the solvent alone [12]. For now, we denote the scaling factor for the pressure as P_0, but we note that this factor will not appear in the finalized model because the pressure term will disappear due to the incompressibility condition in our formulation. Following the same procedure as in obtaining (4.22) and defining the velocity scaling factor

$$U = \frac{\kappa k_B T \ell^2}{\eta_0 V_c L}, \tag{4.25}$$

we end up with the dimensionless system

$$\begin{aligned} \phi_{\tilde{t}} + \gamma \tilde{\mathbf{u}} \cdot \nabla \phi &= \nabla \cdot \left[\tilde{D}(\phi) \nabla \left(\frac{\tilde{\mu}_c(\phi)}{|\tilde{\mu}_c'(\phi_{sc})|} - \nabla^2 \phi \right) \right], \\ \nabla \cdot \tilde{\mathbf{u}} &= 0, \\ \nabla \cdot \Big[\tilde{\eta}(\phi) \boldsymbol{\tau} \Big] &= \frac{P_0 L}{U \eta_0} \nabla \tilde{p} + \nabla \cdot \boldsymbol{\sigma} \end{aligned} \tag{4.26}$$

where we have defined the rate of strain tensor $\boldsymbol{\tau} = \big(\nabla \mathbf{u}\big) + \big(\nabla \mathbf{u}\big)^T$ and Korteweg stress $\boldsymbol{\sigma} = \nabla\phi\nabla\phi - |\nabla\phi|^2 \mathbf{I}$ for convenience. The Peclet number

$$\gamma = \frac{U\tau}{L} = \frac{9\kappa}{2|\tilde{\mu}_c'(\phi_{sc})|} \cdot \left(\frac{l}{a}\right)^2 \tag{4.27}$$

is a dimensionless parameter that describes the relative importance of advective and diffusive transport of the colloid particles.

4.3.3 Numerical implementation

We seek a numerical scheme to solve the dimensionless system

$$\begin{aligned} \phi_t + \gamma \mathbf{u} \cdot \nabla \phi &= \nabla \cdot \left[D(\phi) \nabla \Big(\mu_c(\phi) - \nabla^2 \phi \Big) \right] \\ \nabla \cdot \mathbf{u} &= 0 \\ \nabla \cdot \Big[\eta(\phi) \boldsymbol{\tau} \Big] &= \nabla p + \nabla \cdot \boldsymbol{\sigma}, \end{aligned} \tag{4.28}$$

where we have dropped the tildes and re-defined $D(\phi) := \tilde{D}(\phi)/\tilde{D}(\phi_D)$ and $\mu_c(\phi) := \tilde{\mu}_c(\phi)/|\tilde{\mu}_c'(\phi_{sc})|$ for convenience; note that we have also omitted the prefactor $\frac{P_0 L}{U \eta_0}$ in front of the pressure term ∇p, as it is inconsequential because the following formulation will cause this term to vanish.

We solve the system (4.28) on a square 512×512 spatial grid with periodic boundary conditions. The domain size is $4\pi P \times 4\pi P$, where where we typically take $P = 20$ unless otherwise stated. We make this choice because our linear stability analysis yields an upper bound $k^* = 1/\sqrt{2}$ for the wavenumber of maximum growth for ϕ_0 in the spinodal region, as per Equation (4.24). This corresponds to a wavevector with components $k_x = k_y = 1/2$, for example. Our choice of simulation domain size admits P such wavelengths in the x and y directions.

To imitate the initially homogenized "base state" of the suspension immediately after mixing, we generate a two-dimensional matrix of small, random (but smooth) Gaussian perturbations in MATLAB and add it to the base state colloid volume fraction ϕ_0. When ϕ_0 satisfies (4.15) (*i.e.,* is in the spinodal region), these small-amplitude perturbations will grow in time and spinodal decomposition will take place.

Cahn-Hilliard equation with advective term To solve the first equation in (4.28), we implement a numerical scheme that is semi-implicit in time and pseudo-spectral in space. The first-order forward Euler method for this equation, written in Fourier space, is:

$$\hat{\phi}^{n+1} = \hat{\phi}^n - \gamma \Delta t \mathcal{F}\Big[\mathbf{u} \cdot \nabla \phi\Big] + \Delta t i \mathbf{k} \cdot \mathcal{F}\Bigg[D(\phi)\mathcal{F}^{-1}\Big[i\mathbf{k}\Big(\mathcal{F}\big[\mu_c(\phi)\big] + |\mathbf{k}|^2 \hat{\phi}\Big)\Big]\Bigg] \quad (4.29)$$

where Δt is the time step size, $\mathbf{k}$ is the two-dimensional wave vector $\mathbf{k} = [k_1,\ k_2]$, and the hats are used to denote Fourier-transformed variables, $\hat{\phi} = \mathcal{F}[\phi]$.

Unfortunately, (4.29) has a severe time-stepping restriction, $\Delta t \sim O((\Delta x)^4)$. To avoid this problem, Zhu *et al.* [120] propose a semi-implicit time-stepping scheme. Specifically, they add and subtract a constant A from the diffusivity function:

$$D(\phi) = \big(D(\phi) - A\big) + A, \quad (4.30)$$

which results in a linear term $-A\Delta t|\mathbf{k}|^4\hat{\phi}$ on the right-hand side. This term is treated implicitly, while all of the other, nonlinear terms are treated explicitly. The constant A is chosen to satisfy the condition $|D(\phi) - A| \leq A$. Zhu *et al.* suggested $A = \frac{1}{2}\big(\max(D(\phi)) + \min(D(\phi))\big)$, but we found by experimenting with the numerical scheme that $A = 1$ is a suitable choice for the mobility defined in Equation (4.6).

Rearranging the resulting equation, we obtain

$$\hat{\phi}^{n+1} = \hat{\phi}^n - \frac{\Delta t}{1 + A\Delta t|\mathbf{k}|^4}\Bigg(\gamma\mathcal{F}\Big[\mathbf{u}^n \cdot \nabla\phi^n\Big] - i\mathbf{k} \cdot \mathcal{F}\Bigg[D(\phi^n)\mathcal{F}^{-1}\Big[i\mathbf{k}\Big(\mathcal{F}\big[\mu_c(\phi^n)\big] + |\mathbf{k}|^2\hat{\phi}^n\Big)\Big]\Bigg]\Bigg). \quad (4.31)$$

To verify that we are getting first-order convergence in time, we plotted the relative error $\|\phi - \phi_{ex}\|_{L^2}/\|\phi_{ex}\|_{L^2}$ as a function of the time step size at time $t = 10$, taking our "exact" solution ϕ_{ex} to be the result of running our simulation with a time step

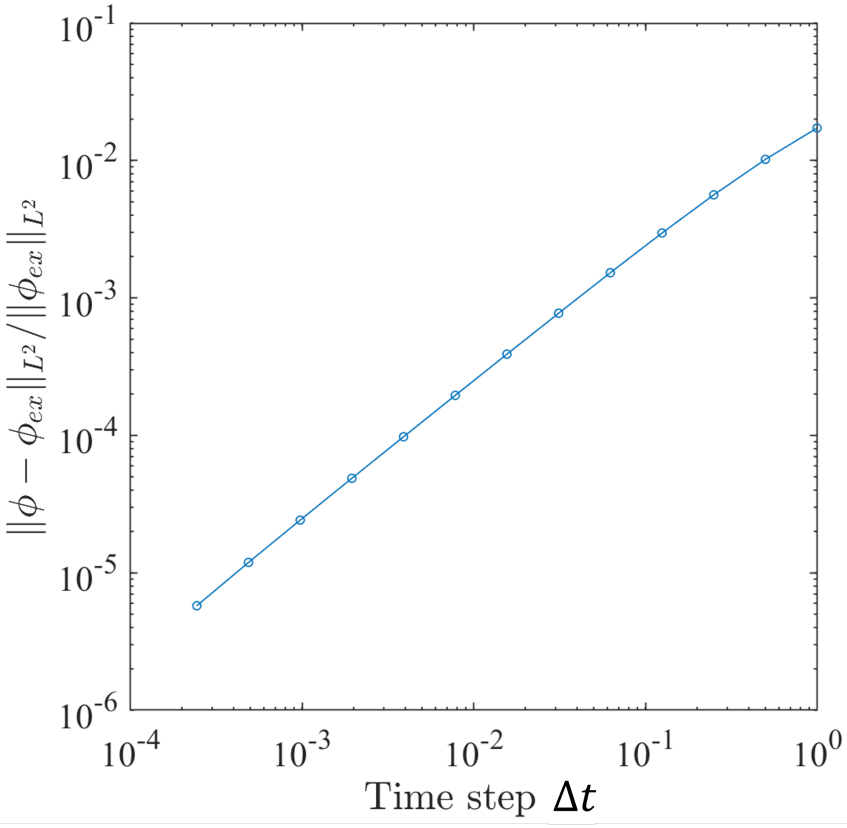

Figure 4.26 Time convergence plot for the semi-implicit scheme (4.31). The vertical axis values are the relative errors $\|\phi - \phi_{ex}\|_{L^2}/\|\phi_{ex}\|_{L^2}$ in the solution ϕ at $t = 10$, as obtained using the time step size Δt (horizontal axis.) We took the "exact" solution ϕ_{ex} to be the solution at $t = 10$ when using $\Delta t = 2^{-16}$. For this plot, we used the parameters corresponding to BCAT-5 Sample 4, without hydrodynamic effects ($\gamma = 0$.)

size of $\Delta t = 2^{-16}$. Figure 4.26 shows a log-log plot of this; we measured the slope to be approximately 1, as desired.

In the case $\gamma = 0$, *i.e.,* when no hydrodynamic effects are taken into account, the advective term $\gamma \mathbf{u} \cdot \nabla \phi$ in (4.31) disappears and there is no need to solve for $\mathbf{u}$. For $\gamma > 0$, we must solve the incompressible Stokes equations, *i.e.,* the last two equations in (4.28), to obtain $\mathbf{u}$ before we can solve for ϕ. The algorithm for solving the incompressible Stokes equations for $\mathbf{u}$ at any given time step n is detailed below.

Incompressible Stokes equations Following Tree *et al.* [114], we write

$$\eta(\phi) = \eta^* + \bar{\eta}(\phi), \quad \eta^* = \max(\eta(\phi)) = \text{constant}. \tag{4.32}$$

Plugging this definition in for η, we rewrite the last equation in (4.28) as

$$\eta^* \nabla^2 \mathbf{u} = \nabla p - \nabla \cdot \big[\bar{\eta}\boldsymbol{\tau}\big] + \nabla \cdot \boldsymbol{\sigma}. \tag{4.33}$$

Taking the Fourier transform of (4.33) we obtain

$$-\eta^* |\mathbf{k}|^2 \hat{\mathbf{u}} = i\mathbf{k}\hat{p} + i\mathbf{k} \cdot \bigg[- \mathcal{F}\big[\bar{\eta}\boldsymbol{\tau}\big] + \mathcal{F}\big[\boldsymbol{\sigma}\big]\bigg] \tag{4.34}$$

and then applying $\mathbf{k}\cdot$ to both sides, we get:

$$-\eta^* |\mathbf{k}|^2 \mathbf{k} \cdot \hat{\mathbf{u}} = i|\mathbf{k}|^2 \hat{p} + \mathbf{k} \cdot \bigg(i\mathbf{k} \cdot \bigg[- \mathcal{F}\big[\bar{\eta}\boldsymbol{\tau}\big] + \mathcal{F}\big[\boldsymbol{\sigma}\big]\bigg]\bigg). \tag{4.35}$$

The term on the left-hand side vanishes since the incompressibility condition $\nabla \cdot \mathbf{u} = 0$ in Fourier space becomes $i\mathbf{k} \cdot \hat{\mathbf{u}} = 0$. Solving for $\hat{p}$, we obtain

$$\hat{p} = \frac{i\mathbf{k}}{|\mathbf{k}|^2} \cdot \bigg(i\mathbf{k} \cdot \bigg[- \mathcal{F}\big[\bar{\eta}\boldsymbol{\tau}\big] + \mathcal{F}\big[\boldsymbol{\sigma}\big]\bigg]\bigg) \tag{4.36}$$

and then plug this identity into (4.34) to get

$$-\eta^* |\mathbf{k}|^2 \hat{\mathbf{u}} = \Big(\mathbf{I} - \frac{\mathbf{k}\mathbf{k}^T}{|\mathbf{k}|^2}\Big)\Big[i\mathbf{k} \cdot \Big(- \mathcal{F}\big[\bar{\eta}\boldsymbol{\tau}\big] + \mathcal{F}\big[\boldsymbol{\sigma}\big]\Big)\Big].$$

At last, we solve for $\hat{\mathbf{u}}$, which gives us:

$$\hat{\mathbf{u}} = -\frac{1}{\eta^* |\mathbf{k}|^2}\Big(\mathbf{I} - \frac{\mathbf{k}\mathbf{k}^T}{|\mathbf{k}|^2}\Big)\Big[i\mathbf{k} \cdot \Big(- \mathcal{F}\big[\bar{\eta}\boldsymbol{\tau}\big] + \mathcal{F}\big[\boldsymbol{\sigma}\big]\Big)\Big]. \tag{4.37}$$

Denoting $\hat{\mathbf{u}} = [\hat{u}_1,\ \hat{u}_2]$, the incompressibility condition yields the identity $\hat{u}_2 = -\frac{k_1}{k_2}\hat{u}_1$. This allows us to rewrite (4.37) in terms of only one component of $\mathbf{u}$, which in essence reduces (4.37) to a scalar equation. We thus define a scalar $\hat{u}$ such that:

$$\hat{\mathbf{u}} = \frac{i\mathbf{k}^\perp}{|\mathbf{k}|}\hat{u}, \tag{4.38}$$

where $\mathbf{k}^{\perp} = [k_2,\ -k_1]$. Substituting (4.38) into (4.37) and using the identity

$$\mathbf{I} - \frac{\mathbf{k}\mathbf{k}^T}{|\mathbf{k}|^2} = \frac{\mathbf{k}^{\perp}\mathbf{k}^{\perp T}}{|\mathbf{k}|^2} \tag{4.39}$$

to simplify the right-hand side, we then solve for $\hat{u}$ on the left-hand side to get

$$\hat{u} = \frac{i}{\eta^* |\mathbf{k}|^3} \mathbf{k}^{\perp} \cdot \Big[i\mathbf{k} \cdot \Big(-\mathcal{F}\big[\tilde{\eta}\boldsymbol{\tau}\big] + \mathcal{F}\big[\boldsymbol{\sigma}\big] \Big) \Big]. \tag{4.40}$$

Note that (4.40) must be solved iteratively for $\hat{u}$ because

$$\boldsymbol{\tau} = \nabla\mathbf{u} + \big(\nabla\mathbf{u}\big)^T = \nabla\left(\mathcal{F}^{-1}\left[\frac{i\mathbf{k}^{\perp}}{|\mathbf{k}|}\hat{u}\right]\right) + \left(\nabla\left(\mathcal{F}^{-1}\left[\frac{i\mathbf{k}^{\perp}}{|\mathbf{k}|}\hat{u}\right]\right)\right)^T, \tag{4.41}$$

so $\hat{u}$ appears on both sides of the equation. We use a fixed-point method called Anderson mixing [80, 111], described below, but we iterate in *real space* and so we must compute the inverse Fourier transform of (4.40) before performing the Anderson mixing. To this end, we will use u to denote the real-space analog of our scalar $\hat{u}$, and $H_R(u)$ will denote the real-valued inverse Fourier transform of the right-hand side of (4.40).

As can be seen in the discussion below, Anderson mixing requires a startup scheme, for which we will use Picard iteration with relaxation [111]. For all time steps n except the very first, we use the previous time step's u as our initial guess ${u_0}^n$. For the first time step, our ${u_0}^0$ is found by solving the constant-viscosity Stokes equation:

$$\eta\nabla^2\mathbf{u} = \nabla p + \nabla\cdot\boldsymbol{\sigma}. \tag{4.42}$$

Fourier-transforming (4.42) and expressing it in terms of our scalar $\hat{u}$, we get:

$$\hat{u} = \frac{1}{\eta|\mathbf{k}|^3} i\mathbf{k}^{\perp} \cdot \Big(i\mathbf{k} \cdot \mathcal{F}[\boldsymbol{\sigma}] \Big), \tag{4.43}$$

which can be solved directly for $\hat{u}$; we then compute the inverse Fourier transform of $\hat{u}$ and use the result as our initial guess, ${u_0}^0$. Note that, at early times, (4.43)

is a relatively good approximation since the phase separation has not yet progressed enough to cause significant spatial variation in $\eta(\phi)$.

Anderson Mixing We begin by writing the inverse Fourier transform of Equation (4.40) as

$$u = H_R(u), \tag{4.44}$$

where H_R is a linear (affine) operator. Since the discretized version of u is large, typically consisting of 512^2 unknowns on a two-dimensional domain, it is not feasible to solve Equation (4.44) explicitly using Gaussian elimination, for example. For this reason, we choose to use an iterative scheme called Anderson mixing, which has been described in prior literature [80, 111]:

$$u_{k+1} = H_R(\bar{u}_{k+1}), \quad \text{where} \;\; \bar{u}_{k+1} = u_k + \sum_j c_j\big(u_{k-j} - u_k\big). \tag{4.45}$$

The constants c_j are obtained by solving for the vector $\mathbf{c}$ in the linear system

$$U\mathbf{c} = \mathbf{v}, \tag{4.46}$$

where U is an $I \times J$ matrix, with $I = J \geq 2$, and $\mathbf{v}$ and $\mathbf{c}$ are vectors of length J. Defining the inner product $(f, g) = \int f(\mathbf{x})g(\mathbf{x})\, d\mathbf{x}$, the elements of U and $\mathbf{v}$ are:

$$U_{ij} = (d_k - d_{k-i}, d_k - d_{k-j}), \quad v_i = (d_k - d_{k-i}, d_k) \tag{4.47}$$

where $d_k := H_R(u_k) - u_k$.

The dimension J of our linear system (4.46) can be chosen as follows; note that for any $k \geq J$, computing our $(k+1)$th iterate u_{k+1} requires $J+1$ previous iterates u_k, u_{k-1}, ..., u_{k-J}. As a startup scheme to obtain the first J iterates u_1, u_2, ..., u_J (recall that u_0 is known), we use Picard iteration with relaxation:

$$u_{k+1} = \omega H_R(u_k) + (1-\omega)u_k, \quad 0 \leq k < J, \tag{4.48}$$

choosing our relaxation parameter to be $\omega = 1/10$.

The error residual for the fixed-point problem (4.44) is computed in real space and measured in the L^2-norm. Specifically, when computing the scalar u^n to recover $\mathbf{u}^n$ at the nth time step t_n, the error residual for the kth iterate of Anderson mixing is defined as

$$E_k^n = \|H_R(u_k^n) - u_k^n\|_{L^2}. \tag{4.49}$$

Convergence of our Anderson mixing algorithm is achieved when $E_k^n \leq e_{tol}$, where $e_{tol} = 10^{-6}$ is our desired error tolerance.

In our numerical experiments, we found that if the linear system could not be solved for $J = 2$, increasing J to 3 sometimes allowed for it to be solved. Similarly, if $J = 3$ failed, we could often solve it if we set $J = 4$. Unfortunately, the larger J is, the more startup iterates (and the more Picard iterations) are needed. In practice, we have found that choosing $J = 2$ for early times t (when the constant-η solution u_0 is fairly accurate) yields fast convergence. As the phase domain coarsening progresses and η is no longer nearly constant, our Anderson mixing code adapts by increasing the dimension J of our linear system and starting over for that time step if convergence is not reached within a certain number of iterations k_{max}^J or if the error residual E_k^n is above a prescribed threshold E^{max}. Note that we include the Picard (startup) iterations when defining k_{max}. Our numerical experiments proved $E^{max} = 100$ to be a suitable value for this threshold. The maximum allowed number of iterations k_{max}^J depends on the dimension J of the system being used; for $J = 2$, we set it to $k_{max}^J = 40$, and increase it by 10 for successive values of J:

$$k_{max}^J = 40 + 10(J - 2), \qquad J \geq 2. \tag{4.50}$$

The reason for this is that the system tends to take more iterations as the phase separation progresses, especially as we increase J and the number of startup Picard iterations is thus also increased.

4.4 Simulation Results

We ran simulations of our model (4.28) with parameter values corresponding to those of the BCAT experiments (refer to Tables 4.1, 4.2, and 4.3), with a goal of comparing our simulation results with the experimental data in Subsection 4.2.2. As stated in Subsection 4.3.3, we use periodic boundary conditions in the simulations. Our dimensionless domain size is $4\pi P \times 4\pi P$ with $P = 20$, we use $N = 512$ Fourier modes in each direction, and our time step size is $\Delta t = 2^{-6}$, unless otherwise specified.

For each BCAT sample, we ran simulations both with hydrodynamic interactions ($\gamma > 0$) and without ($\gamma = 0$) in order to gain an understanding of the role that these effects play in the phase separation process. In Subsection 4.4.1, we present plots of our simulation results and discuss some of the qualitative features of our model that we can observe by simply looking at these outputs. In Subsection 4.4.2, we show the results of implementing on our simulation results the phase domain growth characterization algorithm described in Subsection 4.2.2, which we used on the NASA images. We also detail verification steps we undertook to validate our simulation and phase domain growth algorithms. We then compare the resulting simulation data with the NASA image data.

4.4.1 Qualitative behavior in simulation outputs

We find that our simulations exhibit some behaviors that have been predicted theoretically in prior work [45] and observed experimentally [61, 91]. For example, the plots of the colloid volume fraction ϕ for BCAT-5 Sample 7, which are shown in the left column of Figure 4.27, exhibit a three-phase coexistence of solid, gas, and a metastable liquid phase. This simulation was done with $\gamma = 50$, thus including

hydrodynamic effects; we also ran a simulation without hydrodynamic effects ($\gamma = 0$) in which we observed the same three-phase coexistence (Figure 4.28).

The column on the left in Figure 4.27 shows the colloid volume fraction ϕ for four different (dimensionless) times $t = 0$, 100, 500, and 5000: at $t = 0$, the mixture is nearly homogeneous at the base state value $\phi_0 = 0.29$, with only small perturbations present. By $t = 100$, small domains of low-ϕ "gas" phase (dark blue) have formed; higher-ϕ (lighter green) regions also become visible. The phase domains continue to grow, and the higher-ϕ "liquid" (orange) values take over, forming the background as the low-ϕ "droplets" merge together to form larger gas domains. This liquid state, however, is temporary, as it is only a metastable state. Eventually, crystallization sets in and there is a three-phase coexistence of solid, liquid, and gas. By $t = 5000$, the solid phase has mostly taken over, though small regions of the liquid phase remain. The gas phase "droplets" continue to merge, and coarsening progresses.

Each plot in the center column of Figures 4.27 and 4.29 shows the (dimensionless) fluid speed $|\gamma \mathbf{u}|$ on the spatial domain at the same time t as the corresponding ϕ-plot in the left column. The initial gradients in ϕ are small, so the initial fluid speeds are initially small. The fluid speeds increase quickly thereafter, and are largest for early times (*e.g.,* $t = 100$), slowing down at later times (*e.g.,* $t = 500$ and 1000).

We have made several interesting observations about the behavior of our model. One of these observations is that including hydrodynamic interactions between the colloid particles and the surrounding fluid in the model seems to make the phase domains rounder in shape. This effect was more prominent in some samples than in others. For example BCAT-5 Sample 4 illustrates this phenomenon: the phase domains shown in the left column of Figure 4.29 (where we set $\gamma = 50$), especially at late times, appear more circular than those in Figure 4.30, for which hydrodynamic effects were not incorporated ($\gamma = 0$). This finding is somewhat at odds with the results of Furukawa and Tanaka [50], who conducted simulations of colloids interacting

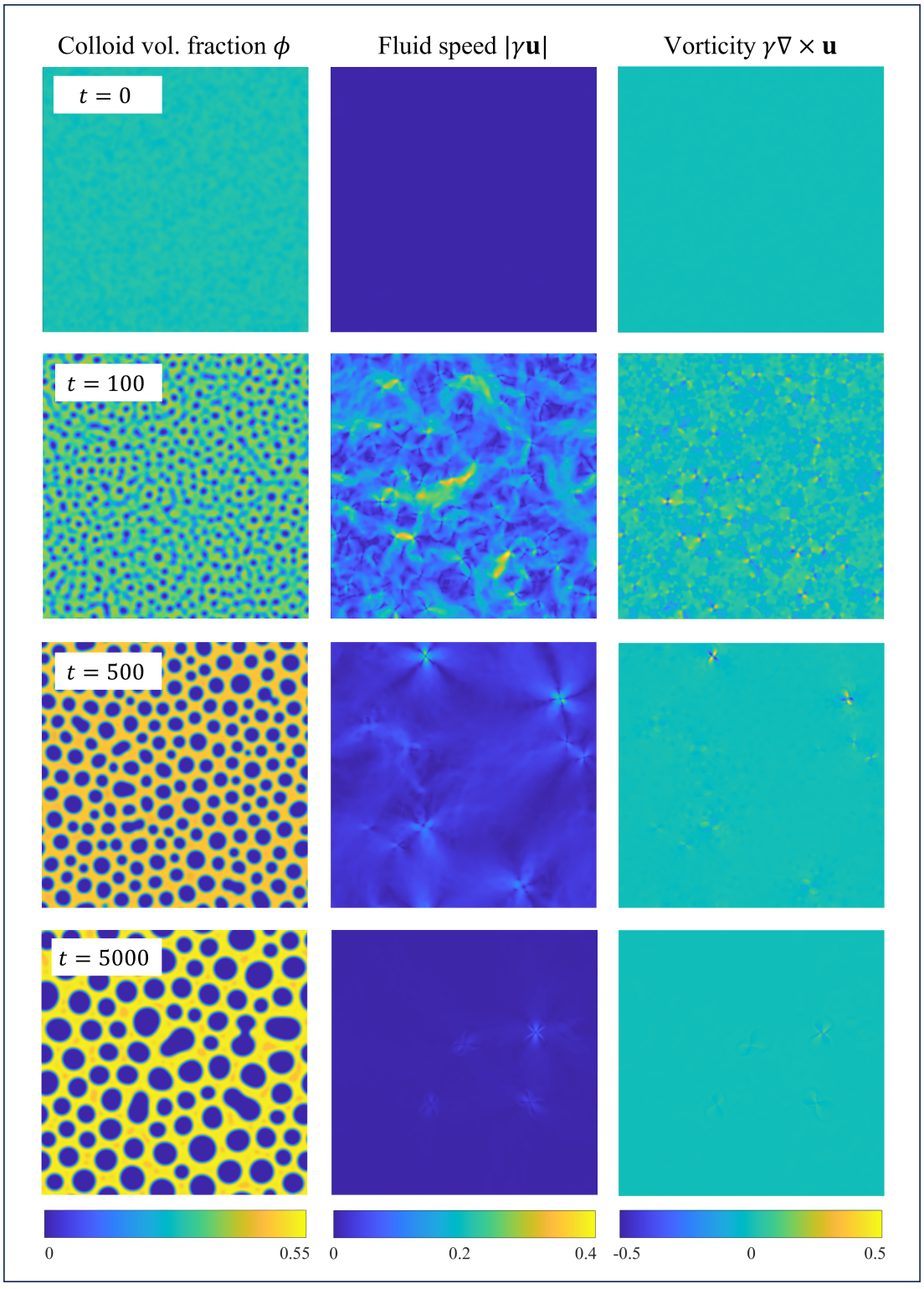

Figure 4.27 Simulation results for BCAT-5 Sample 7, with $\gamma = 50$. Each row represents a different (dimensionless) time t as labeled, with the three panels in each row corresponding to colloid volume fraction ϕ, fluid speed $|\gamma \mathbf{u}|$, and fluid vorticity $\gamma \nabla \times \mathbf{u}$, as labeled at the top of each column.

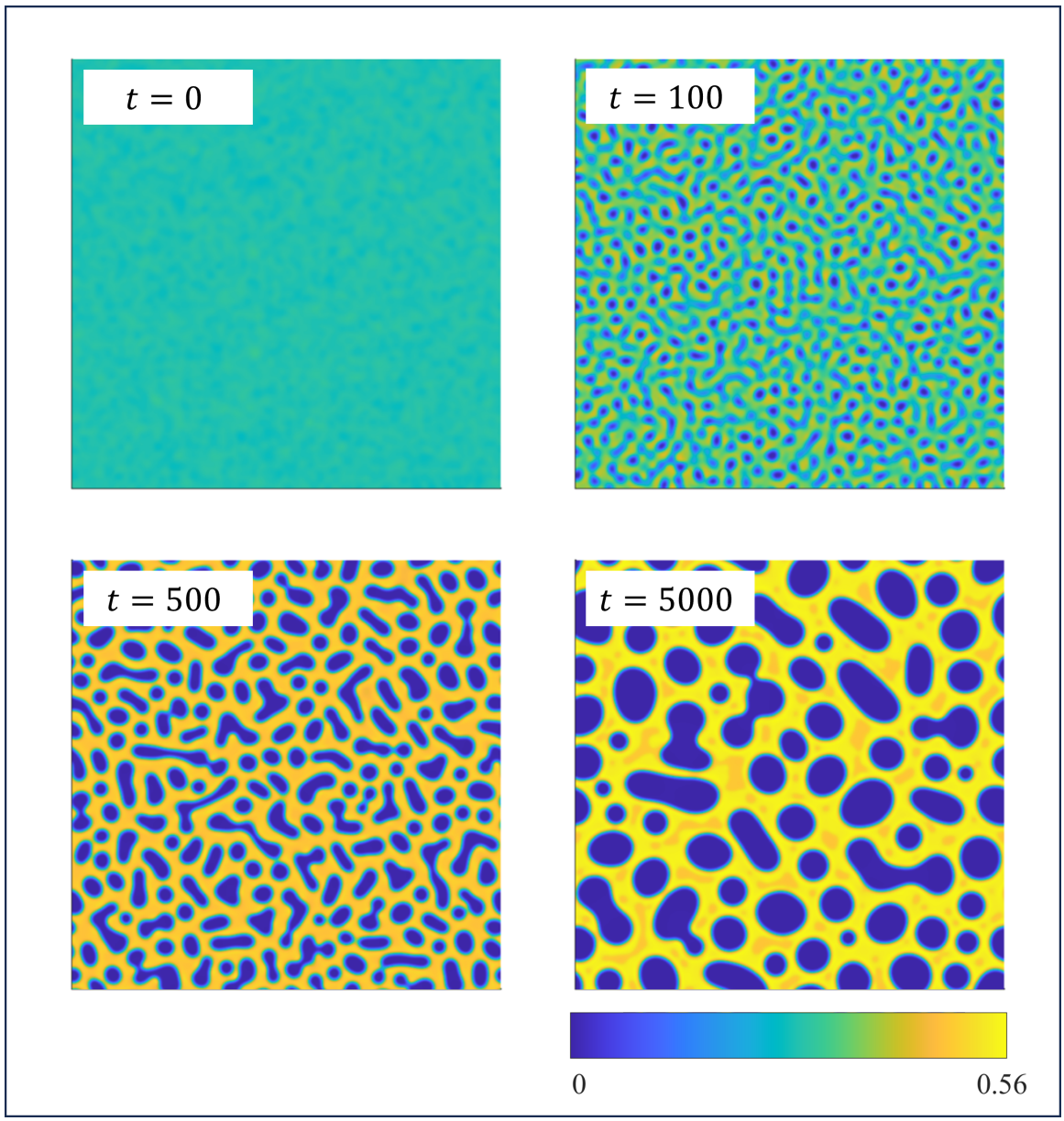

Figure 4.28 Simulation results for BCAT-5 Sample 7, without hydrodynamic effects ($\gamma = 0$). Each panel represents the colloid volume fraction ϕ at a different (dimensionless) time t, as labeled.

through a short-range Lennard-Jones potential by modeling colloids as fluid regions of relatively large viscosity. They found that including hydrodynamic interactions results in the formation of chainlike aggregates instead of circular clusters. This discrepancy with our results in Figures 4.29 and 4.30 is presumably due to the differences in our modeling framework, as the Cahn-Hilliard equation is not solved for in [50] so spinodal decomposition is not explicitly modeled.

Another interesting phenomenon we observed in our simulations in the presence of hydrodynamic interactions ($\gamma > 0$) is the formation of a quadrupole of vortices whenever two phase domains merge together, as illustrated in Figure 4.31. Each vortex quadrupole consists of two pairs of vortices: one pair is clockwise and the other counter-clockwise, positioned across from each other. In general, the fluid moves faster at earlier times when ϕ is nearly homogeneous; as the phase separation progresses, the fluid motion slows down significantly.

4.4.2 Quantifying phase domain growth in simulation outputs

After running the simulations for the BCAT samples, we then proceeded to implement the algorithm from Subsection 4.2.2 in order to obtain a quantitative description of the phase domain growth. This process is identical to the procedure we used on the NASA experiment images: we implement our algorithm directly on the $N \times N$ array that specifies the colloid volume fraction $\phi(\mathbf{x}, t)$ at a specific time t.

Our MATLAB code that implements the algorithm outputs the characteristic domain lengths λ_a in units of pixels, of which there are N in each spatial direction. Thus, to convert these λ_a values to dimensionless variables, we divide them by $N - 1$ and multiply by the dimensionless length $4\pi P$ of the simulation domain. After converting to dimensionless variables, we can obtain the desired dimensional units of millimeters and seconds by multiplying the dimensionless values λ_a and t by the

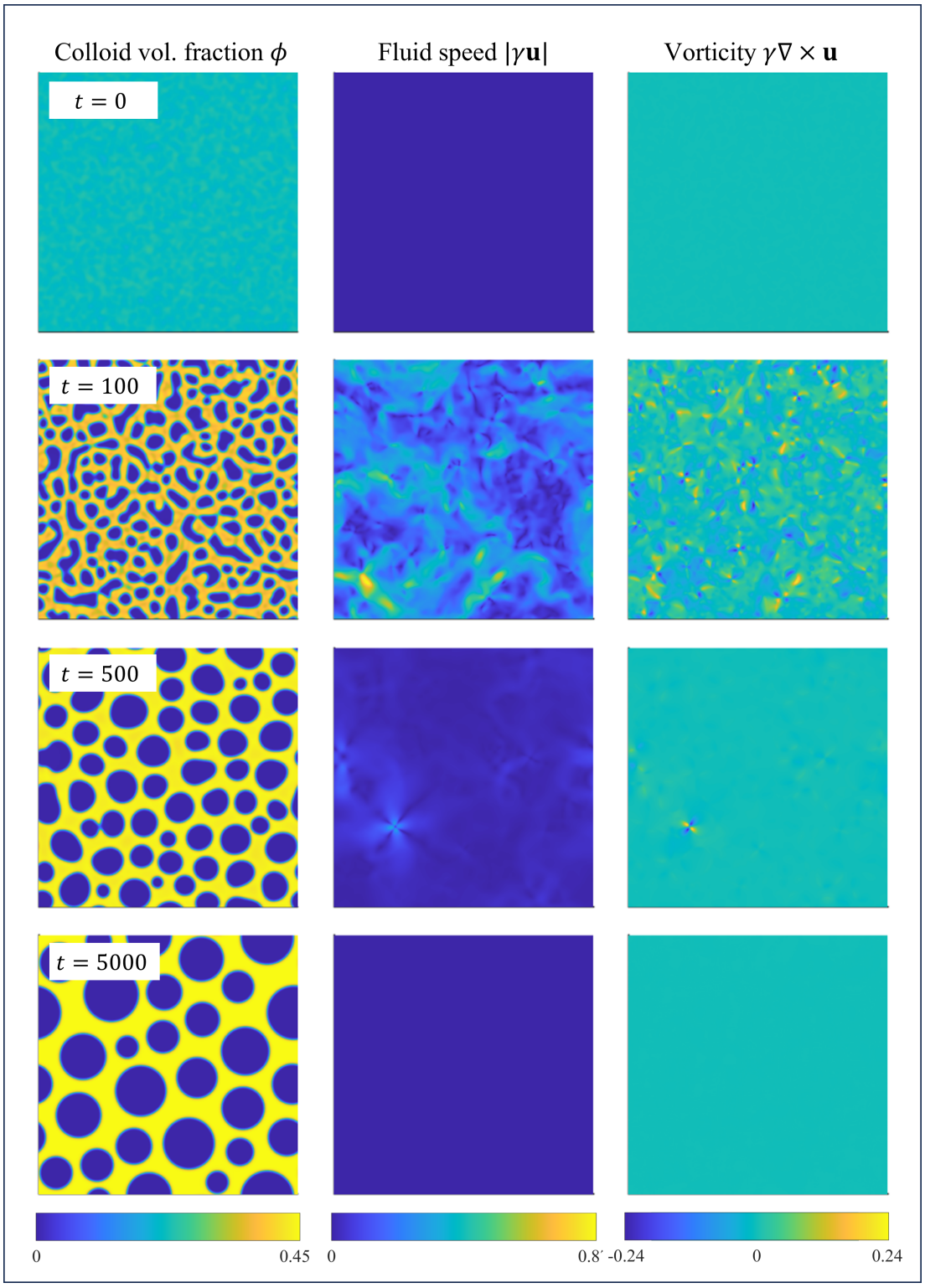

Figure 4.29 Simulation results for BCAT-5 Sample 4, with $\gamma = 50$. Each row represents a different (dimensionless) time t as labeled, with the three panels in each row corresponding to colloid volume fraction ϕ, fluid speed $|\gamma \mathbf{u}|$, and fluid vorticity $\gamma \nabla \times \mathbf{u}$, as labeled at the top of each column.

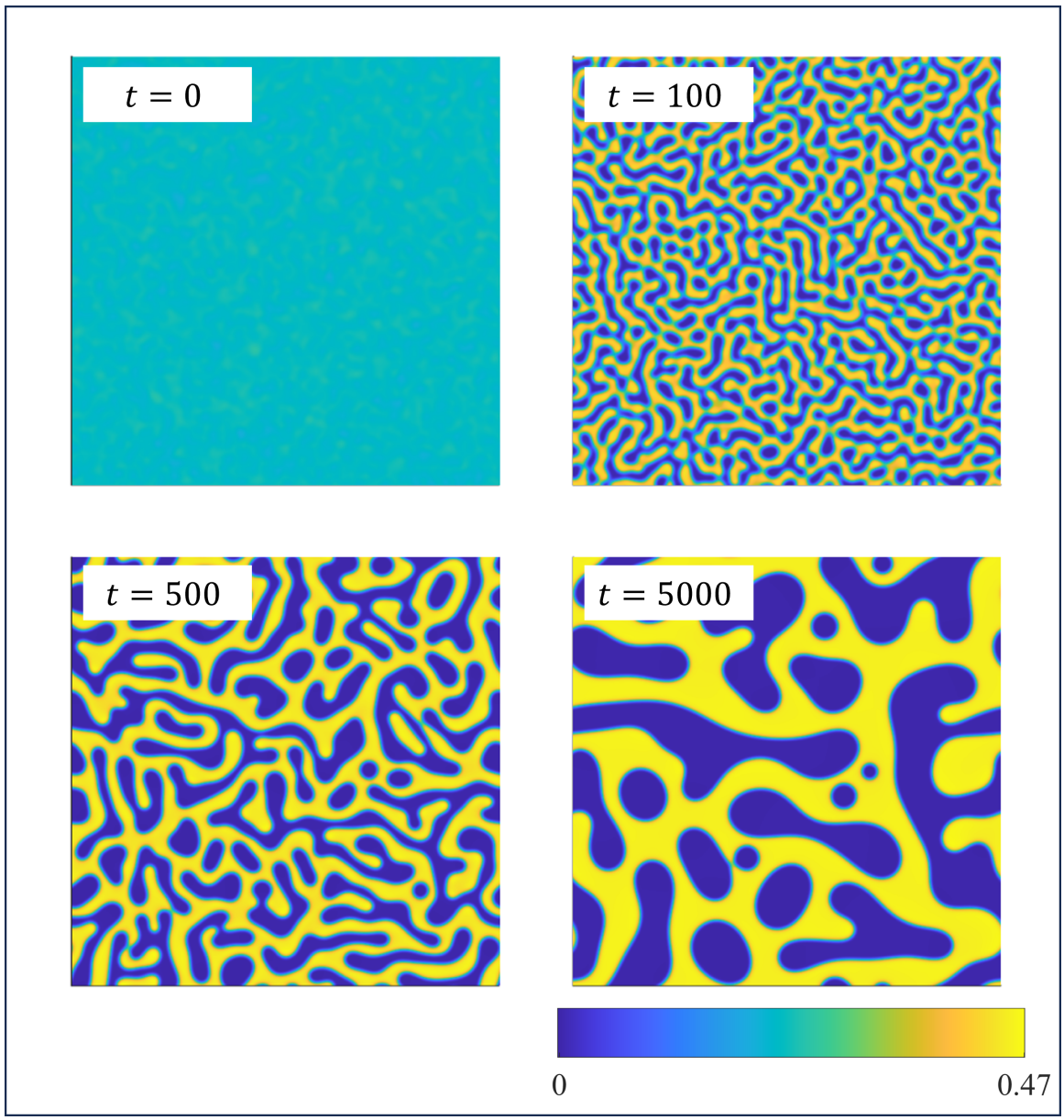

Figure 4.30 Simulation results for BCAT-5 Sample 4, without hydrodynamic effects ($\gamma = 0$). Each panel represents the colloid volume fraction ϕ at a different (dimensionless) time t, as labeled.

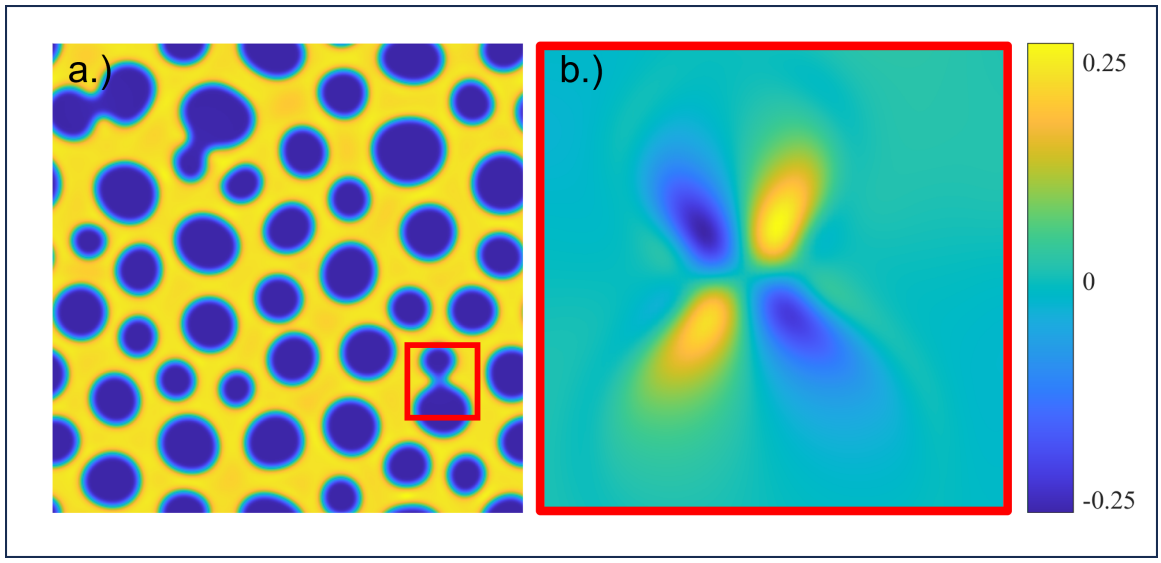

Figure 4.31 (a) Plot of ϕ for a BCAT-5, Sample 7 simulation using $\gamma = 50$ on a $4\pi P \times 4\pi P$ ($P = 10$) domain at (dimensionless) time $t = 527$. (b) Fluid vorticity $\gamma \nabla \times \mathbf{u}$ in the red-boxed region in Panel (a).

scaling factors L and τ, respectively, as given by (4.21). This requires a value for the free length parameter ℓ (refer to the discussion under Equation 4.19).

To obtain an appropriate value for ℓ, we experimented by plugging in various values for ℓ and plotting the corresponding curves (now in dimensional units) for each ℓ on the same axes as the experimental data, as shown in Figure 4.32. We did this for each of the five BCAT-5 samples, selecting the ℓ-value that best matched the experimental data. Then, we chose an ℓ-value about midway between the highest and lowest out of the "best" ones for the five samples; we use this "best overall" value as our ℓ for all five samples in BCAT-5. A comparison between the best value of ℓ for each individual sample and the best overall ℓ is depicted in Figures 4.33-4.37, which correspond to BCAT-5 Samples 4, 5, 6, 7 and 8, respectively. The green curve in the plot on the left in each figure is the simulation curve, in dimensional variables, using the overall best ℓ, which we found to be $\ell = 0.27$ mm. The purple curve in the plot on the right is the simulation curve with the best ℓ for each specific sample. The blue

curve in both plots is the experimental data. All simulation curves in these figures were run with $\gamma = 50$.

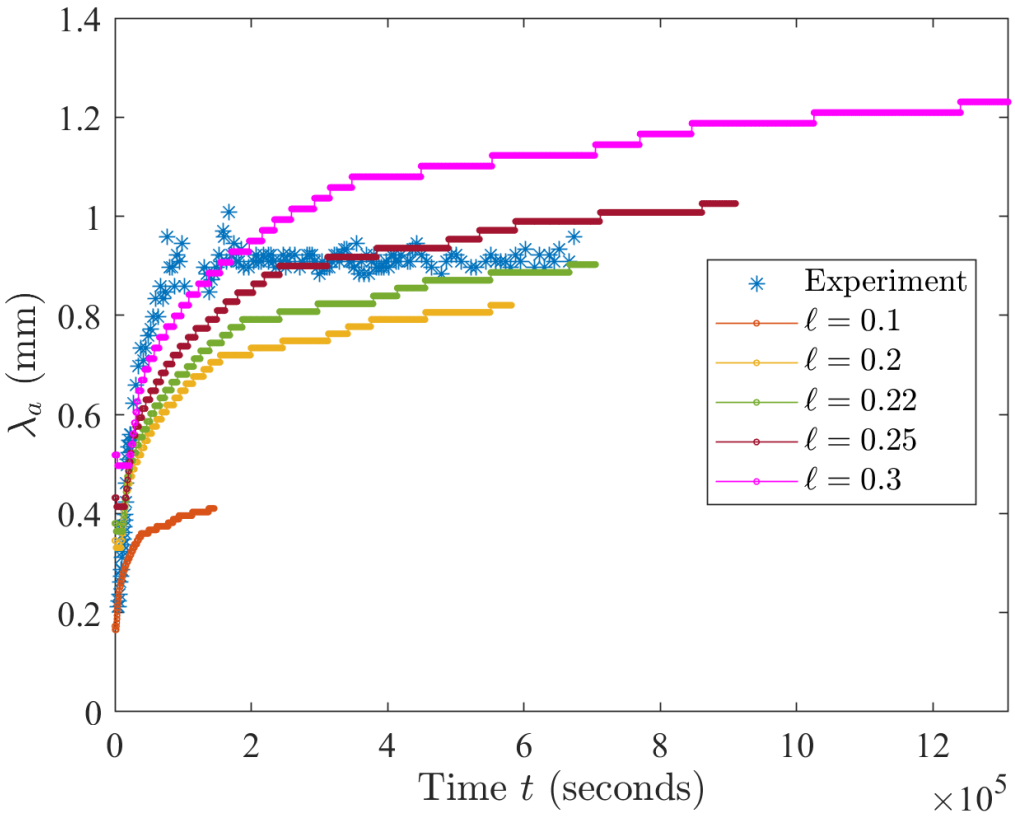

Figure 4.32 Autocorrelation curve λ_a vs. t for BCAT-5 Sample 7, obtained from numerical simulations using $\gamma = 50$, plotted on the same axes with the experimental data (blue curve). The different colors correspond to different choices of ℓ (in mm) used in computing the scaling factors L and τ defined in Equation (4.21).

Using $\ell = 0.27$ mm, we then calculate the appropriate length scale L and time scale τ, as given by (4.21), for each sample. Multiplying the dimensionless values λ_a and t by L and τ, respectively, we obtain values of λ_a and t in *dimensional* units of mm and seconds. These dimensional values may now be compared with the corresponding growth curves for the experiment image data. Figure 4.38 shows the growth curves for BCAT-5 Samples 4, 5, 6, 7 and 8, for both the experimental data (triangles) and the simulation data (solid curves) in the absence of hydrodynamic interactions ($\gamma = 0$). Hydrodynamic interactions are accounted for in Figure 4.39, for which $\gamma = 50$.

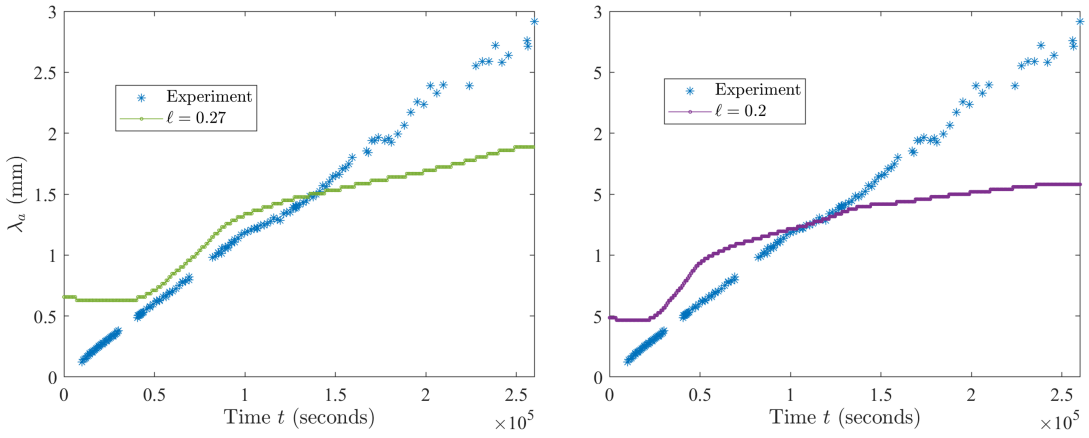

Figure 4.33 Autocorrelation curve λ_a vs. t for BCAT-5 Sample 4, obtained from numerical simulations using $\gamma = 50$, plotted on the same axes with the experimental data for (a) $\ell = 0.27$ mm and (b) $\ell = 0.2$ mm. The value $\ell = 0.2$ mm was chosen to make the simulation curve match as closely as possible with the experimental curve for this particular sample, and the value $\ell = 0.27$ mm was chosen as the "best" value to accommodate all five of the BCAT-5 samples.

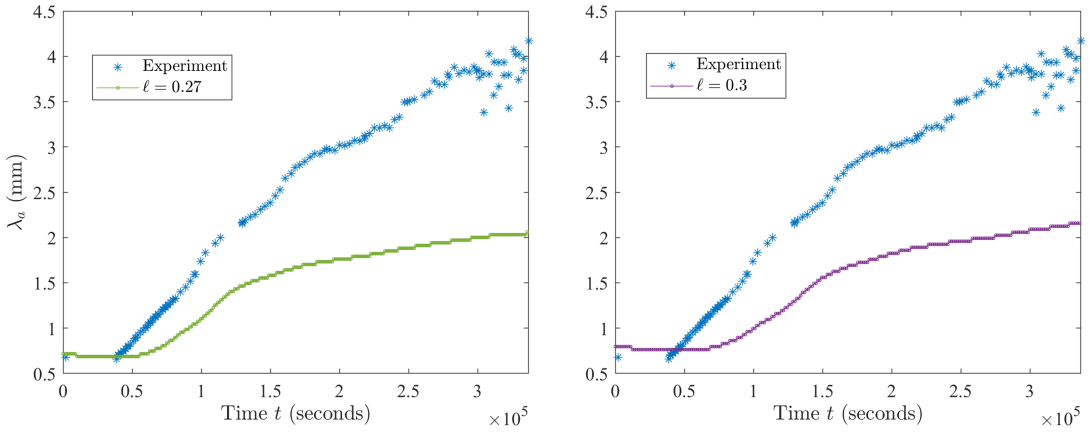

Figure 4.34 Autocorrelation curve λ_a vs. t for BCAT-5 Sample 5, obtained from numerical simulations using $\gamma = 50$, plotted on the same axes with the experimental data for (a) $\ell = 0.27$ mm and (b) $\ell = 0.3$ mm. The value $\ell = 0.3$ mm was chosen to make the simulation curve match as closely as possible with the experimental curve for this particular sample, and the value $\ell = 0.27$ mm was chosen as the "best" value to accommodate all five of the BCAT-5 samples.

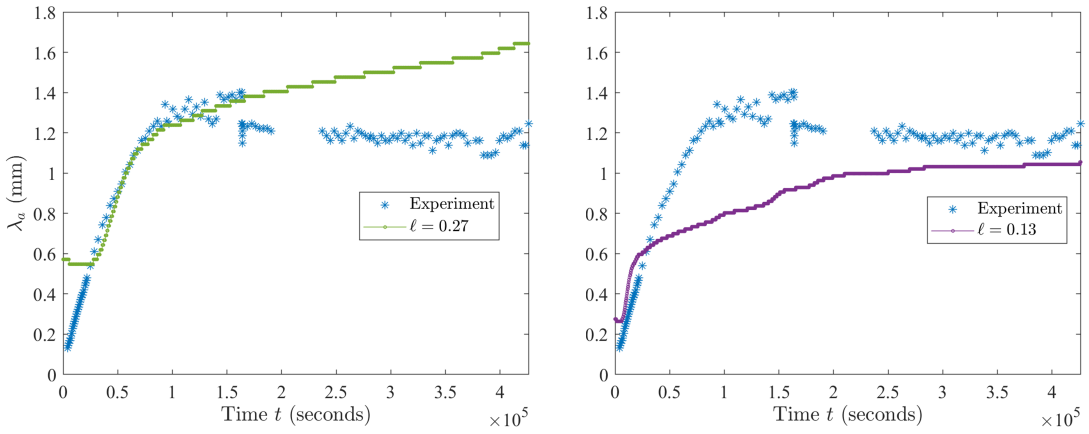

Figure 4.35 Autocorrelation curve λ_a vs. t for BCAT-5 Sample 6, obtained from numerical simulations using $\gamma = 50$, plotted on the same axes with the experimental data for (a) $\ell = 0.27$ mm and (b) $\ell = 0.13$ mm. The value $\ell = 0.13$ mm was chosen to make the simulation curve match as closely as possible with the experimental curve for this particular sample, and the value $\ell = 0.27$ mm was chosen as the "best" value to accommodate all five of the BCAT-5 samples.

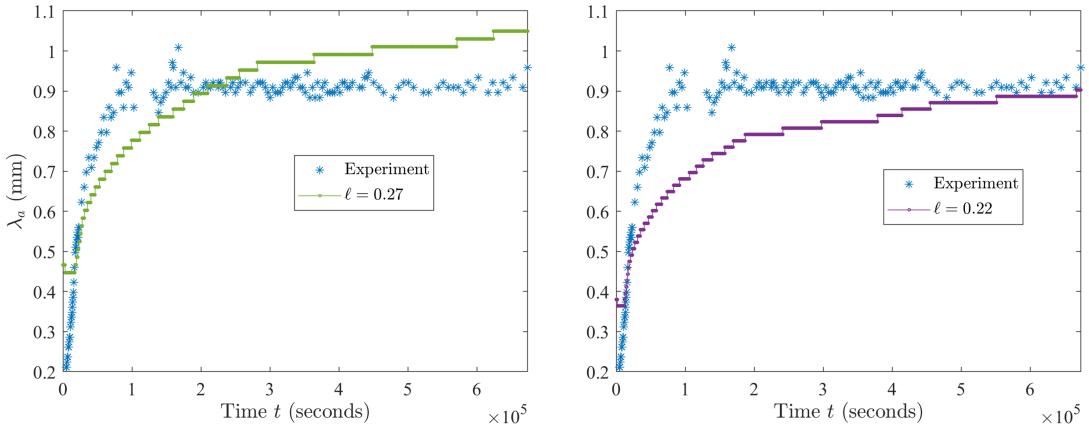

Figure 4.36 Autocorrelation curve λ_a vs. t for BCAT-5 Sample 7, obtained from numerical simulations using $\gamma = 50$, plotted on the same axes with the experimental data for (a) $\ell = 0.27$ mm and (b) $\ell = 0.22$ mm. The value $\ell = 0.22$ mm was chosen to make the simulation curve match as closely as possible with the experimental curve for this particular sample, and the value $\ell = 0.27$ mm was chosen as the "best" value to accommodate all five of the BCAT-5 samples.

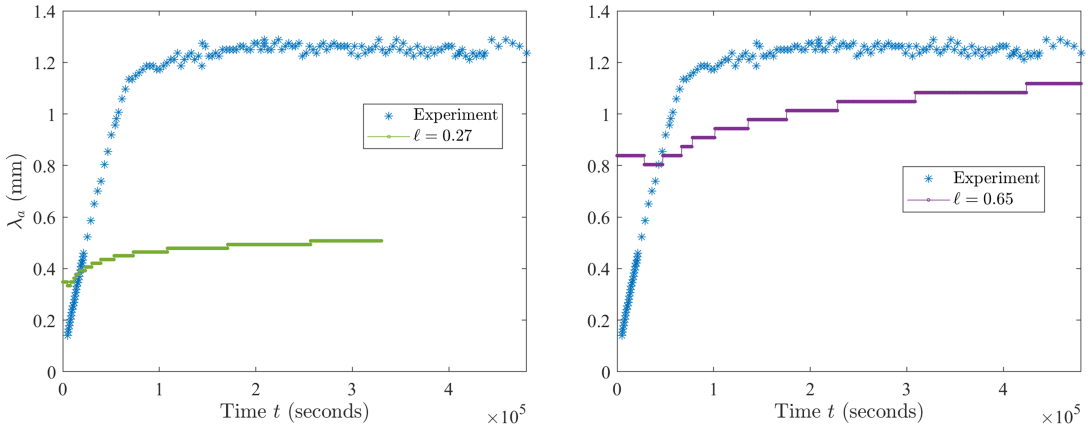

Figure 4.37 Autocorrelation curve λ_a vs. t for BCAT-5 Sample 8, obtained from numerical simulations using $\gamma = 50$, plotted on the same axes with the experimental data for (a) $\ell = 0.27$ mm and (b) $\ell = 0.65$ mm. The value $\ell = 0.65$ mm was chosen to make the simulation curve match as closely as possible with the experimental curve for this particular sample, and the value $\ell = 0.27$ mm was chosen as the "best" value to accommodate all five of the BCAT-5 samples.

Comparing these two figures illustrates the importance of hydrodynamic effects, as the two possess qualitatively different behavior. We first focus our attention on the $\gamma = 50$ case (Figure 4.39), where hydrodynamic effects *are* considered. While the experimental and simulation data do not compare exactly, the dependence of the final length scale on sample parameters is mostly consistent between experiment and simulation. Specifically, for the experimental data, the largest λ_a values are attained by the Sample 5 curve (red), followed by Sample 4 (blue), followed by Sample 6 (yellow) and Sample 8 (green), which are nearly the same. Sample 6 attains higher values overall than Sample 8, but its values eventually decrease (presumably due to an artifact of the image processing) and settle at a lower value than Sample 8. Finally, Sample 7 (purple) attains the smallest values. For the simulation data, the ordering is as follows: Sample 5 (red), Sample 4 (blue), Sample 6 (yellow), Sample 7 (purple), and finally Sample 8 (green), which is consistent with the ordering of the experimental data with the exception of Sample 8. Moreover, we note that, by

choosing a single value of ℓ, the values of λ_a predicted by the simulations are the same order of magnitude as those in experiment.

In the absence of hydrodynamic effects, $\gamma = 0$ (Figure 4.38), the simulation curves for the five samples are clustered closer together than in Figure 4.39; the values of λ_a for Samples 4, 5 and 6 at the latest time considered (10^{-7}) are quite similar to each other, while Sample 7 attains significantly lower values and Sample 8 attains the lowest of all. Inclusion of hydrodynamic interactions appears to cause the λ_a-curves to separate from each other, making the different sample parameters more distinguishable from each other.

We note also that the early-time growth rates of the simulation curves in Figure 4.39 are more similar to the experimental data than those in Figure 4.38, indicating that the hydrodynamic effects contribute to early-time behavior of the system. Specifically, in Samples 6, 7 and 8 we observe faster domain growth at early times, followed by a slowing down of the growth at later times. This behavior is reflected more in the $\gamma = 50$ simulation curves than in the $\gamma = 0$ simulation curves.

To analyze this observation more closely, we made a plot for each sample of the $\gamma = 0$ and $\gamma = 50$ simulation curves in dimensionless variables, together on the same axes, as shown in Figure 4.40. Doing this provides a direct comparison, for each of the five BCAT-5 samples, between the qualitative behavior with and without hydrodynamic effects. At early times, the $\gamma = 50$ curve (red) for each sample exhibits faster growth than its $\gamma = 0$ counterpart (blue). Both curves begin to flatten out as time progresses, indicating a slowing down of the phase domain growth. In each plot, this slowing starts earlier with hydrodynamics (red) than without (blue). These results suggest that the inclusion of hydrodynamic effects initially speeds up the phase separation process, but eventually slows it down at later times. Specifically, the increase in suspension viscosity (4.17) and decrease in mobility (4.6) as the colloid volume fraction increases may lead to phase separation being hindered or

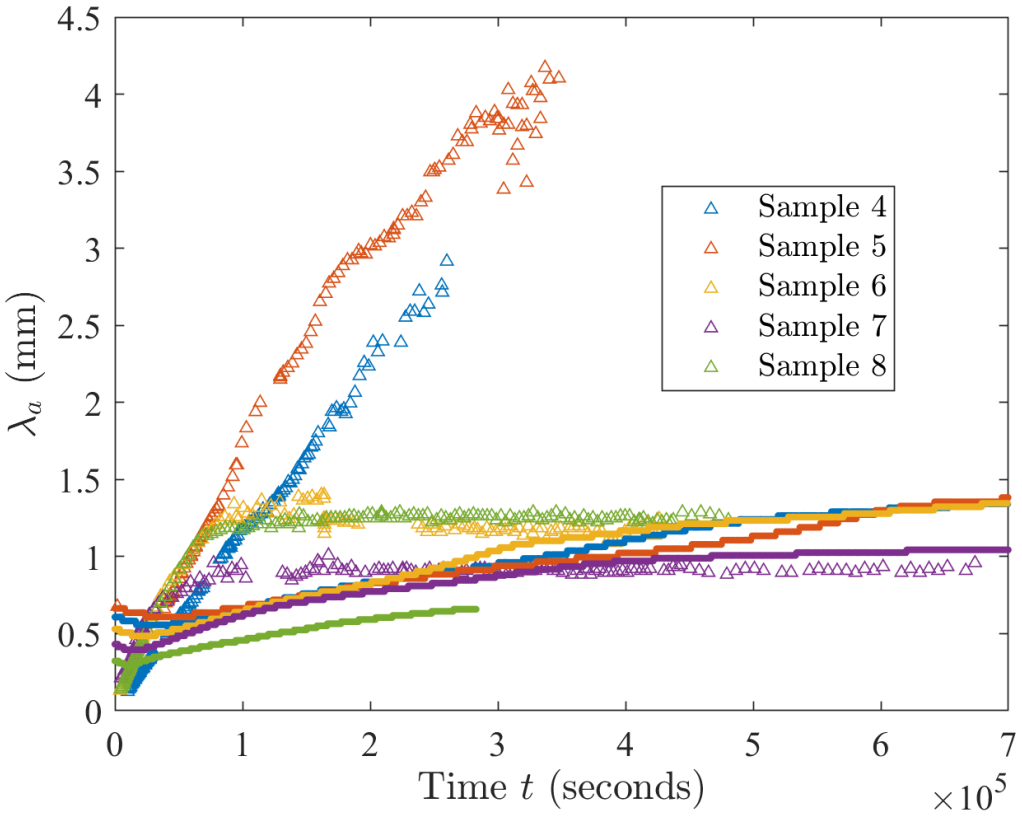

Figure 4.38 BCAT-5 autocorrelation curves for Samples 4, 5, 6, 7 and 8, obtained from experimental data (triangles) and simulations (solid curves) run without accounting for hydrodynamic interactions ($\gamma = 0$) using $N = 512$ spatial grid points on a $P = 20$-period domain, with the free parameter value $\ell = 0.27$ mm.

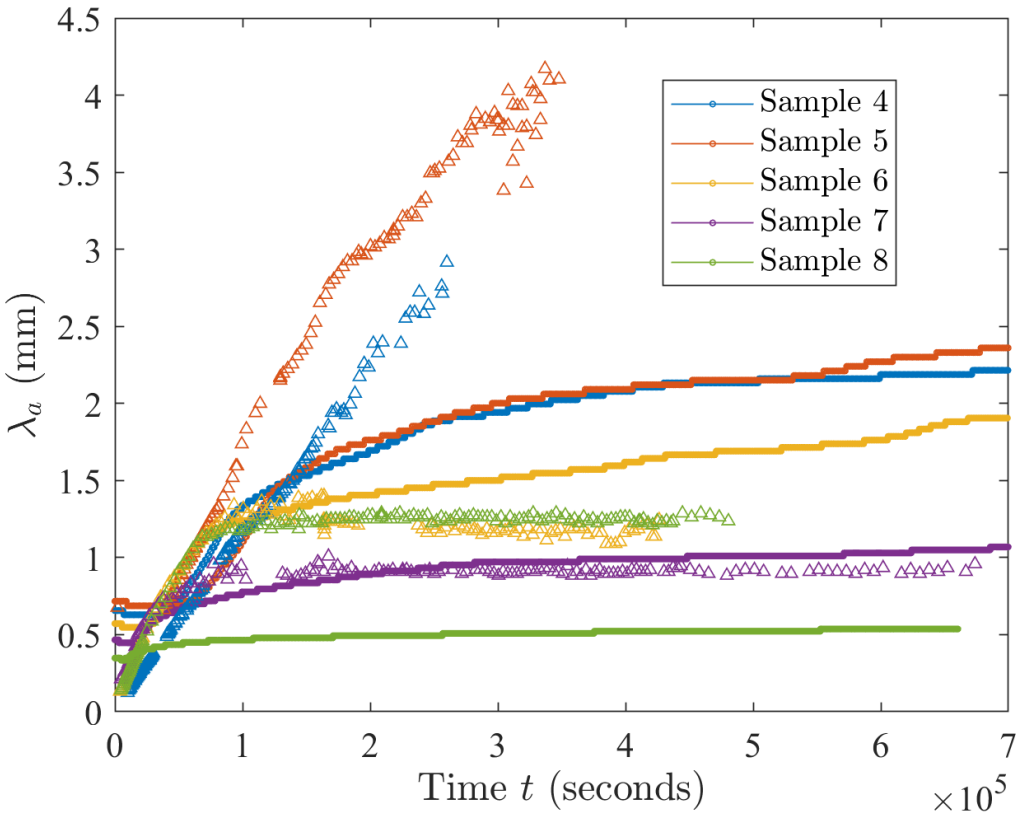

Figure 4.39 BCAT-5 autocorrelation curves for Samples 4, 5, 6, 7 and 8, obtained from experimental data (triangles) and simulations (solid curves) run with $\gamma = 50$ using $N = 512$ spatial grid points on a $P = 20$-period domain, with the free parameter value $\ell = 0.27$ mm.

even arrested in a colloid-polymer suspension. This mechanism would be in addition to the one identified by Sabin *et al.* [104], who analyzed microgravity experiments of colloid-polymer suspensions. They found that phase separation was arrested due to the emergence of a system-spanning crystal gel, an effect that cannot be captured by our model because it does not include gelation.

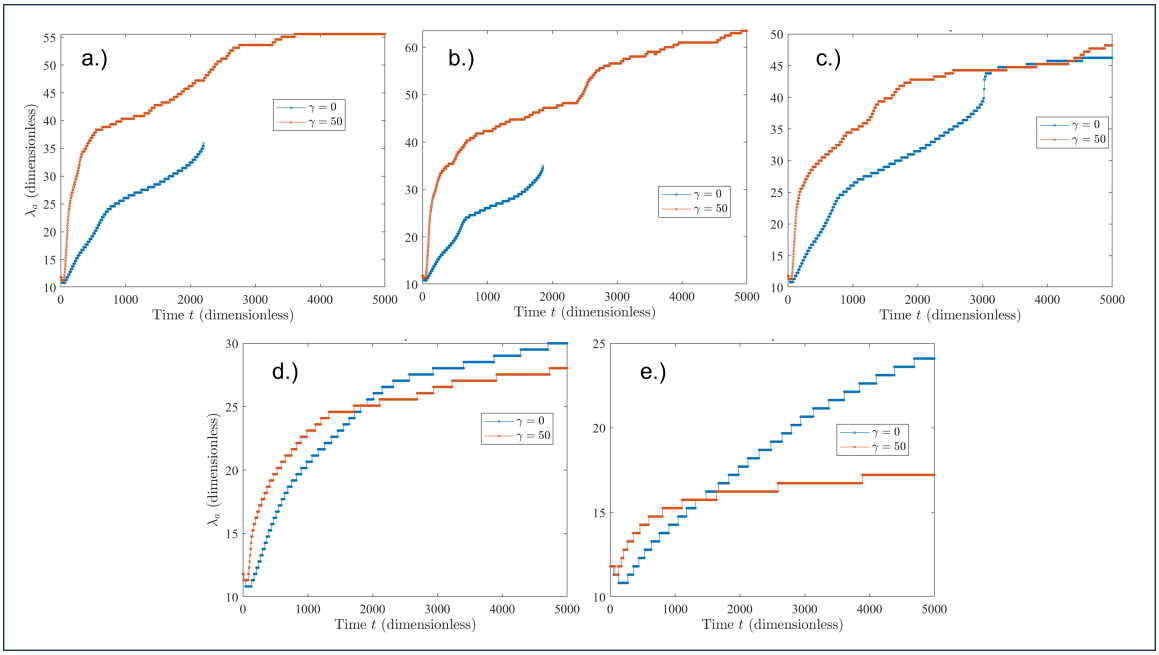

Figure 4.40 Characteristic domain length λ_a, as obtained from our numerical simulations, plotted as a function of t (in dimensionless variables) for the five samples in BCAT-5: (a) Sample 4, (b) Sample 5, (c) Sample 6, (d) Sample 7, and (e) Sample 8. The blue curve in each panel corresponds to $\gamma = 0$ (no hydrodynamic interactions) and the red curve to $\gamma = 50$. All simulations in this figure were run on a $4\pi P \times 4\pi P$ ($P = 20$) domain with $N = 512$ spatial grid points in each spatial direction. In Panels (a) and (b), the blue ($\gamma = 0$) curves were cut short because the autocorrelation curve exhibited a discontinuous jump in values, a numerical artifact.

4.4.3 Validations and checks

To verify that our simulation domain size is sufficiently large to obtain an accurate measurement from the autocorrelation function, we ran several simulations of the same sample (BCAT-5 Sample 7) with the same number of spatial grid points ($N = 512$) and Peclet number value ($\gamma = 50$), but varying the domain size. Specifically,

we selected three different (dimensionless) domain sizes $4\pi P \times 4\pi P$, choosing $P = 10$, $P = 20$, and $P = 40$ (see Figure 4.41(a)). Similarly, to ensure that we are using sufficiently many spatial grid points for the simulations, we ran several more simulations of BCAT-5 Sample 7 with $\gamma = 50$, keeping the domain size constant ($P = 10$) and using two different values $N = 256$ and $N = 512$ (see Figure 4.41(b)). We then repeated a similar test for a larger domain size, $P = 40$, comparing the appearance of the curve when using $N = 512$ and $N = 1024$ to resolve this larger domain (Figure 4.41(c)). Taken together, the results in Figure 4.41 show that the predicted domain growth curve is roughly independent of both simulation domain size and spatial resolution, as desired.

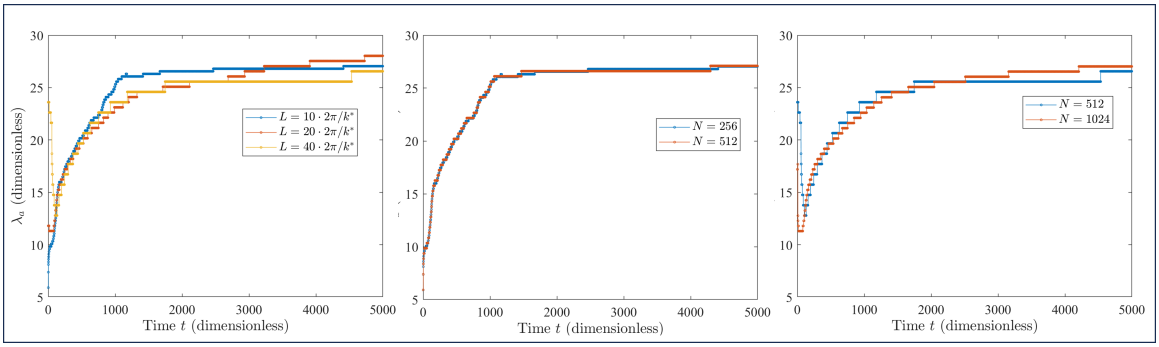

Figure 4.41 (a) Autocorrelation curves obtained from model simulations of BCAT-5 Sample 7 with $\gamma = 50$ on a $N \times N$ spatial grid for $N = 512$, for three different (dimensionless) domain sizes $4\pi P \times 4\pi P$: $P = 10$, $P = 20$, and $P = 40$.
(b) Autocorrelation curves obtained from model simulations of BCAT-5 Sample 7 with $\gamma = 50$ and $P = 10$, for two different values $N = 256$ and $N = 512$.
(c) Autocorrelation curves obtained from model simulations of BCAT-5 Sample 7 with $\gamma = 50$ and $P = 40$, for two different values $N = 512$ and $N = 1024$.

4.4.4 Preliminary results for BCAT-3 and BCAT-4

Our simulations of the BCAT-3 and BCAT-4 experiments are ongoing. Several preliminary simulations have been run, with some results shown in Figures 4.42- 4.45. Figures 4.42 and 4.43 show the autocorrelation curves corresponding to simulations of BCAT-3, plotted on the same axes as the experimental data: without hydrodynamic interactions (Figure 4.42) and with hydrodynamic interactions (Figure 4.43.) The

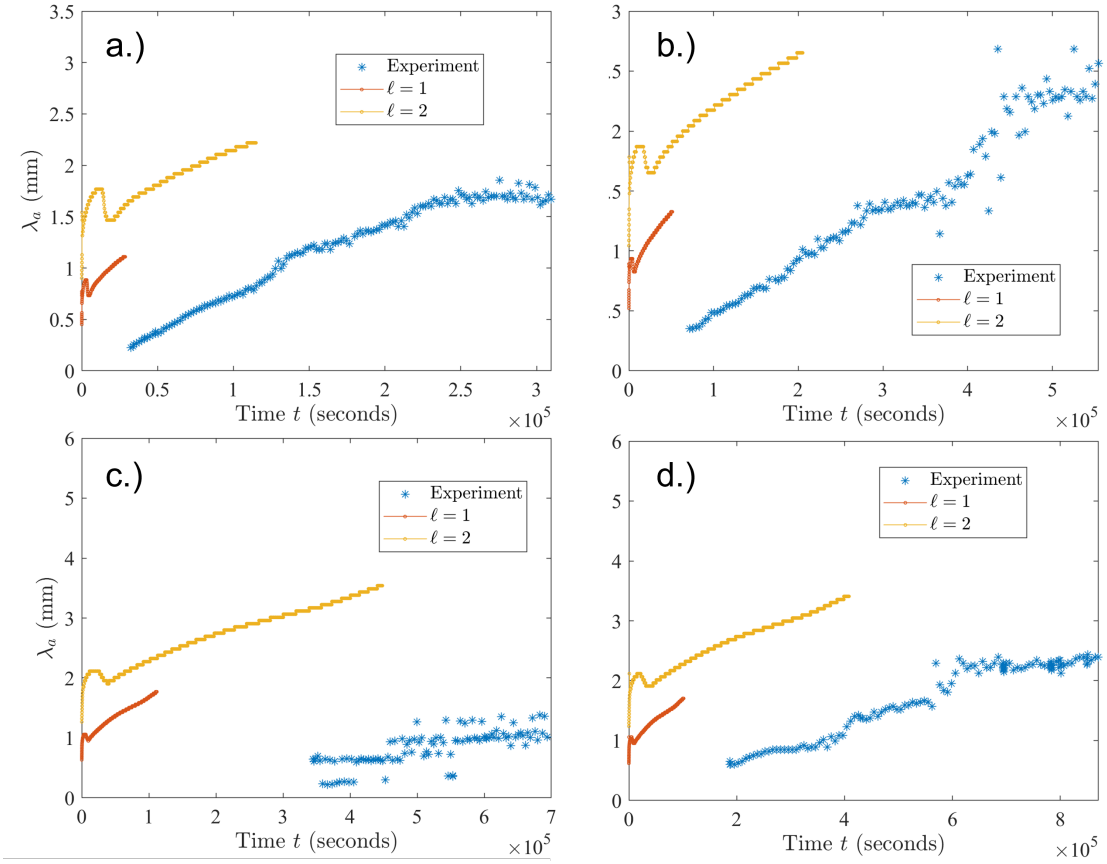

Figure 4.42 Autocorrelation curve λ_a vs. t for all four BCAT-3 samples, obtained from numerical simulations using $\gamma = 0$, plotted on the same axes with the experimental data: (a) Sample 1, (b) Sample 2, (c) Sample 4, and (d) Sample 6. The red and yellow curves correspond to choosing $\ell = 1$ and $\ell = 2$, respectively, for the free length scale parameter ℓ.

curves are plotted in dimensional values, with the yellow curve obtained by using the value $\ell = 1$ for the "free parameter" in the definitions of the length and time scales L and τ; the red curve was obtained using $\ell = 2$. Figures 4.44 and 4.45 show the BCAT-4 simulation curves plotted with the experimental ones, for $\gamma = 0$ and $\gamma = 50$ respectively; the curve colors denote the same ℓ-values as in Figures 4.42 and 4.43.

The λ_a-values in the $\ell = 2$ (yellow) simulation curves in Figure 4.42 differ from the experimental curves by a factor of between ≈ 1.5 and ≈ 2 mm or more, although the curves' slopes appear to match reasonably well with the experimental data. The curves in Figure 4.44 exhibit similar features, both qualitatively and quantitatively. In

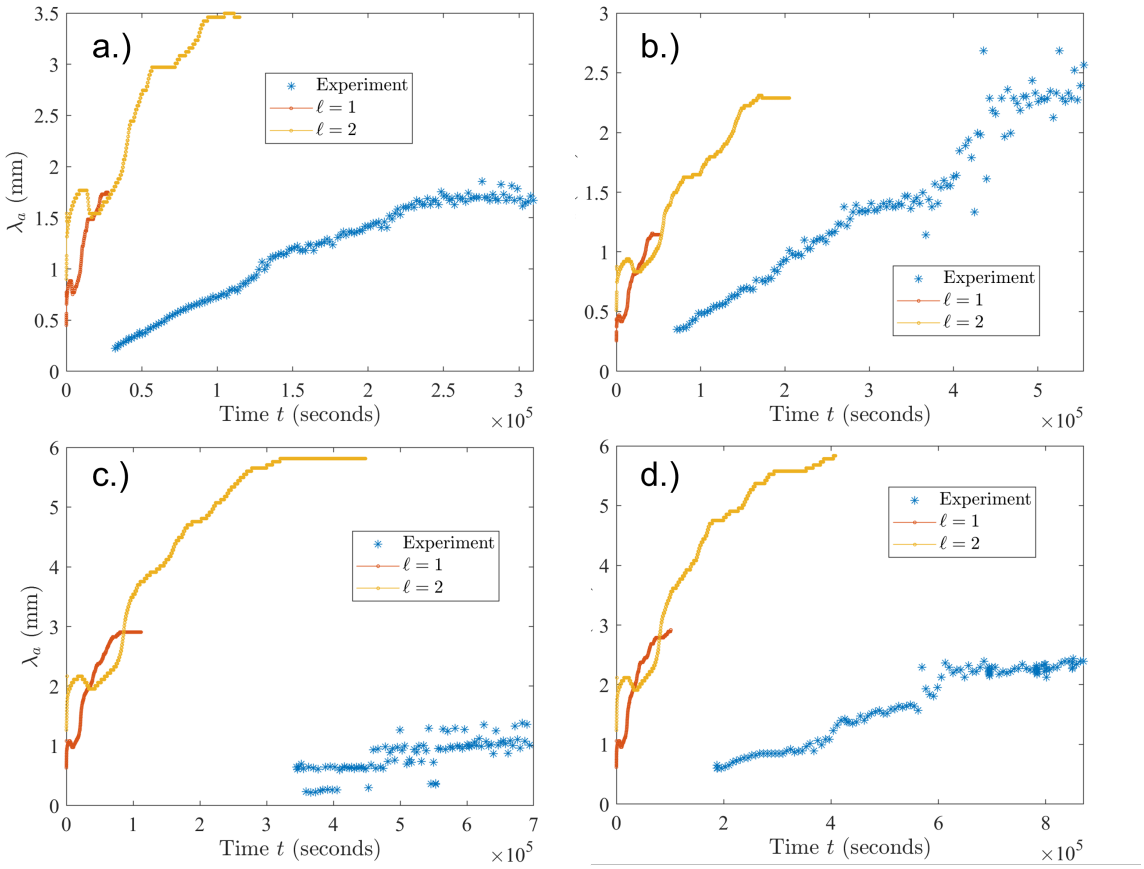

Figure 4.43 Autocorrelation curve λ_a vs. t for all four BCAT-3 samples, obtained from numerical simulations using $\gamma = 50$, plotted on the same axes with the experimental data: (a) Sample 1, (b) Sample 2, (c) Sample 4, and (d) Sample 6. The red and yellow curves correspond to choosing $\ell = 1$ and $\ell = 2$, respectively, for the free length scale parameter ℓ.

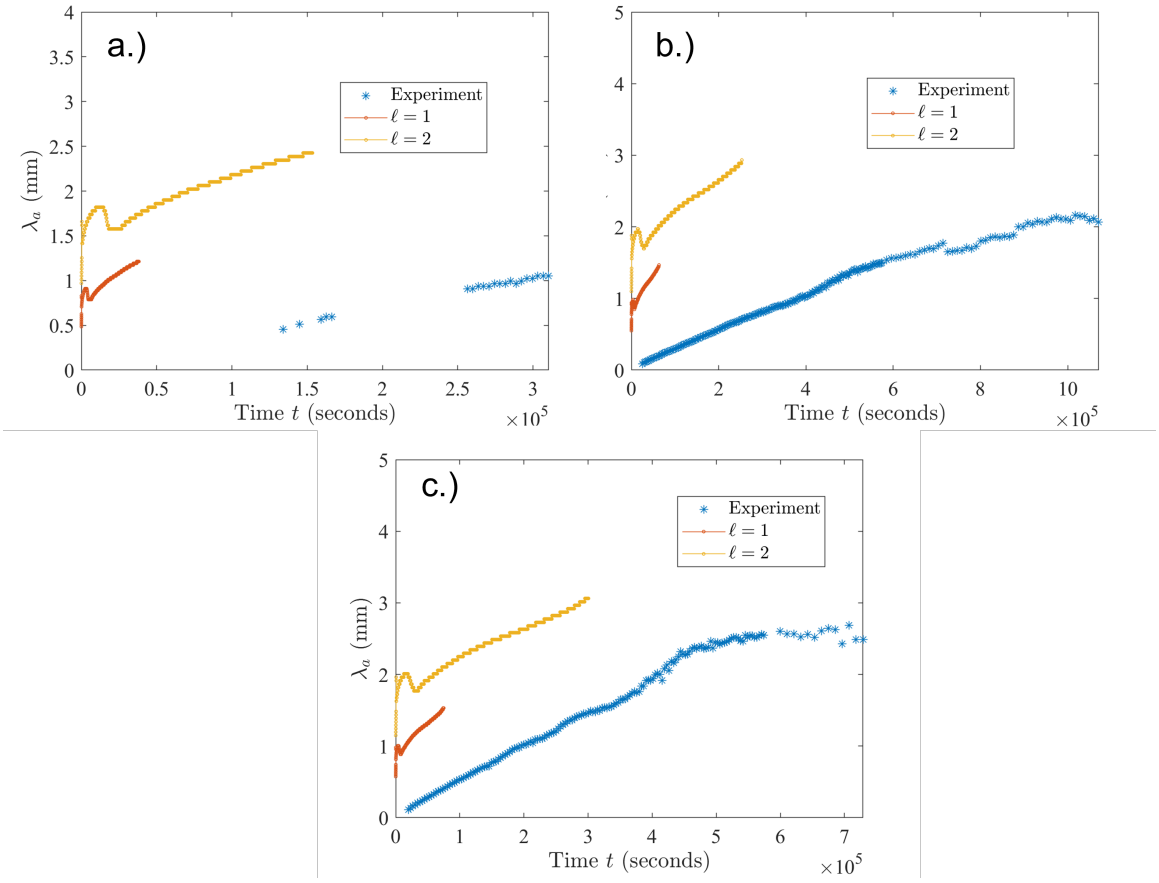

Figure 4.44 Autocorrelation curve λ_a vs. t for all four BCAT-4 samples, obtained from numerical simulations using $\gamma = 0$, plotted on the same axes with the experimental data: (a) Sample 1, (b) Sample 2, and (c) Sample 3. The red and yellow curves correspond to choosing $\ell = 1$ and $\ell = 2$, respectively, for the free length scale parameter ℓ.

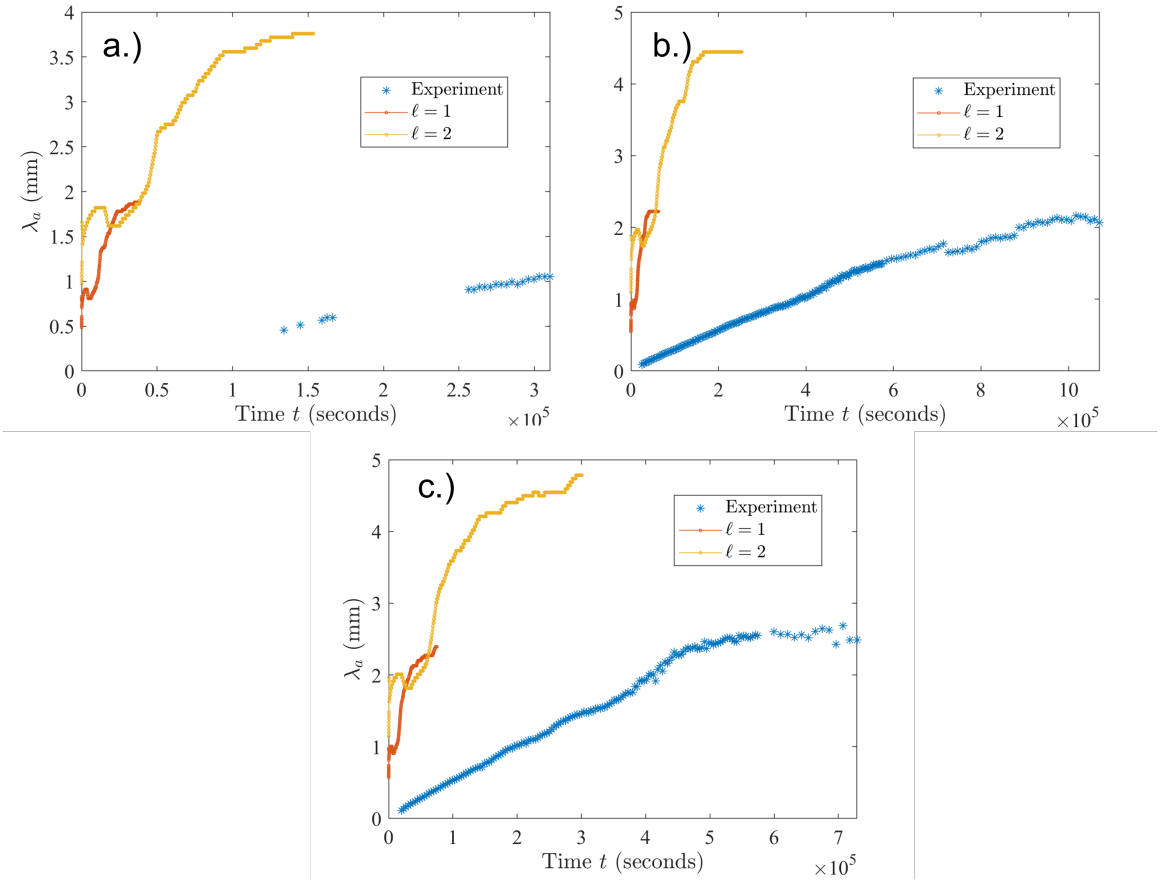

Figure 4.45 Autocorrelation curve λ_a vs. t for all four BCAT-4 samples, obtained from numerical simulations using $\gamma = 50$, plotted on the same axes with the experimental data: (a) Sample 1, (b) Sample 2, and (c) Sample 3. The red and yellow curves correspond to choosing $\ell = 1$ and $\ell = 2$, respectively, for the free length scale parameter ℓ.

the presence of hydrodynamic interactions (Figures 4.43 and 4.45), the discrepancies between simulation and experiment values is substantially larger than in the $\gamma = 0$ case, and the curves' slopes do not match. The reason for the significant discrepancies in all of these figures is likely due to the ξ-values for BCAT-3 and BCAT-4 being relatively large, putting these experiments in a parameter regime for which the free-volume theory proposed by [74] is not valid. Further investigation of this would require running the simulations out to longer dimensionless times, which we hope to do in the future.

4.5 Discussion and Future Work

We have processed and analyzed large sets of images from NASA's BCAT experiments on colloid-polymer suspensions. In particular, we have extracted meaningful data from the images that provide a quantitative description of the phase domain coarsening process in each of the samples. We have also presented a theoretical model for phase separation in colloid-polymer suspensions which includes the effects of hydrodynamic interactions between the colloid particles and the surrounding fluid. Finally, we have presented results from our simulations of this model and compared these results with the experimental data extracted from the NASA images.

Since our model is a phase-field model, we are essentially treating the colloid particles as a continuum field. This is one of several considerable approximations that our model makes. Another such approximation is the use of the Korteweg stress term in our incompressible Stokes equations: the actual influence of a suspension of small spheres (colloids) on fluid flow is far more complex. In spite of these significant simplifications in our model, however, our simulation results have shown that the order of magnitude predictions are correct.

Our simulation results have also provided some insight into the role of hydrodynamic effects on phase separation in colloid-polymer suspensions. In particular,

we have seen that the hydrodynamic effects tend to accelerate the growth of phase domains at early times, and then slow it down at later times. We also observed that the phase domain structures take on a more stringy appearance when hydrodynamic interactions are neglected.

There are several future directions we hope to take for this investigation. First, simulations of the BCAT-3 and BCAT-4 samples are still ongoing; we intend to run the simulations for longer and then analyze these results in a similar manner as for BCAT-5. We also hope to improve our model by eliminating the assumption that the polymer chemical potential is constant, which our model assumes for simplicity. Doing so will introduce another variable, the polymer concentration, which will have to be evolved in time as well. To this end, we plan to explore the idea of using the generalized free-volume theory presented in [48] to obtain an expression for the polymer concentration. This will improve the accuracy of our model in several ways. First, it is more physically accurate because it incorporates an additional physical mechanism instead of ignoring it for simplicity. Second, it is more relevant for the parameter regime we are interested in. The free-volume theory used to obtain the formulation in [48] is valid for the parameter regime corresponding to the BCAT experiments; note that the free-volume theory presented in [74] is intended for suspensions with polymer-to-colloid size ratio $\xi < 0.5$, which is smaller than the value in the BCAT experiments.

In addition to improving our model's accuracy, another future goal is to make our code more efficient by improving the numerics. One such improvement would be to make the time-stepping adaptive, since the phase separation tends to slow down as time progresses and the fluid moves faster when merger of domains occurs. Thus, it is likely we can get away with a larger time step size at later times. Similarly, another numerical avenue worth exploring is the use of higher-order time-stepping. Zhu *et*

al. [120] proposed a second-order scheme; we have begun the process of implementing this but still need to make some modifications in order to use it for our simulations.

Another future direction would be to explore the validity of the hypotheses advanced by Evans *et al.* [44], who proposed that the interface between colloid-rich (solid) and colloid-poor (gas) may "unbind" into two separate interfaces with a metastable intermediate phase separating them. This effect was hypothesized to impede the growth of the solid phase. The simulation platform described herein could be used to investigate their hypotheses, which were put forth using 1D arguments and have yet to be validated with numerical simulations.

APPENDIX A

INCOMPRESSIBLE STOKES EQUATIONS: STREAM FUNCTION FORMULATION

In this appendix, we discuss the conventional stream function formulation of the incompressible Stokes equations, as well as the numerical approaches we implemented in an attempt to solve this system and some possible reasons why they failed.

The stream function formulation of the incompressible Stokes equations is

$$\nabla \cdot \left[\eta(\phi) \Big(\nabla(\nabla^{\perp}\psi) + \big(\nabla(\nabla^{\perp}\psi)\big)^T \Big) \right] = \nabla p + \nabla \cdot \Big(\nabla\phi\nabla\phi - |\nabla\phi|^2 \mathbf{I} \Big) \qquad \text{(A.1)}$$

where ψ is the stream function, defined such that $\nabla^{\perp}\psi = \mathbf{u}$ (where $\mathbf{u}$ is the fluid velocity, and $\nabla^{\perp} := [\partial_y, \ -\partial_x]$.) To eliminate the pressure term ∇p we apply the operator $\nabla^{\perp}\cdot$ to both sides of Equation (A.1), resulting in a scalar-valued partial differential equation in ψ:

$$\begin{aligned} &\eta''(\phi)\Big(4\phi_x\phi_y\psi_{xy} + {\phi_y}^2\big(\psi_{yy} - \psi_{xx}\big) - {\phi_x}^2\big(\psi_{yy} - \psi_{xx}\big)\Big) + \\ \eta'(\phi)\Big(&4\phi_{xy}\psi_{xy} + 2\big(\phi_x(\psi_{yy} + \psi_{xx})_x + \phi_y(\psi_{xx} + \psi_{yy})_y\big) + \big(\phi_{yy} - \phi_{xx}\big)\big(\psi_{yy} - \psi_{xx}\big)\Big) + \\ &\eta(\phi)\Big(\psi_{xxxx} + 2\psi_{xxyy} + \psi_{yyyy}\Big) - \phi_x\big(\phi_{xx} + \phi_{yy}\big)_y + \phi_y\big(\phi_{xx} + \phi_{yy}\big)_x = 0 \quad \text{(A.2)} \end{aligned}$$

where subscripts denote derivatives, *e.g.*, $\phi_x := \frac{\partial\phi}{\partial x}$. We then divide through by $\eta(\phi)$ in the hopes of lessening the numerical issues associated with rapid variations in $\eta(\phi)$.

With some manipulation, the resulting equation can be written as:

$$4\Big[\partial_{xy}\Big(\ln\big(\eta(\phi)\big)\Big)+\partial_x\Big(\ln\big(\eta(\phi)\big)\Big)\partial_y\Big(\ln\big(\eta(\phi)\big)\Big)\Big]\psi_{xy}+$$
$$+\Big[\big(\partial_{xx}-\partial_{yy}\big)\Big(\ln\big(\eta(\phi)\big)\Big)+\Big(\partial_x\Big(\ln\big(\eta(\phi)\big)\Big)\Big)^2-\Big(\partial_y\Big(\ln\big(\eta(\phi)\big)\Big)\Big)^2\Big]\big(\partial_{xx}-\partial_{yy}\big)\psi+$$
$$+2\nabla\Big(\ln\big(\eta(\phi)\big)\Big)\cdot\nabla\big(\nabla^2\psi\big)-\frac{1}{\eta(\phi)}\Big[\phi_x(\nabla^2\phi)_y-\phi_y(\nabla^2\phi)_x\Big]+\nabla^4\psi=0 \quad \text{(A.3)}$$

where ∂ denotes the partial derivative with respect to the variable indicated by its subscript, *e.g.,* $\partial_x := \frac{\partial}{\partial x}$. We then take the Fourier transform of Equation (A.3), resulting in an equation in terms of the Fourier-transformed variables $\hat{\psi}$ and $\hat{\phi}$. We note that, in Fourier space, the final term $\nabla^4\psi$ on the right-hand side of Equation (A.3) becomes $|\mathbf{k}|^4\hat{\psi}$. Thus, dividing through by $|\mathbf{k}|^4$ results in the presence of a solitary $\hat{\psi}$-term; subtracting this term from both sides of the equation and multiplying through by -1 allows us to express the equation in fixed-point form in terms of the Fourier-transformed variables $\hat{\psi}$ and $\hat{\phi}$:

$$H(\hat{\psi})=\hat{\psi} \quad \text{(A.4)}$$

We then compute the inverse Fourier transform so that our fixed-point equation is in real space, much like (4.44):

$$H_R(\psi)=\psi. \quad \text{(A.5)}$$

We then proceed to solve Equation (A.5) iteratively for ψ.

For certain expressions for $\eta(\phi)$, we were able to solve for ψ using Picard iteration with relaxation and Anderson mixing. However, for our viscosity expression $\eta(\phi)=e^{1.15\left(\frac{\phi}{0.638-\phi}\right)}$ [60], both Picard iteration with relaxation and Anderson mixing failed to yield convergence:

1. At late times t (for which the phase separation had progressed), Picard iteration with relaxation failed to converge for a reasonable value of the relaxation

parameter ω. Specifically, we would have to make ω very small, which causes the iterates to take much longer to converge. We discovered that even for $\omega = 1/1024$, the system would not converge. Each time step was taking several hours, which is of course impractical.

2. Anderson mixing also failed: as time progressed, the dimensions of the linear system (4.46) for the Anderson mixing had to be extremely large in order to achieve convergence; this took several hours per time step also. In addition, numerical issues arose in solving such a large linear system.

We also tried to solve it using a GMRES routine in MATLAB, but this failed also. In addition, we took several conventional measures such as increasing the spatial resolution and decreasing the time step size of the system. However, neither of these improved the convergence after a certain time t. It is also worth noting that the time t for which our Stokes solver appears to break down is relatively early: for some sets of system parameters, it broke down before $t = 200$ (in dimensionless variables); the phase separation had not even progressed enough to achieve the predicted final ϕ-values yet at this dimensionless time.

Another avenue we took in the hopes of assisting our numerical solver was to implement a technique called *first-order continuation* [114]. The idea behind first-order continuation is to improve the initial guess ψ_0 (*i.e.,* make ψ_0 closer to the true solution.) Unfortunately, this approach did not help either.

We began to suspect that the difficulties with our Stokes solver were a result of using the stream function formulation. Specifically, the stream function formulation involves the second derivative of the viscosity with respect to ϕ, $\eta''(\phi)$, whose values become very large at later times due to the rapid, exponential increase in η for higher ϕ-values, coupled with the steep interfaces between phase domains when the phase separation has progressed significantly. For example, when the ϕ-values in our spatial domain ranged between 0.07 and 0.44, the corresponding values of $\eta''(\phi)$ reached

values as high as 1.5×10^4. Tree *et al.* [114] proposed a formulation similar to the one described in Subsection 4.3.3, which inspired us to try that approach. As we discussed in Subsection 4.3.3, the formulation described therein produced a more efficient and numerically robust Stokes solver, which yielded very satisfactory results.

REFERENCES

[1] Binary Colloid Alloy Test (BCAT) images from NASA Physical Sciences Informatics (PSI) system. Accessed July 31, 2023, `https://www.nasa.gov/PSI`.

[2] Experimental data from Binary Colloid Alloy Test (BCAT) experiments, NASA Physical Sciences Informatics (PSI) system. Accessed July 31, 2023, `https://www.nasa.gov/PSI`.

[3] ImageJ online documentation. Accessed July 31, 2023, `https://imagej.net/plugins/miji`.

[4] MIJ homepage, École Polytechnique Fédérale de Lausanne. Accessed July 31, 2023, `http://bigwww.epfl.ch/sage/soft/mij/`.

[5] Science requirement documents from Binary Colloid Alloy Test (BCAT) experiments, NASA Physical Sciences Informatics (PSI) system. Accessed July 31, 2023, `https://www.nasa.gov/PSI`.

[6] M. Abramowitz and I. A. Stegun (editors). *Handbook of Mathematical Functions*. New York: Dover, 10th edition, 1972.

[7] B. J. Alder and T. E. Wainwright. Phase transition for a hard sphere system. *Journal of Chemical Physics*, 27(5):1208–1209, 08 2004.

[8] A. Andersen, J. Madsen, C. Reichelt, S. R. Ahl, B. Lautrup, C. Ellegaard, M. T. Levinsen, and T. Bohr. Double-slit experiment with single wave-driven particles and its relation to quantum mechanics. *Physical Review E*, 92(013006), 2015.

[9] V. J. Anderson and H. N. W. Lekkerkerker. Insights into phase transition kinetics from colloid science. *Nature*, 416:811–815, 2002.

[10] J. Arbelaiz, A. U. Oza, and J. W. M. Bush. Promenading pairs of walking droplets: Dynamics and stability. *Physical Review Fluids*, 3(013604), 2018.

[11] S. Asakura and F. Oosawa. On interaction between two bodies immersed in a solution of macromolecules. *Journal of Chemical Physics*, 22:1255, 1954.

[12] A. E. Bailey, W. C. K. Poon, R. J. Christianson, A. B. Schofield, U. Gasser, V. Prasad, S. Manley, P. N. Segre, L. Cipelletti, W. V. Meyer, M. P. Doherty, S. Sankaran, A. L. Jankovsky, W. L. Shiley, J. P. Bowen, J. C. Eggers, C. Kurta, Jr. T. Lorik, P. N. Pusey, and D. A. Weitz. Spinodal decomposition in a model colloid-polymer mixture in microgravity. *Physical Review Letters*, 99(205701), 2007.

[13] L. Barnes, G. Pucci, and A. U. Oza. Resonant interactions in bouncing droplet chains. *Comptes Rendus Mécanique*, 348(6-7):573–589, 2020.

[14] T. Beatus, T. Tlusty, and B.-Z. Roy. Phonons in a one-dimensional microfluidic crystal. *Nature Physics*, 2(11):743–748, 2006.

[15] T. B. Benjamin and F. Ursell. The stability of the plane free surface of a liquid in vertical periodic motion. *Proceedings of the Royal Society of London A*, 225:505–515, 1954.

[16] T. Bohr, A. Andersen, and B. Lautrup. Bouncing droplets, pilot-waves, and quantum mechanics. In J. Klapp, L. D. G. Sigalotti, A. Medina, A. López, and G. Ruiz-Chavarría, editors, *Recent Advances in Fluid Dynamics with Environmental Applications*, pages 335–349. Springer International Publishing, Switzerland, 2016.

[17] C. Borghesi, J. Moukhtar, M. Labousse, A. Eddi, E. Fort, and Y. Couder. Interaction of two walkers: Wave-mediated energy and force. *Physical Review E*, 90(063017), 2014.

[18] Pierre-Thomas Brun, Daniel M. Harris, Victor Prost, Julio Quintela, and John W. M. Bush. Shedding light on pilot-wave phenomena. *Physical Review Fluids*, 1(050510):1–2, 2016.

[19] N. B. Budanur and M. Fleury. State space geometry of the chaotic pilot-wave hydrodynamics. *Chaos*, 29(013122), 2019.

[20] M. Bukov, L. D'Aless, and A. Polkovnikov. Universal high-frequency behavior of periodically driven systems: from dynamical stabilization to Floquet engineering. *Advances in Physics*, 64(2):139–226, 2015.

[21] J. W. M. Bush. The new wave of pilot-wave theory. *Physics Today*, 68(8):47–53, 2015.

[22] J. W. M. Bush. Pilot-wave hydrodynamics. *Annual Review of Fluid Mechanics*, 47:269–292, 2015.

[23] J. W. M. Bush and A. U. Oza. Hydrodynamic quantum analogs. *Reports on Progress in Physics*, 84(017001), 2021.

[24] N. F. Carnahan and K. E. Starling. Thermodynamic properties of a rigid-sphere fluid. *Journal of Chemical Physics*, 53(600), 1970.

[25] Z. Cheng, P. M. Chaikin, J. Zhu, W. B. Russel, and W. V. Meyer. Crystallization kinetics of hard spheres in microgravity in the coexistence regime: Interactions between growing crystallites. *Physical Review Letters*, 88(015501), 2001.

[26] M. M. P. Couchman and J. W. M. Bush. Free rings of bouncing droplets: stability and dynamics. *Journal of Fluid Mechanics*, 903:A49, 2020.

[27] M. M. P. Couchman, S. E. Turton, and J. W. M. Bush. Bouncing phase variations in pilot-wave hydrodynamics and the stability of droplet pairs. *Journal of Fluid Mechanics*, 871:212–243, 2018.

[28] Y. Couder and E. Fort. Single particle diffraction and interference at a macroscopic scale. *Physical Review Letters*, 97(154101), 2006.

[29] Y. Couder and E. Fort. Probabilities and trajectories in a classical wave-particle duality. *Journal of Physics: Conference Series*, 361(012001), 2012.

[30] Y. Couder, E. Fort, C.-H. Gautier, and A. Boudaoud. From bouncing to floating: noncoalescence of drops on a fluid bath. *Physical Review Letters*, 94(177801), 2005.

[31] Y. Couder, S. Protière, E. Fort, and A. Boudaoud. Walking and orbiting droplets. *Nature*, 437(208), 2005.

[32] T. Cristea-Platon, P. J. Sáenz, and J. W. M. Bush. Walking droplets in a circular corral: Quantisation and chaos. *Chaos*, 28(096116), 2018.

[33] A. P. Damiano, P.-T. Brun, D. M. Harris, C. A. Galeano-Rios, and J. W. M. Bush. Surface topography measurements of the bouncing droplet experiment. *Experiments in Fluids*, 57(163), 2016.

[34] R. Dubertrand, M. Hubert, P. Schlagheck, N. Vandewalle, T. Bastin, and J. Martin. Scattering theory of walking droplets in the presence of obstacles. *New Journal of Physics*, 18(113037), 2016.

[35] M. Durey and P. A. Milewski. Faraday wave-droplet dynamics: Discrete-time analysis. *Journal of Fluid Mechanics*, 821:296–329, 2017.

[36] A. Eddi, A. Boudaoud, and Y. Couder. Oscillating instability in bouncing drop crystals. *Europhysics Letters*, 94(20004), 2011.

[37] A. Eddi, A. Decelle, E. Fort, and Y. Couder. Archimedean lattices in the bound states of wave interacting particles. *Europhysics Letters*, 87(56002), 2009.

[38] A. Eddi, E. Fort, F. Moisy, and Y. Couder. Unpredictable tunneling of a classical wave-particle association. *Physical Review Letters*, 102(240401), 2009.

[39] A. Eddi, J. Moukhtar, S. Perrard, E. Fort, and Y. Couder. Level splitting at a macroscopic scale. *Physical Review Letters*, 108(264503), 2012.

[40] A. Eddi, E. Sultan, J. Moukhtar, E. Fort, M. Rossi, and Y. Couder. Information stored in Faraday waves: the origin of a path memory. *Journal of Fluid Mechanics*, 674:433–463, 2011.

[41] A. Eddi, D. Terwagne, E. Fort, and Y. Couder Y. Wave propelled ratchets and drifting rafts. *Europhysics Letters*, 82(44001), 2008.

[42] R. M. L. Evans and M. E. Cates. Diffusive evolution of stable and metastable phases. I. Local dynamics of interfaces. *Physical Review E*, 56(5):5738–5747, 1997.

[43] R. M. L. Evans and W. C. K. Poon. Diffusive evolution of stable and metastable phases. II. Theory of non equilibrium behavior in colloid-polymer mixtures. *Physical Review E*, 56(5):5748–5758, 1997.

[44] R. M. L. Evans, W. C. K. Poon, and M. E. Cates. Role of metastable states in phase ordering dynamics. *Europhysics Letters*, 38(8):595–600, 1997.

[45] R. M. L. Evans, W. C. K. Poon, and F. Renth. Classification of ordering kinetics in three-phase systems. *Physical Review E*, 64(031403), 2001.

[46] M. Faraday. On the forms and states of fluids on vibrating elastic surfaces. *Philosophical Transactions of the Royal Society of London*, 121:319–340, 1831.

[47] B. Filoux, M. Hubert, and N. Vandewalle. Strings of droplets propelled by coherent waves. *Physical Review E*, 92(041004(R)), 2015.

[48] G. J. Fleer and R. Tuinier. Analytical phase diagrams for colloids and non-adsorbing polymer. *Advances in Colloid and Interface Science*, 143:1–47, 2008.

[49] E. Fort, A. Eddi, J. Moukhtar, A. Boudaoud, and Y. Couder. Path-memory induced quantization of classical orbits. *Proceedings of the National Academy of Sciences*, 107(41):17515–17520, 2010.

[50] A. Furukawa and H. Tanaka. Key role of hydrodynamic interactions in colloidal gelation. *Physical Review Letters*, 104(245702), 2010.

[51] L. Gammaitoni, P. Hänggi, P. Jung, and F. Marchesoni. Stochastic resonance. *Reviews of Modern Physics*, 70(1):223–287, 1998.

[52] A.P Gast, C.K Hall, and W.B Russel. Polymer-induced phase separations in nonaqueous colloidal suspensions. *Journal of Colloid and Interface Science*, 96(1):251–267, 1983.

[53] T. Gilet and J. W. M. Bush. The fluid trampoline: droplets bouncing on a soap film. *Journal of Fluid Mechanics*, 625:167–203, 2009.

[54] P. Hänggi. Driven quantum systems. In T. Dittrich, P. Hänggi, G.-L. Ingold, G. Schön, and W. Zwerger, editors, *Quantum Transport and Dissipation*, pages 249–286. Weinheim: Wiley-VCH, 1998.

[55] D. M. Harris and J. W. M. Bush. Drops walking in a rotating frame: From quantized orbits to multimodal statistics. *Journal of Fluid Mechanics*, 739:444–464, 2014.

[56] D. M. Harris, T. Liu, and J. W. M. Bush. A low-cost, precise piezoelectric droplet-on-demand generator. *Experiments in Fluids*, 56(83), 2015.

[57] D. M. Harris, J. Moukhtar, E. Fort, Y. Couder, and J. W. M. Bush. Wavelike statistics from pilot-wave dynamics in a circular corral. *Physical Review E*, 88(011001), 2013.

[58] D. M. Harris, J. Quintela, V. Prost, P.-T. Brun, and J. W. M. Bush. Visualization of hydrodynamic pilot-wave phenomena. *Journal of Visualization*, 20(1):13–15, 2017.

[59] T. M. Hoang, C. S. Gerving, B. J. Land, M. Anquez, C. D. Hamley, and M. S. Chapman. Dynamic stabilization of a quantum many-body spin system. *Physical Review Letters*, 111(090403), 2013.

[60] G. L. Hunter and E. R. Weeks. The physics of the colloidal glass transition. *Reports on Progress in Physics*, 75(066501), 2012.

[61] S. M. Ilett, A. Orrock, W. C. K. Poon, and P. N. Pusey. Phase behavior of a model colloid-polymer mixture. *Physical Review E*, 51(2), 1995.

[62] D. Jacqmin. Calculation of two-phase Navier-Stokes flows using phase-field modeling. *Journal of Computational Physics*, 155:96–127, 1999.

[63] P. L. Kapitza. Dynamical stability of a pendulum when its point of suspension vibrates. In D. Ter Haar, editor, *Collected papers of P. L. Kapitza*, volume 2, pages 714–725. Oxford: Pergamon, 1965.

[64] P. L. Kapitza. Pendulum with a vibrating suspension. In D. Ter Haar, editor, *Collected papers of P. L. Kapitza*, volume 2, pages 726–737. Oxford: Pergamon, 1965.

[65] C. Kittel. *Introduction to solid state physics*, volume 8. New York: Wiley, 1976.

[66] K. Kumar. Linear theory of Faraday instability in viscous liquids. *Proceedings of the Royal Society A*, 452:1113–1126, 1996.

[67] K. Kumar and L. S. Tuckerman. Parametric instability of the interface between two fluids. *Journal of Fluid Mechanics*, 279:49–68, 1994.

[68] M. Labousse, A. U. Oza, S. Perrard, and J. W. M. Bush. Pilot-wave dynamics in a harmonic potential: Quantization and stability of circular orbits. *Physical Review E*, 93(033122), 2016.

[69] M. Labousse, S. Perrard, Y. Couder, and E. Fort. Self-attraction into spinning eigenstates of a mobile wave source by its emission back-reaction. *Physical Review E*, 94(042224), 2016.

[70] M. Lam, B. Khusid, L. Kondic, and W. V. Meyer. Role of diffusion in crystallization of hard-sphere colloids. *Physical Review E*, 104(054607), 2021.

[71] A. G. Lamorgese and R. Mauri. Phase-field modeling of mixing/demixing of regular binary mixtures with a composition-dependent viscosity. *Journal of Applied Physics*, 121(134302), 2017.

[72] A. G. Lamorgese, D. Molin, and R. Mauri. Phase field approach to multiphase flow modeling. *Milan Journal of Mathematics*, 79:597–642, 2011.

[73] L. D. Landau and E. M. Lifshitz. *Course of theoretical physics. vol. 1: Mechanics.* Oxford: Butterworth-Heinemann, 1976.

[74] H. N. W. Lekkerkerker, W. C. K. Poon, P. N. Pusey, A. Stroobants, and P. B. Warren. Phase behavior of colloid+polymer mixtures. *Europhysics Letters*, 20(6):559–564, 1992.

[75] F. Length, W. C. K. Poon, and R. M. L. Evans. Phase transition kinetics in colloid-polymer mixtures at triple coexistence: Kinetic maps from free-energy landscapes. *Physical Review E*, 64(031402), 2001.

[76] S. I. Lieber, M. C. Hendershott, A. Pattanaporkratana, and J. E. Maclennan. Self-organization of bouncing oil drops: two dimensional lattices and spinning clusters. *Physical Review E*, 75(56308), 2007.

[77] P. A. Milewski, C. Galeano-Rios, A. Nachbin, and J. W. M. Bush. Faraday pilot-wave dynamics: modelling and computation. *Journal of Fluid Mechanics*, 778:361–388, 2015.

[78] J. Moláček and J. W. M. Bush. Drops walking on a vibrating bath: towards a hydrodynamic pilot-wave theory. *Journal of Fluid Mechanics*, 727:612–647, 2013.

[79] A. Moussaïd, W. C. K. Poon, P. N. Pusey, and M. F. Soliva. Structure of marginal and fully developed colloidal liquids. *Physical Review Letters*, 82(1), 1999.

[80] K-C. Ng. Hypernetted chain solutions for the classical one-component plasma up to Γ =7000. *Journal of Chemical Physics*, 61(2680), 1974.

[81] A. U. Oza, D. M. Harris, R. R. Rosales, and J. W. M. Bush. Pilot-wave dynamics in a rotating frame: on the emergence of orbital quantization. *Journal of Fluid Mechanics*, 744:404–429, 2014.

[82] A. U. Oza, R. R. Rosales, and J. W. M. Bush. A trajectory equation for walking droplets: hydrodynamic pilot-wave theory. *Journal of Fluid Mechanics*, 737:552–570, 2013.

[83] A. U. Oza, E. Siéfert, D. M. Harris, J. Moláček, and J. W. M. Bush. Orbiting pairs of walking droplets: Dynamics and stability. *Physical Review Fluids*, 2(053601), 2017.

[84] A. U. Oza, Ø. Wind-Willassen, D. M Harris, R. R. Rosales, and J. W. M. Bush. Pilot-wave hydrodynamics in a rotating frame: Exotic orbits. *Physics of Fluids*, 26(082101), 2014.

[85] S. Perrard. *Une mémoire ondulatoire: Etats propres, Chaos et Probabilités.* PhD thesis, Université Paris Diderot, 2014. Pages 182–183.

[86] S. Perrard and M. Labousse. Transition to chaos in wave memory dynamics in a harmonic well: Deterministic and noise-driven behavior. *Chaos*, 28(096109), 2018.

[87] S. Perrard, M. Labousse, E. Fort, and Y. Couder. Chaos driven by interfering memory. *Physical Review Letters*, 113(104101), 2014.

[88] S. Perrard, M. Labousse, M. Miskin, E. Fort, and Y. Couder. Self-organization into quantized eigenstates of a classical wave-driven particle. *Nature Communications*, 5(3219), 2014.

[89] W. Poon. Colloids as big atoms. *Science*, 304:830–831, 2004.

[90] W. C. K. Poon. The physics of a model colloid-polymer mixture. *Journal of Physics: Condensed Matter*, 14:R859, 2002.

[91] W. C. K. Poon, F. Renth, R. M. L. Evans, D. J. Fairhurst, M. E. Cates, and P. N. Pusey. Colloid-polymer mixtures at triple coexistence: kinetic maps from free-energy landscapes. *Physical Review Letters*, 83(6), 1999.

[92] A. Prosperetti. Viscous effects on small-amplitude surface waves. *Physics of Fluids*, 19(2):195–203, 1976.

[93] S. Protière, A. Boudaoud, and Y. Couder. Particle-wave association on a fluid interface. *Journal of Fluid Mechanics*, 554:85–108, 2006.

[94] S. Protière, Y. Couder, E. Fort, and A. Boudaoud. The self-organization of capillary wave sources. *Journal of Physics: Condensed Matter*, 17(3529), 2005.

[95] G. Pucci, D. M. Harris, L. M. Faria, and J. W. M. Bush. Walking droplets interacting with single and double slits. *Journal of Fluid Mechanics*, 835:1136–1156, 2018.

[96] P. N. Pusey and W. van Megen. Phase behaviour of concentrated suspensions of nearly hard colloidal spheres. *Nature*, 320(6060):340–342, 1986.

[97] A. Rahman. Standard map-like models for single and multiple walkers in an annular cavity. *Chaos*, 28(096102), 2018.

[98] S. S. Rao. *Mechanical Vibrations*. Boston: Addison Wesley, 1995.

[99] C. O. Reinhold, J. Burgdörfer, M. T. Frey, and F. B. Dunning. Dynamic stabilization of the periodically kicked Rydberg atom. *Physical Review Letters*, 79(26), 1997.

[100] M. Rode, J. Madsen, and A. Andersen. Wave fields in double-slit experiments with wave-driven droplets. *Physical Review Fluids*, 4(104801), 2019.

[101] M. C. M. Rodrigues and M. Militzer. Application of the rolling ball algorithm to measure phase volume fraction from backscattered electron images. *Materials Characterization*, 163(110273), 2020.

[102] D. Ruelle and F. Takens. On the nature of turbulence. *Communications in Mathematical Physics*, 20:167–192, 1971.

[103] W. B. Russel, P. M. Chaikin, J. Zhu, W. V. Meyer, and R. Rogers. Dendritic growth of hard sphere crystals. *Langmuir*, 13:3871–3881, 1997.

[104] J. Sabin, A. E. Bailey, G. Espinosa, and B. J. Frisken. Crystal-arrested phase separation. *Physical Review Letters*, 109(195701), 2012.

[105] P. J. Sáenz, T. Cristea-Platon, and J. W. M. Bush. Statistical projection effects in a hydrodynamic pilot-wave system. *Nature Physics*, 14:315–319, 2018.

[106] P. J. Sáenz, T. Cristea-Platon, and J. W. M. Bush. A hydrodynamic analog of Friedel oscillations. *Science Advances*, 6(20), 2020.

[107] R. J. Speedy. Pressure and entropy of hard-sphere crystals. *Journal of Physics: Condensed Matter*, 10:4387–4391, 1998.

[108] S. R. Sternberg. Biomedical image processing. *IEEE Computer*, 16(1):22–34, 1983.

[109] L. Tadrist, J.-B. Shim, T. Gilet, and P. Schlagheck. Faraday instability and subthreshold Faraday waves: surface waves emitted by walkers. *Journal of Fluid Mechanics*, 848:906–945, 2018.

[110] L. D. Tambasco, D. M. Harris, A. U. Oza, R. R. Rosales, and J. W. M. Bush. The onset of chaos in orbital pilot-wave dynamics. *Chaos*, 26(103107), 2016.

[111] R. B. Thompson, K. Ø. Rasmussen, and T. Lookman. Improved convergence in block copolymer self-consistent field theory by Anderson mixing. *Journal of Chemical Physics*, 120(31), 2004.

[112] S. J. Thomson, M. M. P. Couchman, and J. W. M. Bush. Collective vibrations of confined levitating droplets. *Physical Review Fluids*, 5(083601), 2020.

[113] F. L. Traversa, M. Di Ventra, and F. Bonani. Generalized Floquet theory: Application to dynamical systems with memory and Bloch's theorem for nonlocal potentials. *Physical Review Letters*, 110(170602), 2013.

[114] D. R. Tree, K. T. Delaney, H. D. Ceniceros, T. Iwama, and G. H. Fredrickson. A multi-fluid model for microstructure formation in polymer membranes. *Soft Matter*, 13(3013), 2017.

[115] S. E. Turton, M. M. P. Couchman, and J. W. M. Bush. A review of the theoretical modeling of walking droplets: towards a generalized pilot-wave framework. *Chaos*, 28(096111), 2018.

[116] R. Valani, A. C. Slim, and T. Simula. Hong-Ou-Mandel-like two-drop correlations. *Chaos*, 28(096104), 2018.

[117] W. van Megen, T. C. Mortensen, S. R. Williams, and J. Müller. Measurement of the self-intermediate scattering function of suspensions of hard spherical particles near the glass transition. *Physical Review E*, 58(6073), 1998.

[118] J. Walker. Drops of liquid can be made to float on the liquid. What enables them to do so? *Scientific American*, 238(151), 1978.

[119] Ø. Wind-Willassen, J. Moláček, D. M. Harris, and J. W. M. Bush. Exotic states of bouncing and walking droplets. *Physics of Fluids*, 25(082002), 2013.

[120] J. Zhu, L.-Q. Chen, J. Shen, and V. Tikare. Coarsening kinetics from a variable-mobility Cahn-Hilliard equation: Application of a semi-implicit Fourier spectral method. *Physical Review E*, 60(4), 1999.

[121] J. Zhu, M. Li, R. Rogers, W. V. Meyer, R. H. Ottewill, W. B. Russel, and P. M. Chaikin. Crystallization of hard-sphere colloids in microgravity. *Nature*, 387:883–885, 1997.